Spring 1-1-2012

An Optical Characterization Technique for Parabolic Trough Solar Collectors Using Images of the Absorber Reflection

Jeanmarie Kathleen Owkes
University of Colorado at Boulder, kathleen.owkes@gmail.com

An Optical Characterization Technique for Parabolic Trough Solar Collectors Using Images of the Absorber Reflection

by

Jeanmarie Kathleen Owkes

B.S., Rose-Hulman Institute of Technology, 2007

M.S., University of Colorado, 2012

A thesis submitted to the

Faculty of the Graduate School of the

University of Colorado in partial fulfillment

of the requirements for the degree of

Doctor of Philosophy

Department of Mechanical Engineering

2012

This thesis entitled:

An Optical Characterization Technique for Parabolic Trough Solar Collectors
Using Images of the Absorber Reflection

written by Jeanmarie Kathleen Owkes
has been approved for the Department of Mechanical Engineering

_____

Prof. John Daily

_____

Dr. Chuck Kutscher

Date _____

The final copy of this thesis has been examined by the signatories, and we find that both the content and the form meet acceptable presentation standards of scholarly work in the above mentioned discipline.

Owkes, Jeanmarie Kathleen (Ph.D., Mechanical Engineering)

An Optical Characterization Technique for Parabolic Trough Solar Collectors Using Images of the Absorber Reflection

Thesis directed by Prof. John Daily

As the concentrating solar power industry competes to develop a less-expensive parabolic trough collector, assurance is needed that new parabolic trough collectors maintain accurate optical alignment. Previous optical characterization techniques are either too slow, ill-suited for field testing, or do not allow the collector to be tested in realistic orientations. The Observer method presented here enables the rapid optical characterization of parabolic trough collectors in any orientation in the field.

The Observer method directly measures the combined optical angular errors in the reflector surface shape and the absorber position, which can be separated into its two components: reflector surface slope and absorber misalignment. The data acquisition requires the placement of photogrammetry targets on and around the collector. Multiple photographs of the absorber and its reflection are taken with a digital camera from different angles with respect to the collector. The images are processed to determine the camera location of each image using photogrammetry bundle analysis. The absorber and its reflection are found in the photographs using image-processing techniques.

A Monte Carlo uncertainty model was developed to determine the uncertainty in the Observer measurements. The uncertainty was estimated for a wide array of measurement test scenarios to demonstrate the user's control over the measurement uncertainty. To validate the Observer method, the absorber alignment technique was compared to traditional photogrammetry; the absorber position measured with the two methods compared with a root-mean-square difference of 1.5 mm in the transverse direction and 0.86 mm along the optical axis. The reflector surface slope error measurement was compared to both VSHOT and SOFAST, two well-established optical characterization

tools, by measuring a single reflector panel in the laboratory. The VSHOT and SOFAST measurements agreed with the Observer with a root-mean-square difference of 1.6 mrad and 2.1 mrad, respectively. In the field, the Observer method's capability to test collectors in any orientation was demonstrated by mounting the camera on a radio-controlled helicopter and measuring a collector oriented at 90° above the horizon. The absorber measurement capability was demonstrated in the field for a collector facing both horizontally and vertically.

Dedication

To my parents,

Barbara and Daniel Stynes,

for teaching me the joy of learning,

the importance of education,

and preparing me for life after childhood

and

To my husband, Mark,

for supporting and encouraging me through the past five years

Acknowledgements

I would like to thank everyone who has helped and supported me in this endeavor. My advisor, Professor John Daily, has spent the past five years supporting and encouraging me, for which I am very grateful. His guidance has helped me maintain a broader perspective during my graduate education and discover my independence and competence. I would also like to thank Dr. Chuck Kutscher for providing me the opportunity to select this incredible and exciting dissertation topic. Chuck has been a supportive mentor and dedicated advisor to me. Thank you to Professor Tad Pfeffer and Dr. Yushin Ahn for introducing me to photogrammetry, which has become a vital component of the Observer method. Additionally, I thank the Thermal Systems Group at NREL, especially Gary Jorgensen, Allion Gray, Frank Burkholder, Keith Gawlik, Jen Crawford, Carl Bingham, Judy Netter, Tim Wendelin, Guangdong Zhu, Kane Chinnel, and Ben Ihas of the Distant Observer Team. This dissertation would not exist without the countless hours spent by the Distant Observer team developing the hardware, testing in the field, and contributing to every aspect of this project. Thank you also to Teri Spinuzzi, without whom the Thermal Systems Group could not function. Thank you to all of my committee members: Prof. John Daily, Dr. Chuck Kuscher, Prof. Tad Pfeffer, Prof. Jean Hertzberg, and Dr. Keith Gawlik for their time supporting, guiding, and evaluating this work. Finally, I would like to thank NREL's industry partners who have generously allowed us to test their collectors and use their facilities for developing, troubleshooting, and demonstrating the Observer method. Without parabolic trough collectors to test, this work would not have been possible. This work was supported by the U.S. Department of Energy under Contract No. DE-AC36-08-GO28308 with the National Renewable Energy Laboratory.

Contents

Chapter

Tables

Table

Figures

Figure

Nomenclature

B_{eff}	Angular distribution of effective source including optical errors
B_{source}	Angular distribution of solar energy
D_{a}	Absorber diameter
$d_{\text{j1,j2}}$	Distance constraint
E	Angular distribution of combined optical errors
f	Collector focal length
f_{c}	Focal length of the camera lens
i	Photograph number
I_{b}	Total incident flux from the source
j	Target number
K_1, K_2, K_3	Radial lens distortion coefficients
l_{c}	Collector length
M	Number of photographs in photogrammetry bundle
N	Number of targets in photogrammetry bundle
N_{x}	Number of pixels along the image width
N_{y}	Number of pixels along the image height
P_1, P_2	Tangential lens distortion coefficients
q	Flux intercepted by the absorber
$\mathbf{R}$	Rotation matrix producing the Euler angle rotation of the camera
$\hat{r_{\text{i}}}$	Unit normal incident vector
$\hat{r_{\text{r}}}$	Unit normal reflected vector

$\hat{r_{\mathrm{t}}}$	Unit normal refracted vector
$s_{\mathrm{x}}, s_{\mathrm{y}}$	Width and height of the image sensor
w_{ap}	Collector aperture width
X, Y, Z	Object point
x, y	Image point on an ideal perspective-center camera
x', y'	Image point on a real camera
x_0, y_0	Perspective center of the camera
$X_{\mathrm{a}}, Z_{\mathrm{a}}$	Absorber position relative to the collector vertex
$X_{\mathrm{c}}, Y_{\mathrm{c}}, Z_{\mathrm{c}}$	Camera position
$X_{\mathrm{f}}, Z_{\mathrm{f}}$	Location of the absorber projected onto the focal-line plane
$x_{\mathrm{I}}, y_{\mathrm{I}}$	Image point location in pixel space
α	Absorber absorptance
$\grave{\alpha}$	Angular acceptance function
γ	Intercept factor
$\delta_{\mathrm{x}}, \delta_{\mathrm{y}}$	Total lens distortion corrections
Δx_{abs}	Average spatial resolution indicator across the absorber
Δx_{ap}	Average spatial resolution indicator across the collector aperture
$\Delta\Phi_{\mathrm{c}}$	Average angular resolution indicator
η	Efficiency of a parabolic trough solar collector
η_{o}	Optical efficiency at normal incidence
θ_{a}	Effective slope error due to absorber misalignment
θ_{r}	Reflector transverse slope error
θ_{ra}	Reflector-absorber angle
$\theta_{\mathrm{r,long}}$	Reflector longitudinal slope error
$\vec{\xi}$	Object point coordinates
ρ	Reflector reflectance

σ_{total}	Standard deviation of Gaussian distribution of total optical errors
σ_{r}	Standard deviation of Gaussian distribution of reflector slope errors
σ_{a}	Standard deviation of Gaussian distribution of absorber effective slope errors
$\sigma_{\text{specularity}}$	Standard deviation of Gaussian distribution of reflector specularity
σ_{tracking}	Standard deviation of Gaussian distribution of tracking errors
τ	Glass transmittance
Φ_{c}	Transverse incidence angle between the camera and a point on the collector
$\vec{\chi}$	External orientation parameters of the camera
ω, ϕ, κ	Euler angle rotation of the camera about the Z-, X-, and Y-axis

Chapter 1

Introduction

The development of renewable energy sources around the world has soared over the last decade in response to evidence linking climate change with the burning of fossil fuels. As the price of photovoltaics (PV) continues to drop, the concentrating solar power (CSP) industry is striving to achieve major cost reductions to be competitive with PV. By capturing solar thermal energy instead of solar electric energy as PV does, CSP lends itself to efficient, less expensive thermal storage. Therefore, CSP is often attractive to utility companies looking to shift solar energy production in the afternoon to provide electricity during the evening hours. The parabolic trough is one type of CSP technology that has been operating in the Mojave Desert since the 1980s.

A parabolic trough collector has a parabolic-shaped reflector that concentrates solar energy onto a cylindrical receiver absorber located at the parabola's focal line. In the last decade, many companies have been developing new parabolic trough designs and building utility-scale parabolic trough power plants in the United States. The construction of a parabolic trough power plant represents a significant investment because the majority of the cost is paid up front. However, the fuel itself, solar energy, is free. Investors and utilities want assurances that the trough will perform as advertised. As companies strive to reduce material, construction, and installation costs of their parabolic trough collectors, performance losses associated with those cost reductions would greatly impact the levelized cost of electricity. Thus, it is essential that parabolic trough collectors maintain high efficiencies in spite of cost reductions.

As one aspect of the collector performance, the solar intercept factor provides a metric for the

geometric alignment of a parabolic trough. An efficient parabolic trough must have a reflector that conforms closely to an ideal parabola with the receiver absorber located at its focal line. The surface profile of the reflector and the alignment of the absorber, which both contribute to the intercept factor, can be difficult to measure especially after installation in the field, due to the large scale and the uncontrolled field environment. However, the conformation of these components to design is often highly dependent on the installation process so that the conformation cannot necessarily be measured in the laboratory and assumed applicable for field installations. Therefore, it is essential for the parabolic trough industry to have access to a tool capable of measuring the reflector surface profile and absorber alignment because of the affect of optical alignment on the intercept factor.

The Distant Observer technique originally outlined by Wood in 1981 [41] as a qualitative analysis has been adapted and developed into a quantitative analysis presented herein as the Observer method. The Observer method provides the means to measure the optical alignment of a parabolic trough solar collector in the field. The research presented here demonstrates the ability to measure both the reflector surface profile and the absorber alignment independently, as well as the combined effects of both. The method is flexible enough to be used for both high-accuracy research and development applications, as well as lower-accuracy multi-collector surveys. Using a radio-controlled helicopter platform, the collector can be tested in any orientation, thus providing the means to perform a gravity-loading analysis on the collector optical alignment.

Chapter 2

Background

2.1 Parabolic Trough Solar Collector

A parabolic trough is a type of concentrating solar thermal technology. Concentrating solar power (CSP) uses a reflector to focus direct-normal solar radiation onto a receiver. The conventional solar trough tracks the sun during the day by rotating about a single axis. Typical collectors track the sun from east to west by rotating about a north-south axis. A reflective surface formed in the shape of a parabola focuses solar rays onto a cylindrical receiver located at the focal line. The receiver comprises an absorber tube surrounded by a glass envelope. A vacuum is drawn in the annulus between these two tubes to minimize heat losses to the environment.

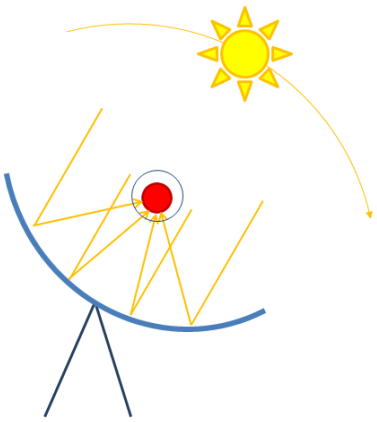

Figure 2.1: Parabolic trough cross-section

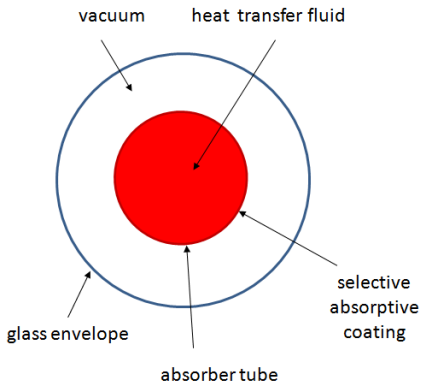

Figure 2.2: Receiver cross-section (enlarged)

A heat transfer fluid (HTF), typically oil, is pumped through the absorber tube and heated by the sun's concentrated energy. The heated HTF is then used to either produce electricity with

a typical Rankine steam turbine power cycle or provide direct heat for industrial processes or hot water. For electricity generation, the HTF is heated to over 350°C. The main attraction of CSP is its high compatibility with thermal storage. Plants without storage tanks inherently have about 30 minutes of built-in storage due to the thermal mass of the system. New plants are being designed with six or more hours of thermal storage to extend electricity production into evening peak hours.

2.1.1 Parabolic Trough Design

The base unit of a parabolic trough field is a solar collector assembly (SCA). An SCA comprises parabolic trough modules (usually 6-12); each module is designed with a complete stand-alone frame. The modules are mounted together and controlled by the same tracking drive. Multiple SCAs are then connected in series to form an entire row along which fluid is pumped. The classic parabolic trough design can be seen in the Luz LS-2 and LS-3 collectors, whose dimensions are specified in Table 2.1 The reflector consists of four curved glass mirror sections across the aperture and five (seven) mirror sections along the length for the LS-2 (LS-3) design. Each mirror panel has four mounting points on the back that attach to the frame. Figure 2.3 shows an LS-3 module during assembly. Two of the mirror panels, as well as the receiver and supports, have not yet been installed.

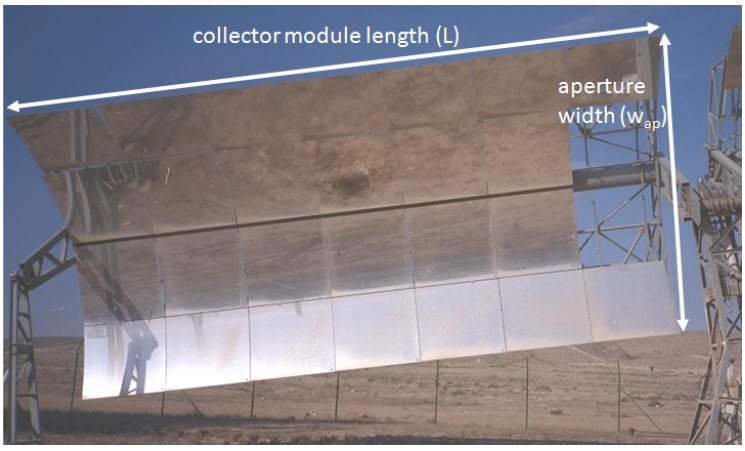

Figure 2.3: Luz LS-3 collector module under construction

Table 2.1: Dimensions of Luz LS-2 and LS-3 [10]

Type	LS-2	LS-3
Aperture width (w_{ap})	5 m	5.76 m
Length (l_c)	7.89 m	11.9 m
Focal length (f)	1.49 m	1.71 m
Absorber diameter (D_a)	70 mm	70 mm

2.1.2 Parabolic Trough Power Plant

In a typical parabolic trough power plant with thermal storage, an oil HTF is pumped through the solar trough field to be heated by the sun. Some of the oil is used to create steam, which runs a steam turbine and produces electricity. The remaining oil is run through a heat exchanger with a molten salt HTF that is being moved from a cold tank to a hot tank. After the sun goes down, molten salt is moved from the hot to cold tank, exchanging heat with the oil along the way. The oil is used to produce more steam to continue electricity production after the sun goes down. Figure 2.4 shows a schematic of a typical parabolic trough power plant with two-tank

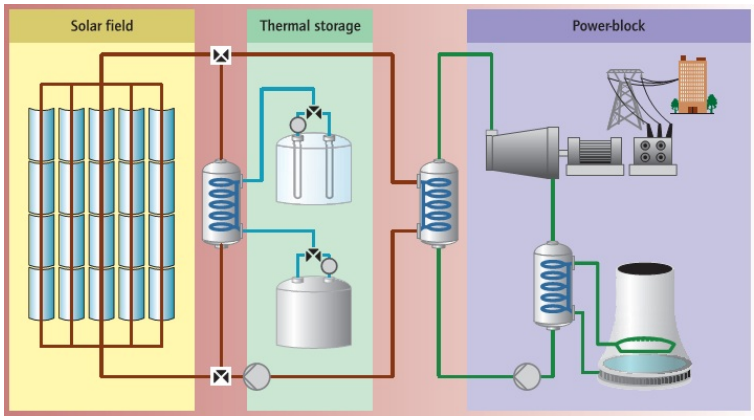

Figure 2.4: Parabolic trough power plant schematic [16]

thermal storage. Alternatives on this model are currently under development. One alternative is to use molten salt directly in the field; however, molten salt has a high freezing point requiring a robust freeze-protection system. Other alternatives include different thermal storage media.

2.1.3 Operating Parabolic Trough Facilities

The Solar Energy Generating Systems (SEGS) were constructed in California's Mojave Desert during the 1980s. The facilities comprise nine individual parabolic trough power plants with a total installed capacity of 354 megawatts (MW). The SEGS plants are still operational and provide electricity to the grid. After the completion of the SEGS plants, there was a 15-year period during which no CSP plants were constructed in the United States. This was due to both natural gas prices declining and the government tax incentives for electricity produced from solar power not being renewed. In 2006, Arizona Public Services completed a 1-MW parabolic trough installation in Saguaro, AZ. The Saguaro power plant runs on an organic Rankine cycle, rather than the traditional Rankine-steam cycle used in the SEGS plants. In 2007, Nevada Solar One, a 64-MW plant, began operation in Boulder City, NV. Abengoa Solar's 280-MW Solana plant is currently under construction. Additional plants are operational or under development around the world, including dozens of plants in Spain [35].

2.1.4 Solar Resource

As sunlight travels through the earth's atmosphere, some of it reaches the earth's surface directly (direct-normal [or beam] radiation), and the rest of it (diffuse radiation) is absorbed, scattered, and reflected by particles in the atmosphere. The sum of beam and diffuse radiation is called the total global solar radiation. CSP technologies use direct-normal solar radiation and are thus only practical in regions with high values thereof. Land with an annual average of at least 6.75 $kWh/m^2/day$ is considered to have high economic potential for CSP [21]. In the United States, this level of direct-normal solar resource is found exclusively in the southwest (Fig. 2.5).

2.2 Performance

The efficiency of a concentrating solar collector varies with the level of direct-normal solar radiation and the absorber temperature. However, due to the difficulty in measuring the absorber

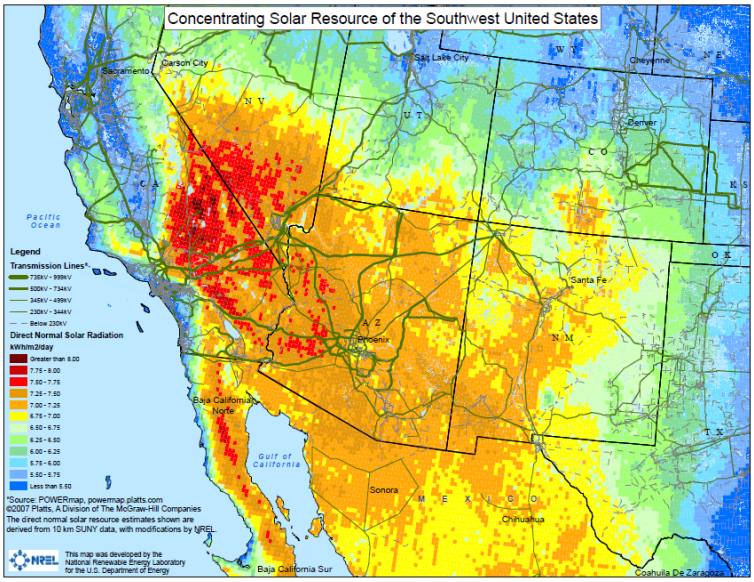

Figure 2.5: Direct-normal solar resource in the southwestern United States [21]

temperature directly, the efficiency is usually expressed as a function of the heat transfer fluid temperature (T_{htf}) minus the ambient temperature at which the receiver was tested, as shown in Fig. 2.6 [20]. The y-intercept of the efficiency curves in Fig. 2.6 is the optical efficiency (η_{o}) at

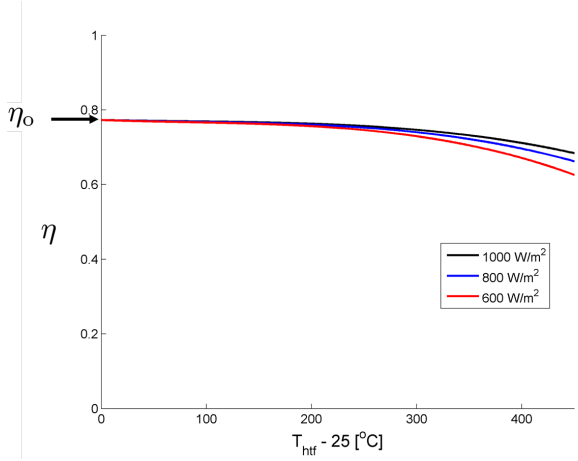

Figure 2.6: Parabolic trough efficiency curve for different levels of direct-normal solar radiation [20]

normal incidence, which occurs when there are no heat losses. The optical efficiency at normal incidence is the product of the intercept factor, γ, mirror reflectance, ρ, glass transmittance, τ, and

absorber absorptance, α:

$$\eta_o = \gamma\rho\tau\alpha \tag{2.1}$$

The reflectance, transmittance, and absorptance are material properties that can be measured in a laboratory. However, the intercept factor is a geometric quantity that characterizes the total geometric accuracy of the system and is defined as the fraction of solar energy reflected off the concentrator that is intercepted by the absorber tube with perfect transmittance through the glass envelope. The intercept factor depends on the reflector surface profile, absorber alignment, tracking error, mirror specularity, and the sun shape.

2.2.1 Reflector Surface Profile

The reflector surface profile is usually referred to as the reflector slope and indicates how well the concentrator conforms to an ideal parabola. It is common for solar mirrors to exhibit some degree of aberrations on a scale larger than the roughness or specularity of the mirror surface [19]. Mirror aberrations consist of striations created during the reflector manufacturing process, as well as warping imposed when the mirror is bonded to another material and any other distortions that cause the reflector to focus at a location other than the design focal line. Reflector surface slope errors may also appear on a larger scale if segmented reflectors are not well aligned relative to one another. Figure 2.7 shows exaggerated reflector slope errors. Reflector slope errors may change with the orientation of the collector due to changing gravity loads. Thus, it is important to specify the orientation in which the reflector slope errors are measured. Ideally, reflector slope errors should be measured with the collector positioned straight up because the most energy is collected around this orientation.

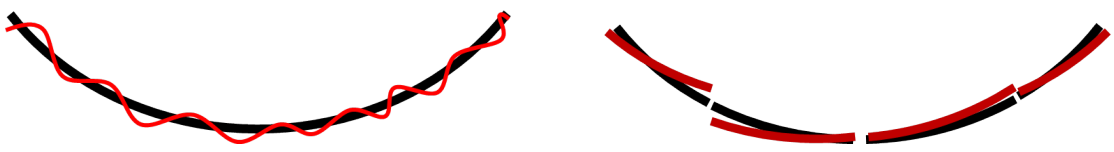

Figure 2.7: Exaggerated reflector slope errors shown in red with the ideal parabolic shape in black

2.2.2 Absorber Alignment

The absorber alignment describes how close the center of the absorber is to the focal line of the parabolic concentrator. Figure 2.8 shows a misaligned absorber. Receivers are typically about four meters long, supported at their ends by tube supports extending from the vertex of the trough. It is common for the absorber to sag from the weight of the heat transfer fluid. As with reflector alignment, absorber alignment is also dependent on the collector orientation. Absorbers may be more inclined to sag in a particular direction, causing increased errors at certain times of the day.

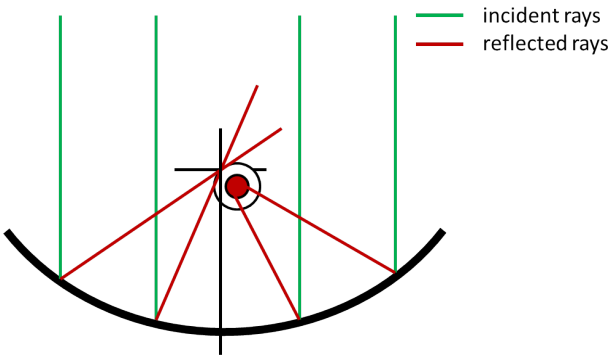

Figure 2.8: Absorber misalignment and associated missing reflected rays

2.2.3 Tracking Error

The tracking error refers to the difference between the sun's position and the direction that the trough is pointing. Typical tracking algorithms adjust the trough's position incrementally by overshooting the sun's position by a couple milliradians and then waiting until the sun has passed the position at which the trough is pointing before moving again (see Fig. 2.10). Solar trackers are designed to maintain the difference between the trough and solar positions small enough that solar energy is not missing the absorber; however, over time, tracking accuracy may decrease. Additionally, tracking twist may occur because several modules are rotated with a single drive mechanism. Those modules immediately next to the drive may be tracking more accurately than those located further away from the drive.

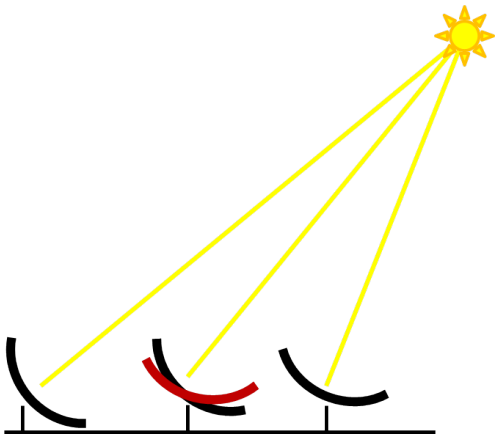

Figure 2.9: Exaggerated tracking error

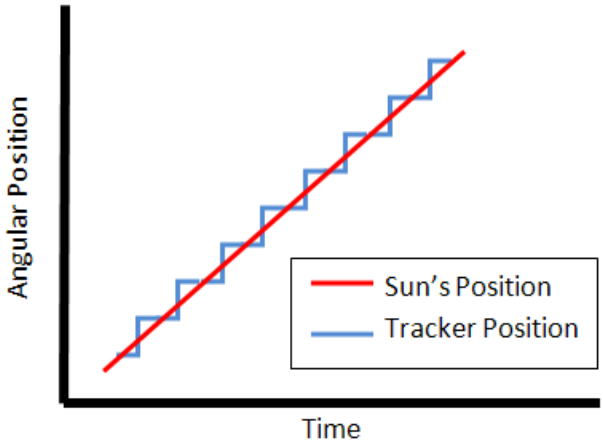

Figure 2.10: Typical tracking algorithm

2.2.4 Reflector Specularity

A perfectly specular mirror would reflect an incoming ray as a single reflected ray. Reflection from a real mirror results in a reflected ray that is distributed across a specified cone angle. A Gaussian distribution is typically used to represent the intensity distribution of a reflected ray due to non-perfect reflector specularity. Figure 2.11 illustrates the concept of reflector specularity.

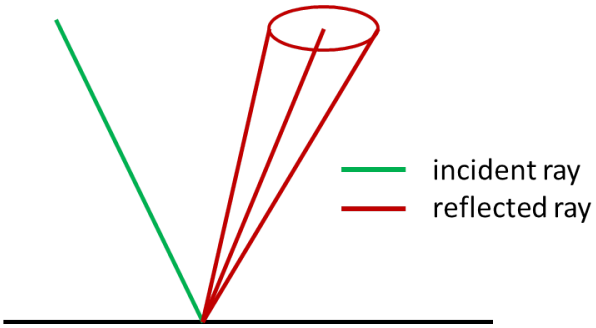

Figure 2.11: The concept of reflector specularity

2.2.5 Sunshape

The sun is not a point source of energy; its intensity is distributed across a finite cone angle. As sunlight travels through the earth's atmosphere, interactions with large particles cause forward scattering that forms the solar aureole (the circumsolar region). Figure 2.12 illustrates the solar

disk and solar aureole. The average solar intensity distribution as a function of the angle of the rays measured by Neumann et al. [24] is shown in Fig. 2.13.

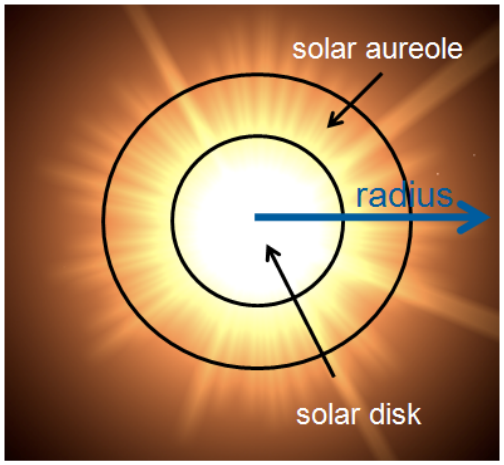

Figure 2.12: The solar disk and solar aureole

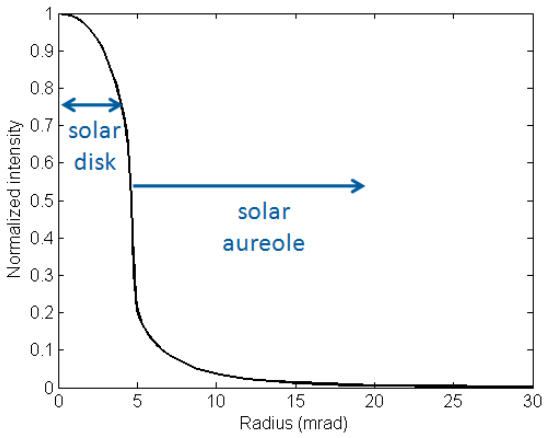

Figure 2.13: Averaged solar profiles [24]

Chapter 3

Purpose

In this chapter, I will present my research objectives and provide an overview of the method selected to achieve those objectives. I will then supply the motivation for this work, including the inadequacies of current optical characterization techniques for parabolic trough collectors, as well as the recent surge in industry growth and the direct link between optical performance and levelized cost of electricity. Finally, I will present an overview of likely uses for the presented method.

3.1 Research Objectives

The objective of this research is to develop the capability to characterize the optical alignment of a parabolic trough collector in the field, under normal operating conditions, and on a reasonable time scale. The optical alignment comprises both the absorber position and the reflector surface slope. The objective is to determine the individual contributing errors due to absorber misalignment and reflector slope, as well as the combined effect on the collector intercept factor. Testing in the field requires transportability of the test equipment, as well as flexibility of the method for uncontrolled outdoor lighting conditions. Normal operating conditions mean that the collectors can be measured in any orientation that is at least 10° above the horizon. Finally, the measurement must be fast enough to provide real-time results to support the research and development of new collector designs; measuring a single collector in less than an hour including setup time is desireable.

3.2 The Observer Method

The Observer method, first outlined by Wood as the Distant Observer in 1981 [41], was selected as the most promising means to test the optical performance of parabolic trough solar collectors in the field. In this method, a series of digital photographs is taken with a camera oriented at different angles with respect to the optical axis of the collector. By analyzing the reflected image of the absorber, the combined reflector slope errors and absorber alignment errors can be quantified. The absorber position will be measured using a triangulation technique specifically developed to complement the Observer method. Once the absorber position is known, the reflector slope errors can be separated from the absorber alignment errors. This method requires minimal equipment and time. An aerial vantage point allows the collector to be tested in any orientation. This technique aims to replace slower, more expensive tools that are ill-suited for outdoor testing.

3.3 Motivation

3.3.1 Inadequacies of Previous Techniques

Previous methods for characterization of the collector optical alignment are too slow, ill-suited for field testing, or limit the collector orientation during testing. Previous techniques focus almost exclusively on measuring the reflector surface slope error while ignoring the equal importance of absorber alignment. There is no prior practical measurement technique for measuring the absorber alignment with the collector positioned in any orientation. Table 3.1 summarizes some currently available parabolic trough optical alignment measurement tools and their limitations. VSHOT (Video Scanning Hartmann Optical Test) is a laser scanning tool, photogrammetry is a general position measurement technique, SOFAST (Sandia Optical Fringe Analysis Slope Tool) is a fringe-reflection tool, and TARMES (Trough Absorber Reflection Measurement System) is an absorber-reflection tool.

Table 3.1: Reflector slope error measurement tools

Tool	**Application**	**Time scale**	**Orientations**	**Absorber Method**	Source
VSHOT	Laboratory[1]	2-5 hours	0°	Not applicable	[38]
Photogrammetry	Field and Lab.	1 day	Any	Targets on receiver	[26]
SOFAST	Laboratory	5 minutes	0°	Not applicable	[1]
TARMES	Field	30 minutes	0°	Laser distance meter	[36]
Observer	Field and Lab.	15 minutes	Any	Triangulation	-

The state-of-the-art tool prior to the Observer is TARMES [36], which uses the reflected absorber image similarly to the Observer. However, TARMES requires that the collector is oriented at 0° facing the horizon with the camera positioned at a distance of at least 100 times the collector focal length. Therefore, TARMES is unable to measure the optical alignment at normal operating orientations or as a function of the collector orientation. TARMES uses a laser distance meter to measure the absorber position, which requires multiple measurements along the absorber length to accurately characterize absorber sag. The difficulty of positioning the laser distance meter to measure the absorber position along the optical axis is not addressed; neither are the complications of laser-probing a highly absorptive surface through the receiver glass. Improvements to TARMES are currently under development in a tool called Qfly, which allows a collector to be measured in any orientation [27]. The preliminary presentation of Qfly suggests that this technique is quite similar to the Observer method presented here; however, the lack of substantive information published about Qfly prohibits a direct comparison. Specifically, Prahl et al. fail to mention how they measure the absorber location or any details related to finding the camera positions or location of the absorber reflection.

The Observer method improves on the TARMES technique in three distinct ways. First, a robust, absorber alignment measurement technique is introduced that allows the absorber position to be measured with the collector in any orientation using a camera. No contact is required with the absorber or receiver glass, and the absorber position is measured along its entire length. Second, a

[1] A field VSHOT tool does exist, but it is largely impractical because testing can only be performed at night, only a column of data across the collector aperture can be taken at a time, and the field system has never been validated.

[2] TOPCAT essentially only measures reflector slope error at one point on each mirror panel; all of the other tools measure the reflector slope error at a much higher spatial resolution.

collector can be measured in any orientation with the camera positioned as close as a few meters to measure a single reflector panel in the laboratory, as far as 30+ m to measure multiple collectors in the field, or anywhere in between to accommodate most testing environments. Finally, a collector need not be rotated during the measurement. A stationary collector can be measured to ensure that the collector shape does not change during the measurement. This allows prototype collectors not installed with a tracking system to be measured with the Observer method.

3.3.2 Industry Development

The Observer tool aims to meet the research and development (R&D) needs of a growing industry. After a couple decades of stagnation, the CSP industry has undergone substantial development. In the past couple years, many projects have entered the contracting, design, and construction phases. Parabolic trough power plants are under construction around the world in Spain, Algeria, Morocco, Italy, Egypt, Chile, India, Italy, and the United States. Spain, in particular, has a significant number of plants operating or under development due to aggressive feed-in tariffs. The power plants in Spain are being designed and built with at least 6 hours of thermal storage. The next major project in the United States is the 280-MW Solana plant, which is under development by Abengoa Solar for Arizona Public Service and is currently under construction.

CSP companies are competing to develop a new, low-cost parabolic trough collector. Innovative designs include alternative reflectors and collector frames. New reflector panels are being developed from metal, instead of glass, with special reflective coatings or highly polished surfaces. Collector frames are being modified to reduce material and installation costs. With all of this new development and innovation in CSP, the research and development teams need a technique to assess the optical alignment of their parabolic trough collectors that can provide immediate feedback on the alignment of prototype collector modules installed in the field.

3.3.3 Economics

As the competition to produce a low-cost parabolic trough collector continues, the effect of collector performance on the cost of electricity cannot be overemphasized. The optical intercept factor has a significant impact on the levelized cost of electricity (LCOE). If the cost of the collector is reduced by 10%, the LCOE decreases by about 2%; however, if the intercept factor decreases by 10%, the LCOE increases by 7%. [1] A reduction in the intercept factor directly affects the amount of solar-thermal energy gained by the absorber. Thus, it is absolutely imperative that cost reductions in the parabolic trough collector do not result in reductions in the optical intercept factor. The Observer method provides the means to verify that new less-expensive collectors maintain accurate optical alignment.

3.3.4 Applications of the Observer Tool

R&D support

Because many new collectors are being designed, industry requires a means to quickly test prototype collectors. Current optical characterization tools are too slow or designed for indoor measurements of single reflector panels. The Observer tool would provide a means by which industry could test the optical alignment of full collector modules in both indoor and outdoor environments. Testing can be performed on a time scale of 15-30 minutes per module. During the collector development phase, the Observer can be used to measure the optical implications of physical adjustments to the collector with real-time feedback.

Effects of gravity loading

There is little experimental work measuring the optical effects of gravity loading on parabolic collectors. As the collector orientation changes throughout the day, the gravitational loading also changes. The effect that orientation plays on the optical performance is of interest in improving current trough designs and developing new designs. Because the Observer tool can measure the

[1] These cost figures are based on simulations run with the System Advisor Model (SAM), a performance and finance model for renewable energy technology developed at NREL that is publicly available [25].

optical alignment in any orientation, a collector can be tested in multiple orientations to determine if its optical alignment changes due to changing gravitational loads.

Installation quality control

Because many collectors are being designed to be nonadjustable, correct installation is key to future performance. During construction of a plant, the Observer tool could be used to quickly check a few collectors in each row after installation to ensure that everything is properly aligned. An error found in any row could save considerable time and effort if identified and corrected before installing additional rows. The Observer tool would provide a guarantee for all invested parties that the collectors are being installed accurately.

Troubleshooting

At parabolic trough power plants, there are typically temperature measurement devices monitoring the inlet and outlet temperature of the HTF to each loop in the field. If temperature measurements indicate a drop in performance of a particular loop in the solar field, the Observer tool would be able to quickly identify if the drop in performance were due to optical misalignments or rule out optical misalignments as the cause.

Full-field performance evaluation

The Observer tool could be used to take sample measurements of collector optical alignment throughout an entire solar collector field. Statistical analysis would then be used to estimate the intercept factor for the entire solar field, providing the operators, investors, and utilities with an accurate performance assessment.

Chapter 4

Previous Work

Optical testing has a long history dating back to the development of the first optical devices. However, due to the large scale of parabolic trough collectors, only a small range of traditional optical techniques can be applied. A review of traditional optical testing can be found in Appendix A. Of the many optical testing methods, there are five main techniques currently applied to measure the optical alignment of solar collectors: laser scanning, photogrammetry, fringe reflection, flux measurement, and reflected-absorber image analysis.

Laser scanning takes data one point at a time and is too slow and ill-suited for field work. Photogrammetry allows optical characterization of collectors in all orientations; however, the setup is too time-intensive for field work. Photogrammetry also measures the reflector position instead of the reflector slope, which is of greater interest. Fringe reflection is the fastest technique and provides high-resolution, high-accuracy data; however, for parabolic troughs, it is ill-suited for field testing because of the need for a large screen on which to project sinusoidal patterns. Flux measurement attempts to measure the solar flux at the absorber, which could provide the most accurate information; however, the size and shape of a cylindrical receiver as well as the difficulty in accessing the absorber, limits the use of flux measurement. The work most relevant to this research falls under the reflected-absorber image analysis category. Prior work using the reflected-absorber image technique is described below, along with the main differences from the Observer method. Additional information on the techniques of laser scanning, photogrammetry, fringe reflection, and flux measurement is located in Appendix A.

4.1 Distant Observer Method

It was first recognized in 1981 by Wood [41] that a great deal of information could be ascertained by analyzing the reflection of the absorber in a parabolic trough concentrator. Just as parallel rays from the sun are reflected off a parabolic trough onto the absorber, so are the lines of sight from an observer reflected onto the absorber tube. Thus, an observer aligned with the optical axis of the collector sees an enlarged image of the absorber on the reflective surface. Wood's method uses the shape of this reflected image to ascertain information about the optical performance of the collector by introducing the concept of an acceptance window (see Section 5.1).

Wood's method examines theoretical one-dimensional slices across the aperture of the collector observed from different incidence angles with respect to the collector optical axis. Wood proposed photographing a field of collectors from a sufficiently far distance such that the rays from the camera could be assumed parallel. At this far distance, he proposed using an airplane to quickly determine the overall optical alignment of a full collector field. However, the limitations of camera resolution and the difficulty and expense involved in obtaining an aerial platform in 1981 prevented Wood from performing any experiments at sufficiently far distances.

Wood's observations of how the acceptance window changes based on collector optical alignments form the foundation for the Observer method presented here; however, his proposal to place the observer at a far distance from the collector is unnecessary and introduces further complications. By locating the camera (observer) close to the collector, the uncertainty in the optical alignment measurements is minimized. The term *Observer* method is used to give credit to Wood's original idea; the term *Distant* is dropped to de-emphasize the idea that the observer must be located far from the collector.

4.2 TOPCAT

Diver et al. at Sandia National Laboratories used Wood's Distant Observer method to perform a qualitative alignment of the mirror facets of a single LS-2 module [8]. Digital photographs of the

collector were taken from the ground 460 meters away while washers were added to the mounting points on each mirror to correct its alignment. The alignment was adjusted until the reflected image of the absorber tube filled each mirror facet as fully as possible. Figure 4.1 shows the Distant Observer image before and after alignment.

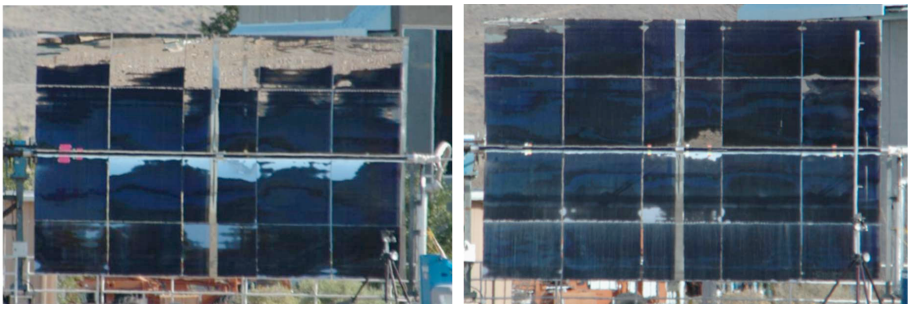

Figure 4.1: Sandia National Laboratories Distant Observer method: before alignment (left) and after alignment (right) [8]

Diver et al. have also developed an up-close alignment tool: Theoretical Overlay Photographic Collector Alignment Technique (TOPCAT) [8]. This method uses Wood's theory that information about the mirror alignment can be obtained from close-up photography of a parabolic collector. Sandia has designed a mast on which five cameras are spaced vertically. The collector is first aimed facing the horizon. One camera is aligned at the collector vertex and the other four cameras are each aligned with one of the mirror facets on a classic parabolic collector. Each camera simultaneously takes a photograph of the reflected absorber image in its respective mirror facet. The center camera is used to produce an ideal theoretical position for the reflected absorber image in each of the four mirrors. The other four cameras photograph the actual position of the reflected absorber image in each mirror. A prescription is then calculated to determine how many washers should be added to each of the mounting points to match the actual to the theoretical reflected absorber image by tilting the mirror. The camera apparatus is mounted on a truck that can drive along the rows of collectors to determine mirror alignment diagnostics and prescriptions for each collector.

TOPCAT assumes that the absorber is located at the focal point of the collector and attempts to align the mirrors to the absorber. Likewise, it does not measure the slope errors across a mirror

facet, but rather, measures the slope error at a single point on each mirror panel and asssumes a constant slope error across each mirror panel. TOPCAT can only be used to measure alignment for the classic segmented-mirror collector and cannot be applied to the new generation of collectors that use a single sheet of metal across the aperture as the reflector. The collectors must be characterized in the horizon-facing position, which is not representative of typical operating conditions.

4.3 TARMES and Qfly

Ulmer et al. at the German Aerospace Center[1] (DLR) have successfully implemented a quantitative variation of Wood's method to measure slope errors of parabolic troughs from the reflected absorber image [36]. TARMES (Trough Absorber Reflection Measurement System) takes a series of high-resolution digital photographs from the ground as the collector is rotated. The absorber position is measured with a laser distance meter. The results provide the reflector slope errors for a full collector and have been compared to photogrammetry results. In this method, the camera is located on a tripod 100 focal lengths from the collector (about 150 meters for typical geometries). The collector is then rotated about 5° to cover the entire acceptance angle while a series of digital photographs is taken. Figure 4.2 shows photographs taken by DLR of the collector with the reflected image of the absorber visible. Ulmer et al. acknowledge that "the measurements are limited to horizontal collector position and unobstructed line of sight from a large distance" [36].

TARMES requires a long unobstructed line of sight, which limits the field environment in which collectors can be measured. The ground-based measurement from such a long distance limits the collector orientation to a single position at 0° facing the horizon. Also, the collector must be rotated to perform the measurement; so, prototype collectors that are not installed with a tracking mechanism cannot be tested.

QFly is an extension of DLR's TARMES that is under development. QFly operates using a radio-controlled helicopter that moves across a stationary parabolic collector [27]. The camera is located using photogrammetry by placing coded photogrammetric targets around the collector.

[1] DLR has licensed this technology to the spin-off company CSP Services

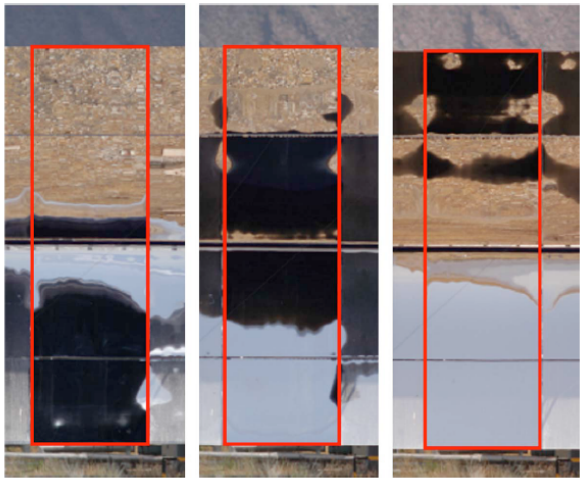

Figure 4.2: Photographs from DLR's absorber reflection method [36]

A commercial photogrammetry package is used to find the coded targets and the corners of the collector to determine the relative orientation of the camera and the collector. QFly has been demonstrated to measure a single parabolic collector and compared to TARMES and photogrammetry with the camera located 30 m above the collector. The method used to locate the absorber is not disclosed by the authors nor are any details regarding the photogrammetry camera location technique and identification of the absorber reflection. Although this method appears to be similar to the Observer method, the lack of details that have been published regarding QFly prohibits a direct comparison. The main observeable difference between the Observer method and QFly is the absorber location method demonstrated in the Observer method. Furthermore, the QFly measurement system appears to be intended as a commercial service endeavor, which signficantly limits publication, access, and collaboration regarding this work.

4.4 VISField

VISfield (Visual Inspection System Field) is a field optical characterization tool developed by ENEA (National Agency for New Technologies, Energy, and Sustainable Economic Development), an R&D facility sponsored by the Italian government [23]. Similar to TARMES, VISfield uses the

location of the image reflection of the absorber to determine the reflector slope errors. VISfield is designed to use a vertically extending mast that scans the camera across the lower half of the collector aperture. The collector must be stationary and positioned in a horizontal orientation. VISfield is designed to measure a 12-m-long collector from 13 m away. The vertical extent of the mast limits the measurement to the bottom half of the collector, which must then be rotated 180° to measure the other half.

The absorber is first aligned to the collector using optical sighting to align each receiver support with the edges of the inner reflector panels. Once the absorber is aligned, the combined errors due to reflector surface slope and absorber position are measured. VISField cannot measure the absorber position, but instead attempts to minimize errors due to absorber misalignment and is thus unable to separate the angular errors due to reflector surface slope and absorber misalignment. As with the other tools, VISField limits the orientation of the collector to 0°, facing the horizon. Because VISField can only measure the bottom half of the collector, the top half of any collector that is unable to rotate a full 180° cannot be tested. Tracking mechanisms rarely allow for a full 180° rotation from horizon to horizon because no energy is collected in these positions. Typically, the collector can only be horizontally oriented in one direction, which enables a stow position to protect the collectors during high winds.

4.5 Summary

There are currently available techniques to measure the reflector slope errors of parabolic reflectors using digital photography of the reflected absorber image. In the past couple years, using the reflection of the absorber has become one of the most popular techniques for optical characterization of parabolic troughs. However, all of these techniques except QFly require the collector to be measured in an atypical orienation facing the horizon. The Observer method allows the collector to be measured in any orientation, providing a more realistic measurement and creating the ability to measure the effects of collector orienation on optical alignment.

The Observer method includes a novel technique to measure the absorber alignment that

improves on the absorber position measurements presented here and which can also be excecuted with the collector in any orientation. Likewise, the Observer method emphasizes the equal importance of absorber position errors compared to reflector surface slope errors. Previous techniques focus exclusively on the reflector slope errors. Finally, the technique used to perform an Observer measurement is presented here in full so that this work can be expanded and improved on in the future.

Chapter 5

Theory

The Observer method is based on the principles of the idealized domain of geometric optics. The large scale of parabolic trough collectors relative to the wavelengths of visible light allows us to neglect the effects of diffraction. The principle of reversibility provides that light rays emanating from the sun that are reflected off the concentrator onto the receiver absorber will follow the same path as light rays traveling from the absorber reflecting off the concentrator back to a distant observer. In theory, a very distant observer aligned with the sun would see what the sun sees if the sun were a point source of energy: an enlarged image of the absorber in the reflector. In practice, the sun has a finite shape, and for the rays entering an observing camera to mimic parallel rays from the sun, the camera must be placed so far from the collector as to make this approach currently unfeasible. However, the same principles can be applied to a camera placed much closer to the collector if the angle of the camera relative to the collector is known. For the Observer method, photographs showing the reflection of the absorber are used to measure transverse errors (along the curvature of the parabola) in both the reflector surface slope and the absorber position.

In this chapter, the theory behind the Observer measurement principles will be explained. The Observer method is only capable of measuring errors in the direction of reflector curvature. The effects of unknown errors along the length of the collector (longitudinal errors) will be presented. The absorber alignment measurement technique that will be used to separate the effects of reflector slope error and absorber position is described. The information obtained from an Observer measurement can be used to calculate the collector intercept factor using one of two methods detailed

here. Finally, the photogrammetry theory required to locate the camera positions and remove lens distortion from the images will be summarized.

5.1 Reflector-Absorber Angles

The Observer method measures the combined angular errors due to reflector surface shape and absorber position termed the reflector-absorber angles. The theory behind measuring the reflector-absorber angles, absorber alignment, and reflector surface slope errors is presented here.

5.1.1 Ideal Collector

The surface of an ideal parabolic trough collector is represented as a parabola with focal length (f). The parabola is given by

$$Z(X) = \frac{X^2}{4f}. \tag{5.1}$$

The absorber is represented as a cylinder with diameter D_{a}, and is ideally located along the focal line of the parabola. The focal line lies parallel to the Y-axis, which is often referred to as the longitudinal direction and is constrained by the collector length (l_{c}). The transverse direction lies parallel to the X-axis and is constrained by the width of the collector aperture (w_{ap}). The optical axis of the collector lies along the Z-axis with the vertex of the collector located at the origin of the coordinate system.

The surface slopes of an ideal parabolic trough in the transverse and longitudinal directions are found by taking the partial derivatives of the parabola with respect to X and Y. The surface normal of an ideal parabola, $\vec{n}_{\mathrm{ideal}}$, is found directly from the surface slope and is written as:

$$\vec{n}_{\mathrm{ideal}} = \begin{bmatrix} -\frac{\partial Z}{\partial X} \\ -\frac{\partial Z}{\partial Y} \\ 1 \end{bmatrix} = \begin{bmatrix} -\frac{X}{2f} \\ 0 \\ 1 \end{bmatrix}. \tag{5.2}$$

The direction of a ray reflected from an ideal parabolic collector is found using Snell's Law:

$$\hat{r_{\mathrm{r}}} = \hat{r_{\mathrm{i}}} - 2(\hat{r_{\mathrm{i}}} \cdot \hat{n})\hat{n}, \tag{5.3}$$

where $\hat{r}_i$ is the unit incident ray, $\hat{n}$ is the unit surface normal, and $\hat{r}_\mathrm{r}$ is the unit reflected ray. Figure 5.1 shows a diagram of Snell's Law in vector form. By substituting the ideal surface normal

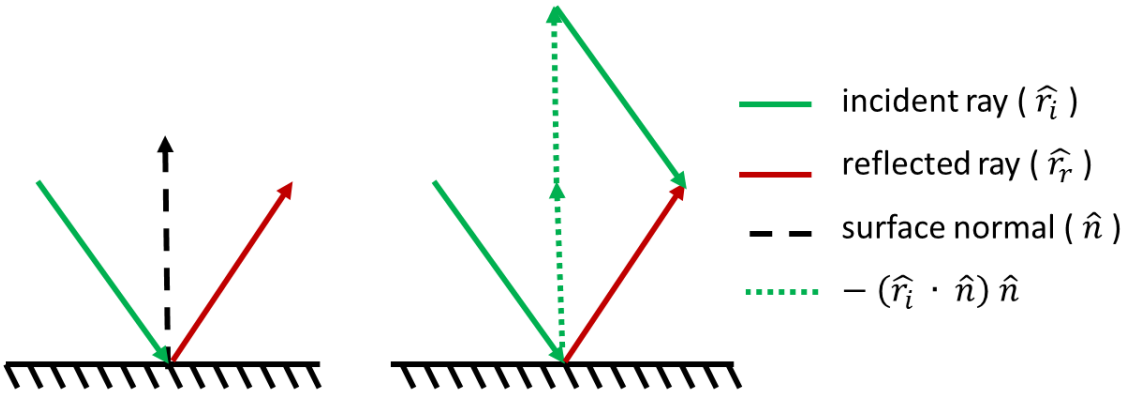

Figure 5.1: Diagram of Snell's Law of reflection

into Eqn. 5.3, it can be shown that all incident rays parallel to the optical axis will be reflected through the focal line of the collector. For a distant observer located at infinity, all incident rays from the observer will be parallel. The angle of the observer with respect to the optical axis of the collector is denoted Φ_c and referred to as the camera angle. If the observer is aligned with the optical axis of the collector ($\Phi_\mathrm{c} = 0$), the absorber reflection will fill the entire aperture. For small, non-zero camera angles, the reflected rays will still be intercepted by the absorber due to its finite diameter; however, as the camera angle increases, rays reflected from the collector rims will begin to miss the absorber because the rim is the farthest distance from the focal point. Thus, the absorber reflection will begin to shrink, but it will always be centered at the vertex of the collector. Figure 5.2 shows the incident rays from a distant observer at two different camera angles.

The maximum angular deviation of an incident ray that will be intercepted by an absorber is referred to as the angular acceptance function, $\grave{\alpha}$. The angular acceptance function depends on the position across the aperture, X, and can be calculated from the collector geometry with

$$\grave{\alpha}(X) = 2\sin^{-1}\left(\frac{D_\mathrm{a}/2}{\sqrt{(Z - Z_\mathrm{a})^2 + (X - X_\mathrm{a})^2}}\right), \tag{5.4}$$

where $(X_\mathrm{a}, Z_\mathrm{a})$ is the location of the absorber relative to the collector vertex, and D_a is its di-

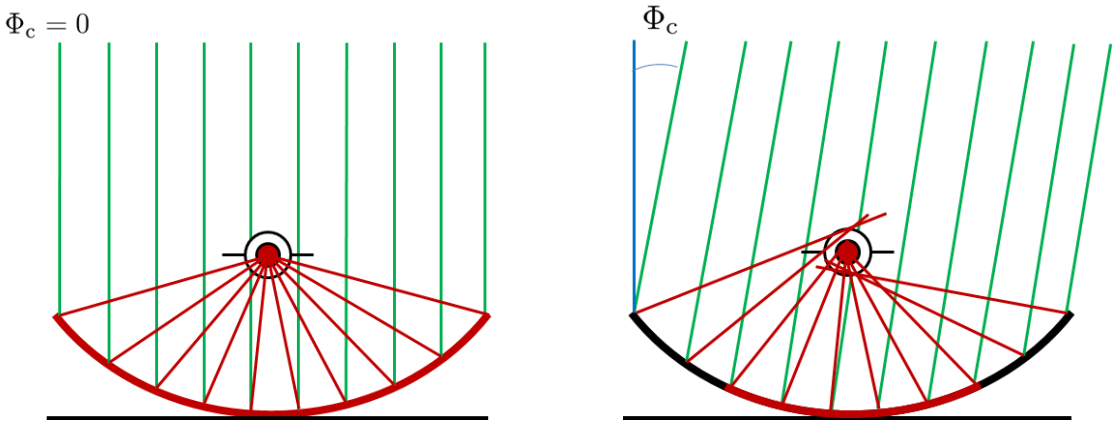

Figure 5.2: Ray trace of a perfect collector for a distant observer with the absorber reflection shown on the collector in red

ameter [2]. Figure 5.3 shows a plot of the angular acceptance function often called the collector acceptance window. The centerline of the acceptance window is the incidence angle of a ray that will be reflected through the center of the absorber. For this ideal case, all rays parallel to the optical axis will be reflected through the center of the absorber, so the centerline is equal to zero. The outer lines are equal to $\pm\dot{\alpha}/2$. For a reflector with perfect specularity, all incident rays within this acceptance window will be intercepted by the absorber. The acceptance window is narrower at the rims of the collector because the distance between the absorber and reflector is greatest here.

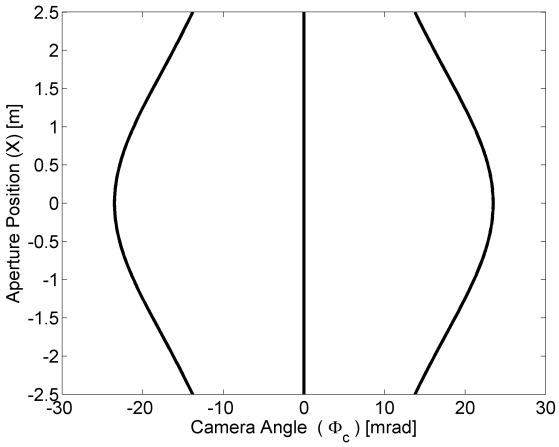

Figure 5.3: Acceptance window of a perfect LS-2 parabolic collector with absorber aligned at the focal point

5.1.2 Reflector Surface Errors

Errors in the reflector surface profile are traditionally modeled as angular errors in the surface slope relative to the ideal parabola and are termed *slope errors*. A slope error is defined as the difference between the angle of measured reflector surface slope and the angle of the slope of the ideal parabola [39]. Reflector slope errors are defined both in the transverse and longitudinal directions; however, because transverse slope errors are of significantly more importance than longitudinal slope errors, only transverse errors will be considered here. The effect of longitudinal errors will be explored in Section 5.2. The term reflector slope error will be used synonymously with transverse slope error.

An error in the angle of the reflector slope is equivalent to the error in the reflector surface normal. The surface normal at a point on the reflector with slope error θ_r in the transverse direction can be found by rotating the ideal surface normal about the Y-axis:

$$\vec{n} = \begin{bmatrix} \cos\theta_{\mathrm{r}} & 0 & \sin\theta_{\mathrm{r}} \\ 0 & 1 & 0 \\ -\sin\theta_{\mathrm{r}} & 0 & \cos\theta_{\mathrm{r}} \end{bmatrix} \vec{n}_{\mathrm{ideal}}. \tag{5.5}$$

Likewise, by Snell's Law, the angle of an incident ray relative to the optical axis that will reflect off a point on the collector with surface normal error, θ_r, and pass through the focal point of the collector is equal to $2\theta_r$. Figure 5.4 shows the relationship between the incident ray, reflector surface normal, and reflected ray. For a distant observer, the camera angle for which rays will be reflected through the focal point is equal to $2\theta_{\mathrm{r}}$. Thus, the centerline of a collector acceptance window for a perfectly aligned absorber is equal to $2\theta_{\mathrm{r}}$. Figure 5.5 shows the acceptance window for a reflector with surface slope errors.

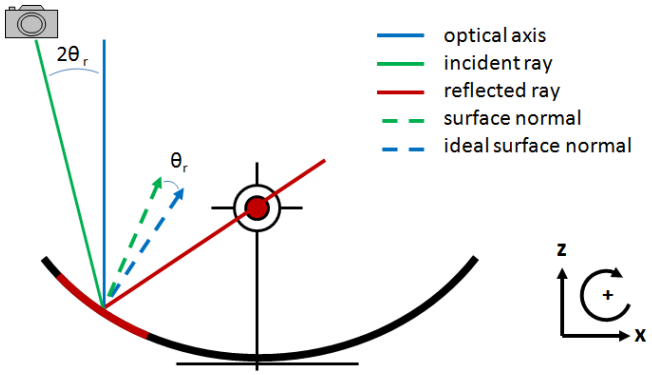

Figure 5.4: Graphical representation of a reflector surface slope error using ray tracing

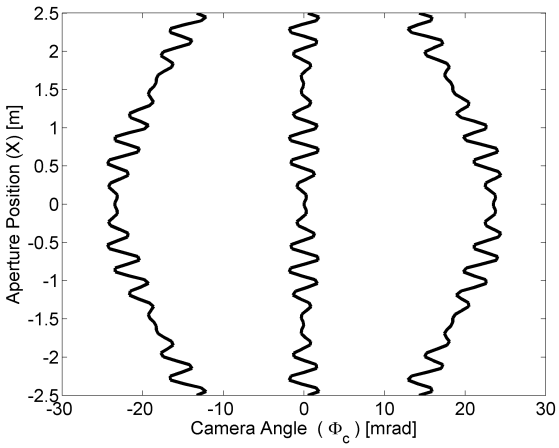

Figure 5.5: Acceptance window of reflector with surface slope errors $\theta_r = \sin(2X)\sin(20X)$ mrad and a perfectly aligned absorber

5.1.3 Absorber Misalignment

Errors in the absorber position are traditionally modeled as offsets from the collector focal point:

$$\begin{aligned} \Delta X_{\mathrm{a}} &= X_{\mathrm{a}} - 0 \\ \Delta Z_{\mathrm{a}} &= Z_{\mathrm{a}} - f, \end{aligned} \tag{5.6}$$

where $(X_{\mathrm{a}}, Z_{\mathrm{a}})$ is the location of the absorber relative to the collector vertex. However, absorber position can also be represented as a set of effective slope errors. The benefit of representing absorber misalignment as effective slope errors is that they can then be combined directly with

reflector surface slope errors. The effective slope error at a point on the collector is equal to half of the incidence angle required for an incident ray to be reflected from an ideal parabola and pass through the center of the absorber instead of the focal point, as shown in Fig. 5.6. The effective

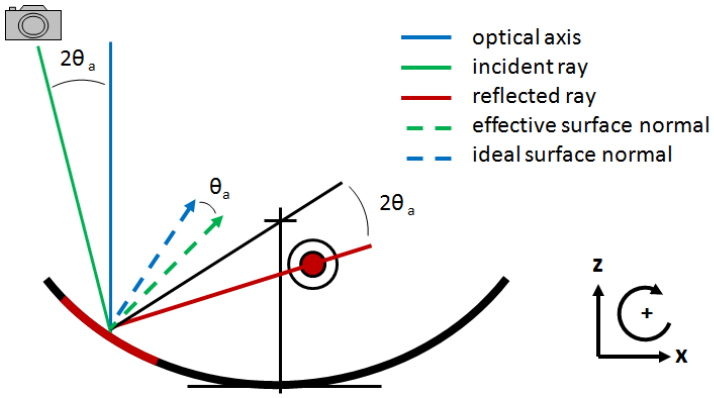

Figure 5.6: Depiction of absorber misalignment represented with effective slope error

surface normal is the surface normal required for an incident ray parallel to the optical axis to be reflected through the center of the absorber instead of the focal point. The effective slope errors (θ_{a}) due to absorber position ($X_{\mathrm{a}}, Z_{\mathrm{a}}$) are calculated with

$$\theta_a(X) = \frac{1}{2}\left[\tan^{-1}\left(\frac{X - X_{\mathrm{a}}}{Z - Z_{\mathrm{a}}}\right) - \tan^{-1}\left(\frac{X - 0}{Z - f}\right)\right], \tag{5.7}$$

where Z is a function of X given by the ideal parabola, Eqn 5.1. The camera angle of a distant observer for which rays will be reflected and pass through the center of the absorber is $2\theta_{\mathrm{a}}$. Figure 5.7 shows the collector acceptance windows for three absorber misalignments. The centerlines of these acceptance windows are equal to $2\theta_{\mathrm{a}}$.

5.1.4 Reflector-Absorber Angles

The reflector surface slope errors and effective slope errors can be combined directly to get the total error due to both rotation of the reflector surface normal and displacement of the absorber from the focal point. Figure 5.8 shows the concept of combining slope errors and absorber positions into a single angular error term.

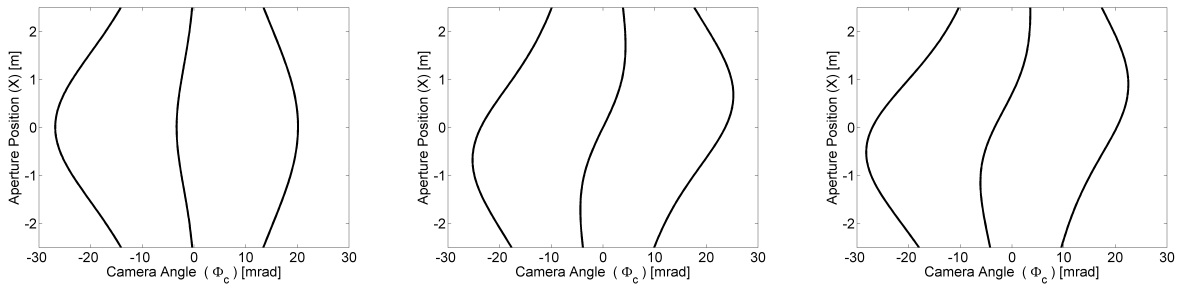

Figure 5.7: Acceptance windows for absorber misalignments of $\Delta X_{\mathrm{a}} = 5$ mm (left), $\Delta Z_{\mathrm{a}} = -10$ mm (center), and the combination of $\Delta X_{\mathrm{a}} = 5$ mm and $\Delta Z_{\mathrm{a}} = -10$ mm (right)

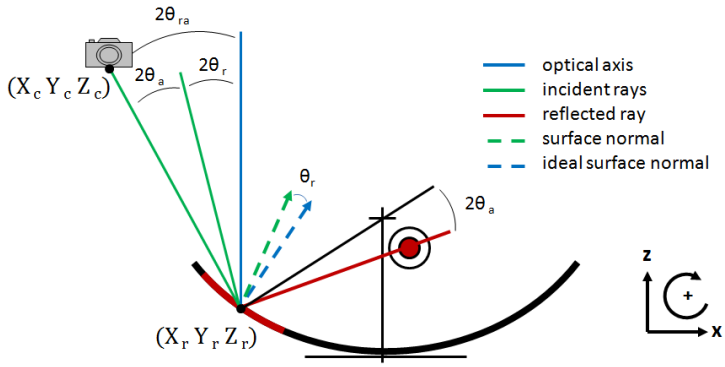

Figure 5.8: Depiction of absorber alignment error combined with reflector slope error

The angular combination of reflector slope errors and absorber position will be termed *reflector-absorber angles*, abbreviated as r-a angles. A reflector-absorber angle, θ_{ra}, is the rotation of the ideal surface normal required at a point on the collector with slope error, θ_r, so that an incident ray parallel to the optical axis will pass through the center of the absorber located at $(X_{\mathrm{a}}, Z_{\mathrm{a}})$. The incidence angle of a ray relative to the optical axis that will be reflected and pass through the center of the absorber is equal to twice the reflector-absorber angle. Figure 5.9 shows three acceptance windows for the r-a angles due to the combination of reflector slope errors and absorber misalignments.

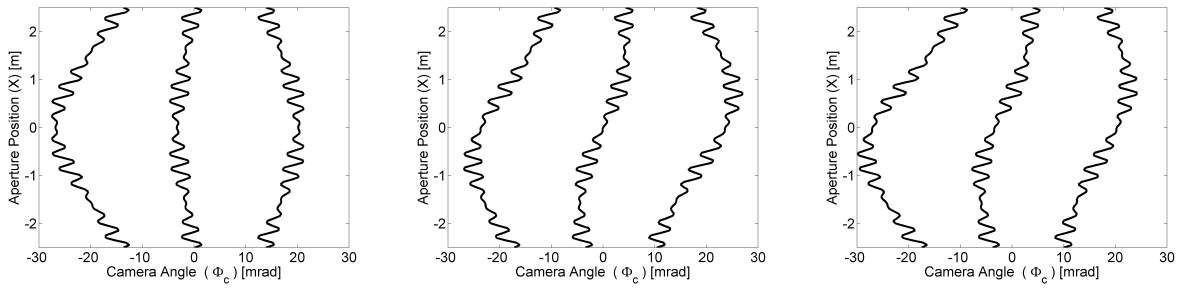

Figure 5.9: Acceptance windows for reflector slope errors $\theta_r = \sin(2X)\sin(20X)$ mrad and absorber misalignments of $\Delta X_\mathrm{a} = 5$ mm (left), $\Delta Z_\mathrm{a} = -10$ mm (center), and the combination of $\Delta X_\mathrm{a} = 5$ mm and $\Delta Z_\mathrm{a} = -10$ mm (right)

5.1.5 R-A Angles Measured by an Observer

Practical application of this method requires that the observer is not located at infinity. As the observer approaches the collector, rays from the observer to the collector are no longer parallel. The camera angle is no longer constant across the collector aperture, but is a function of the aperture position because of parallax. Figure 5.10 shows the change in camera angle across the collector aperture.

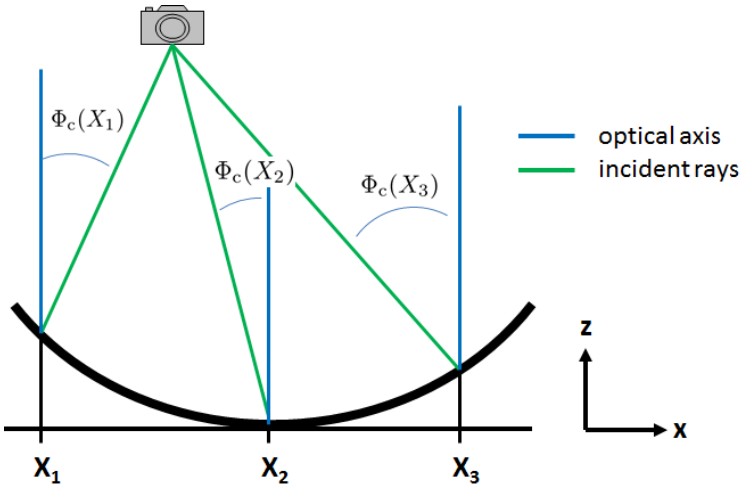

Figure 5.10: Changing camera angle across the aperture for a close observer

The camera angle ($\Phi_\mathrm{c}(X)$) can be calculated for an observer located at $(X_\mathrm{c}, Y_\mathrm{c}, Z_\mathrm{c})$ with

$$\Phi_\mathrm{c}(X) = \tan^{-1}\left(\frac{X_\mathrm{c} - X}{Z_\mathrm{c} - Z}\right), \tag{5.8}$$

where Z can be defined in terms of X as given in Eqn. 5.1. For the observer to be far enough away that it can be approximated as a distant observer located at infinity, we must assume that the incident rays are parallel. That means that Φ_c cannot change significantly across the aperture of the collector. The change in camera angle can be written as

$$\Phi_c(w_{ap}/2) - \Phi_c(-w_{ap}/2) < \frac{1}{2}\theta_\epsilon, \tag{5.9}$$

where θ_ϵ is the maximum allowable error in the reflector-absorber angle measurement. For a 5-m-aperture collector and an allowable error of 2 mrad, the observer must be 5 km away from the collector. At this extreme distance, it is currently infeasible to measure the angle of the observer with respect to the collector with sufficient accuracy. We must, therefore, take into account the change in camera angle across the collector aperture. Likewise, the observer can be positioned close to the collector to allow for measurement in confined spaces.

As seen from a close observer, the absorber reflection will no longer be centered at the vertex of the collector; its location will depend on the position of the observer. Figure 5.11 shows incident and reflected rays from a close observer, as well as the location of the absorber reflection on the reflector.

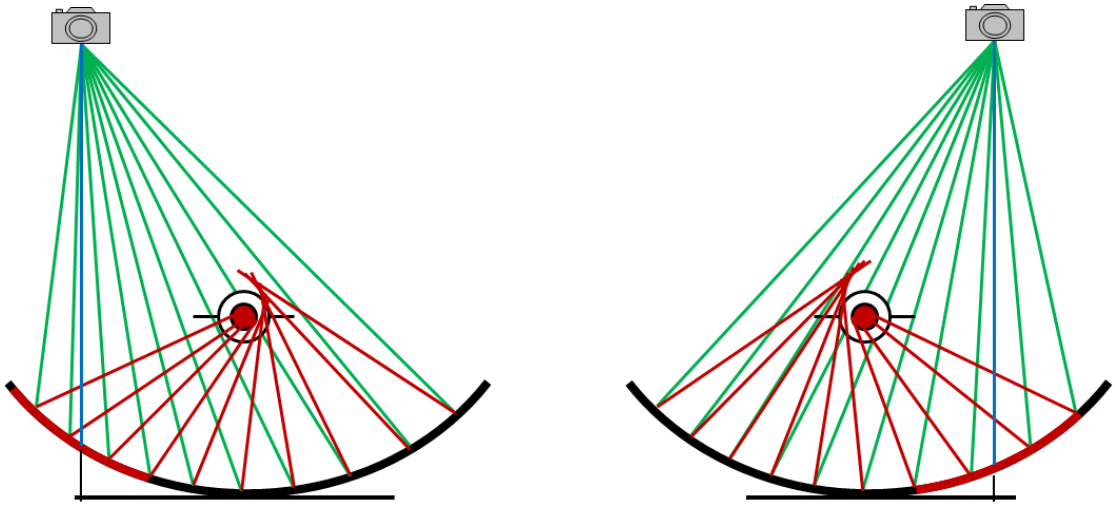

Figure 5.11: Ray-trace diagrams for a close observer located at two different angles with respect to the optical axis of the collector

The angle of incident rays that will be reflected through the absorber can still be plotted for a close observer; however, because the camera angle is no longer constant across the collector, they are now plotted as a function of the camera angle with respect to the vertex of the collector. With this method, each camera angle ($\Phi_c(0)$) represents a different observer position. The resulting plot appears as a tilted version of the acceptance window. To convert the tilted plot into a true acceptance window, the incident rays must be plotted vs. the camera angle with respect to the location of the absorber reflection ($\Phi_c(X)$) instead of the vertex. Figure 5.12 shows the angles of incident rays from a close observer that are intercepted by the reflector for a perfect parabola and absorber alignment (absorber-reflection plot) and the acceptance window created from that plot. As can be seen, the acceptance window created from a close observer is identical to the acceptance window created from a distant observer (Fig. 5.3).

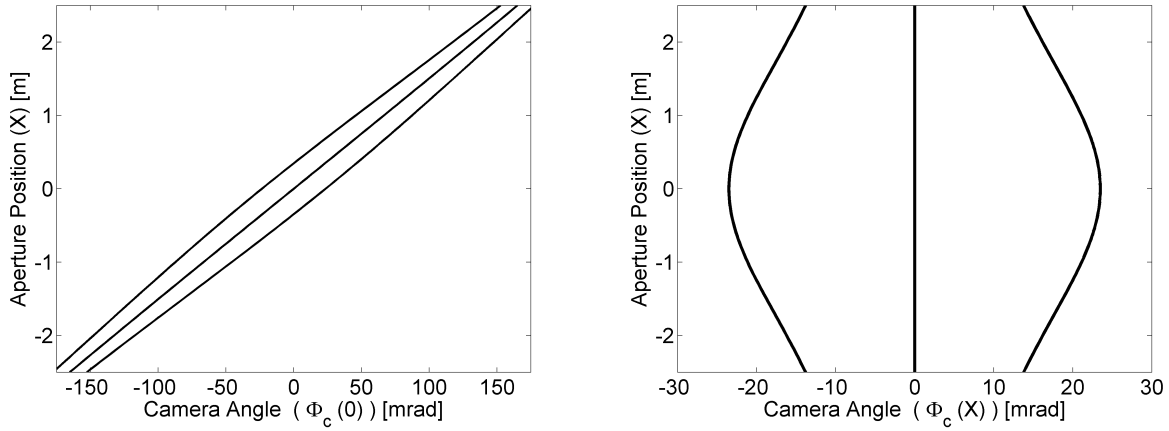

Figure 5.12: An absorber-reflection plot showing the incidence angles from a close observer that will be reflected to pass through the absorber for a perfect parabola and absorber alignment (left) and the acceptance window created from that observer (right)

The reflector-absorber angles can, thus, be measured with a camera (observer) located close to the collector. The camera angle at the center of the absorber reflection is equal to $2\theta_{\mathrm{ra}}$, as shown in Fig. 5.8, and can be calculated with

$$\theta_{\mathrm{ra}}(X) = \theta_{\mathrm{r}}(X) + \theta_{\mathrm{a}}(X) = \frac{1}{2}\tan^{-1}\left(\frac{X_{\mathrm{c}} - X}{Z_{\mathrm{c}} - Z}\right), \tag{5.10}$$

where $(X_{\mathrm{c}}, Z_{\mathrm{c}})$ is the observer (camera) position, and (X, Z) is the center of the absorber reflection

on the parabola. The r-a angle is, therefore, a function of the observer location and the location of the center of the absorber reflection. A series of photographs taken from different camera positions is used to create an acceptance window for the collector. Thus, the essence of the Observer method is locating the camera and the center of the absorber reflection in each photograph. The camera location is found using photogrammetry and the center of the absorber reflection is found using image processing.

5.2 Longitudinal Errors

Due to the linear concentration of parabolic trough collectors, the Observer method is unable to measure longitudinal slope errors independently of transverse slope errors. Photographs of the reflected image of the absorber provide no information about where along the length of the absorber the reflected ray is intercepted. Large longitudinal slope errors can cause errors in the measurement of the reflector-absorber angles and, by extension, in the transverse slope errors. The longitudinal angle between a point on the collector and the camera is referred to as the longitudinal incidence angle of the camera. As the longitudinal incidence angle is reduced, the measurement error in the reflector-absorber angles as a result of unknown longitudinal slope errors is minimized. When there are large longitudinal slope errors, it is preferential, therefore, to locate the camera close to a zero longitudinal incidence angle; however, due to the finite length of the collector, the longitudinal incidence angle at the ends of the collector will always be non zero.

To illustrate the effect of longitudinal slope errors, Fig. 5.13 shows a photograph of the absorber reflection at difference longitudinal incidence angles on several different reflector panels. The reflection of the absorber becomes more wavy for the collectors farther from the camera. The wavy reflection is typically indicative of transverse slope errors so that one would assume the mirrors farthest from the camera have much larger transverse slope errors than those reflectors closer to the camera. However, because the reflectors farther from the camera were photographed at higher longitudinal incidence angles, the wavy reflection is caused by longitudinal slope errors. This was verified by observing that the absorber reflection for the farthest mirrors no longer appeared wavy

when viewed at a zero longitudinal incidence angle.

Figure 5.13: A row of parabolic collectors showing that longitudinal slope errors can appear as transverse slope errors when viewed at non-zero longitudinal incidence angles

To explore the effect of longitudinal slope errors on Observer measurements of r-a angles, a simple model was constructed. An LS-2 type geometry collector with normal random distributions of longitudinal slope errors (2σ = 3, 5, and 7 mrad) was used to represent the range of typical longitudinal errors found on parabolic trough collectors. The corresponding error in the measurement of r-a angles is determined from the difference in the transverse reflected angles off of surfaces with and without longitudinal slope errors. The error in the measured r-a angle (θ_ϵ) is equal to half the difference of the transverse reflected angles:

$$\theta_\epsilon = \frac{1}{2}\left[\tan^{-1}\left(\frac{r_x}{r_z}\right) - \tan^{-1}\left(\frac{r_{0,x}}{r_{0,z}}\right)\right], \tag{5.11}$$

where $\vec{r}$ and $\vec{r}_0$ are the reflected rays with and without longitudinal errors, respectively.

For non-zero longitudinal incidence angles, the measurement error will always be greatest at the rim of the reflector where the reflector transverse slope is the greatest. Figure 5.14 shows 2σ values for the measurement error in the r-a angles for longitudinal incidence angles from $0° - 30°$. For the average case of $2\sigma = 5$ mrad, the incidence angle between the camera and any point on the collector should be less than about 15° to limit the measurement errors to less than 0.5 mrad.

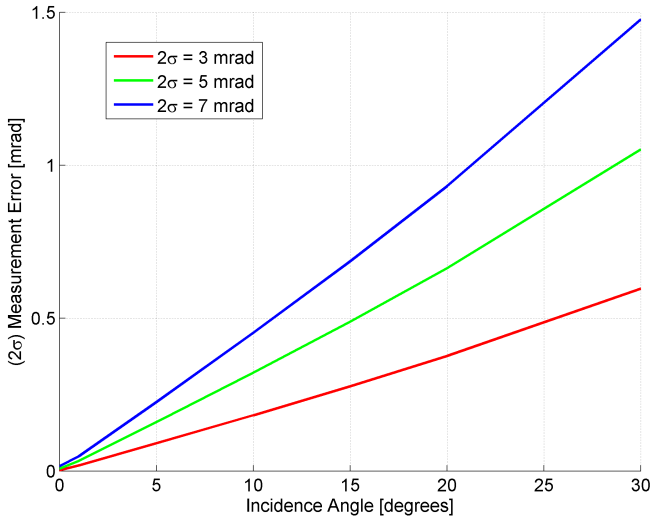

Figure 5.14: Measurement errors in the r-a angles due to longitudinal slope errors

5.3 Absorber Alignment

The Observer method measures the reflector-absorber angles, which are the combination of reflector slope errors and absorber position. To differentiate the two types of errors, the absorber position must be measured independently; then, the effective slope errors can be subtracted from the r-a angles to determine the reflector slope errors. The absorber location is found using triangulation. Triangulation uses multiple angle measurements to find a geometric position. For the absorber position measurement, a camera acts as the angle measurement device and multiple photographs provide multiple angular measurements of the absorber.

To measure the angle between the optical axis of the collector and the absorber, a photograph is used to find the location of the projection of the absorber onto a chosen plane. Although any plane is acceptable, a plane parallel to the aperture and through the design focal line of the collector (focal-line plane) is a logical choice given that we are interested in the position of the absorber relative to the focal line. The location of the camera (X_c, Z_c), location of the projection of the absorber onto the focal-line plane (X_f, Z_f), and location of the absorber (X_a, Z_a) are related by

similar triangles:

$$\frac{Z_\mathrm{c} - Z_\mathrm{f}}{X_\mathrm{c} - X_\mathrm{f}} = \frac{Z_\mathrm{a} - Z_\mathrm{f}}{X_\mathrm{a} - X_\mathrm{f}}, \tag{5.12}$$

as shown in Fig. 5.15. As with the r-a angle measurement, the camera location is found using photogrammetry and the projection of the absorber is found using image processing. The two remaining unknowns are the location of the absorber in two dimensions $(X_\mathrm{a}, Z_\mathrm{a})$. Two camera locations will result in two different projections of the absorber, as shown in Fig. 5.15, that provide a system of two equations with two unknowns that can be solved explicitly for the absorber location. Taking more than two photographs allows for a least-squares solution, potentially improving the accuracy of the measurement. The essence of this method thus reduces to the determination of the location of the camera and the location of the projection of the absorber.

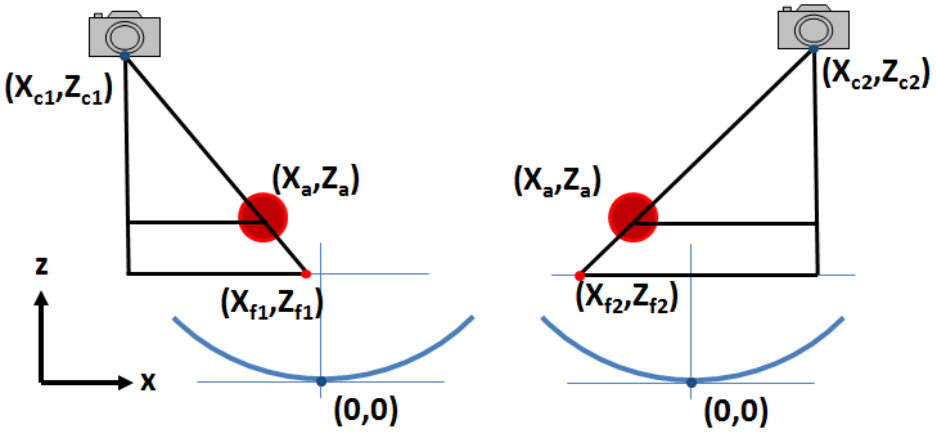

Figure 5.15: Relationship between the absorber location $(X_\mathrm{a}, Z_\mathrm{a})$, projection of the absorber onto the focal-line plane $(X_\mathrm{f}, Z_\mathrm{f})$, and camera position $(X_\mathrm{c}, Z_\mathrm{c})$

Instead, one might expect that the absorber position could be determined from the width of the absorber reflection at different points across the aperture. Although the absorber reflection width does change with absorber misalignment, the change is too small to be resolved. For an LS-2 collector, an absorber misalignment of 3.5 cm results in a maximum change in the absorber reflection width of 1.5 cm, which typically cannot be resolved due to the ambiguity of the absorber reflection edge location in an image. The width of an image is much more difficult to measure than the centerline because it requires finding both edges of the image. The centerline can be measured

more accurately because the exact location of the edges is irrelevant.

5.4 Intercept Factor

The intercept factor is a common metric used to quantify the optical alignment of parabolic trough collectors. The intercept factor of a parabolic trough collector is defined as the fraction of solar energy reflected off the concentrator that is intercepted by the absorber tube for a glass envelope with perfect transmittance. In this section, two methods will be presented for calculating the intercept factor from the reflector-absorber angles: beam-spread analysis and ray tracing. Beam-spread analysis treats both the energy source (the sun) and optical errors as distributions of angular deviations acting on an incident ray. The following derivation of intercept factor using beam-spread analysis is summarized from Bendt and Rabl [2].

The total optical errors due to reflector slope error, absorber misalignment, reflector specularity, and tracking error are represented with the angular error distribution $E(\theta)$, where θ is the angle of an incident ray relative to the optical axis of the collector. The distribution of angular deviations from the source caused by the finite shape of the sun and scattering as rays pass through the atmosphere is called the sun shape and represented with $B_{\text{source}}(\theta)$. It does not matter whether an angular deviation of an incident ray occurs at the source or along the path to the absorber caused by one of the aforementioned optical error sources. Therefore, the total optical errors can be combined with the sun shape to produce an effective source. The effective source includes all angular deviations. The distribution of this effective source is the effective beam spread ($B_{\text{eff}}(\theta)$). The total optical errors are combined with the intensity distribution of the source by convolution. The effective beam spread is calculated with

$$B_{\text{eff}}(\theta) = \int_{-\infty}^{\infty} E(\theta - \theta') B_{\text{source}}(\theta') d\theta'. \tag{5.13}$$

The total flux intercepted by the absorber (q) is found by multiplying the effective source by the angular acceptance function (Eqn. 5.4) and integrating over all incident angles:

$$q = \int_{-\infty}^{\infty} B_{\text{eff}}(\theta) \dot{\alpha}(\theta) d\theta. \tag{5.14}$$

The intercept factor is the total flux intercepted by the absorber divided by the total incident flux at the absorber (I_{b}) as written in

$$\gamma = \frac{q}{I_{\mathrm{b}}}. \tag{5.15}$$

The simple version of beam-spread analysis treats each optical error as a Gaussian distribution [2]. The convolution of the distributions of optical error sources is simplified for Gaussian distributions with

$$\sigma_{\mathrm{total}}^2 = 4\sigma_{\mathrm{r}}^2 + 4\sigma_{\mathrm{a}}^2 + \sigma_{\mathrm{specularity}}^2 + \sigma_{\mathrm{tracking}}^2, \tag{5.16}$$

where σ_{r}, σ_{a}, $\sigma_{\mathrm{specularity}}$, $\sigma_{\mathrm{tracking}}$, and σ_{total} are the standard deviations of the normal distributions, respectively, of reflector slope error, effective slope errors due to absorber misalignment, reflector specularity, tracking error, and the total optical error. Typically, Eqn. 5.16 is written without the factor of 4 on the absorber errors because they are treated as position deviations instead of effective slope errors. As clearly stated in [2], if one or more of the optical error sources cannot be approximated with a Gaussian distribution, the simplified Eqn. 5.16 cannot be used to convolve the optical error sources; instead, the error distributions from each source must be convolved numerically. Zhu has recently expanded on the work of Bendt and Rabl by developing a MATLAB suite of code that performs numeric convolution of the real distribution of combined reflector slope errors and absorber position errors with the distribution of the source [42]. Like Bendt and Rabl, Zhu treats the tracking error and reflector specularity as Gaussian distributions. Using the measured distributions of reflector slope and absorber position greatly increases the accuracy of the intercept factor.

Ray tracing is the other method frequently used to calculate the intercept factor [32], [37]. Ray tracing uses a number of incident rays with the same angular distribution as the source and traces these rays through the reflector-absorber geometry to determine whether or not they are intercepted by the absorber. Ray tracing often requires long computation time because of the need to simulate a large number of rays to obtain a high precision; however, ray tracing can be very accurate if enough rays are used. As in Zhu's work, the reflector slope errors and absorber position

are not approximated with Gaussian distributions. Ray tracing and beam-spread analysis with numeric convolution of the reflector slope and absorber errors have been shown to be comparable in accuracy; however, beam-spread analysis is significantly faster [42].

With either beam-spread analysis or ray tracing, the reflector-absorber angles measured with the Observer technique can be input directly into the intercept factor calculation. For beam-spread analysis, the reflector-absorber angles directly replace the distribution of combined slope errors and absorber position without any loss of accuracy. In ray tracing, the reflector-absorber angles are treated the same as reflector slope errors with the absorber positioned at the focal point. This simplifies the ray-tracing geometry by allowing the effects of absorber misalignment to be included without needing to change the geometry of the absorber relative to the collector.

5.5 Photogrammetry

Photogrammetry is the use of photography to measure geometric properties of objects. In this research, the principles of photogrammetry are necessary to use the camera as a precision measurement instrument. Background on the mathematical model of the camera, development of the collinearity equations, and method of least-squares bundle adjustment are provided in this section.

5.5.1 Camera Model

To use a camera as a measurement tool, it must be well characterized. Traditionally, cameras are modeled using a perspective-center model to which both radial and tangential lens distortions are applied. The perspective-center model is based on the principle of collinearity; that is, a point in object space, the corresponding point in image space, and the perspective center of the camera all lie on a straight line. Object space is the 3D space containing the objects that you are photographing, and image space is the 2D image sensor in the camera. Figure 5.16 illustrates the perspective-center camera model. The object point (X, Y, Z) is imaged by the real camera on the sensor at point (x', y'). This image point must be corrected by the lens distortion components (δ_x, δ_y) so that

it is imaged by the perspective-center camera at point (x, y). The sensor size $(s_x \times s_y)$ is the width and height of the image sensor. The perspective center is the point through which all straight lines pass. The principal point (x_0, y_0) is the intersection of the image sensor and a line perpendicular to the image sensor passing through the perspective center. The focal length (f_c) is the normal distance between the image sensor and the perspective center.

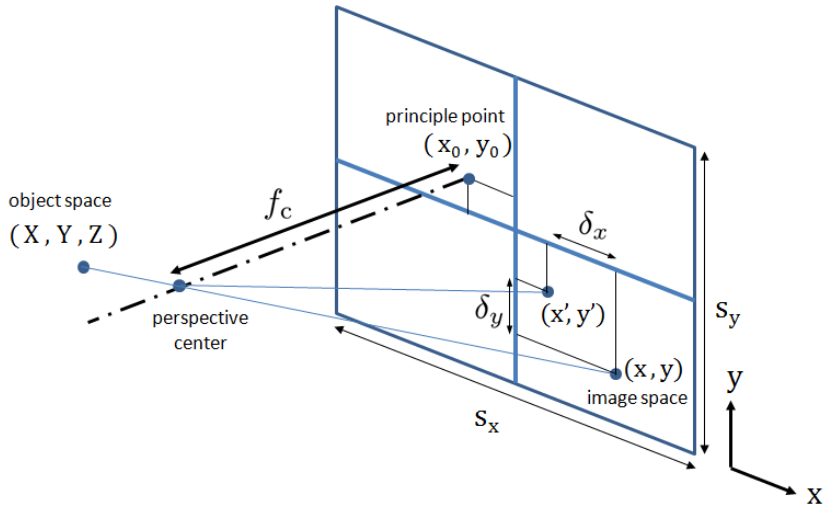

Figure 5.16: Perspective-center model of a camera

The lens distortion quantifies the deviation of rays from the ideal perspective-center model in a real camera and is expressed as deviations (δ_x, δ_y) in the image plane. The primary types of lens distortion are radial distortion and tangential distortion. Radial distortion accounts for the majority of lens aberrations and has radial symmetry, whereas tangential distortion is mainly caused by decentering or misalignment of lens elements. The image points are corrected for lens distortion using Brown's lens distortion model [5]. The radial distortion $(\delta_{x_r}, \delta_{y_r})$ is usually well characterized with three coefficients (K_1, K_2, and K_3):

$$\begin{aligned} \delta_{x_r} &= x'(K_1 r^2 + K_2 r^4 + K_3 r^6) \\ \delta_{y_r} &= y'(K_1 r^2 + K_2 r^4 + K_3 r^6), \end{aligned} \tag{5.17}$$

where any point (x', y') on the image sensor can be described as

$$r = \sqrt{x'^2 + y'^2}. \tag{5.18}$$

The tangential distortion $(\delta_{x_t}, \delta_{y_t})$ is modeled with two coefficients (P_1 and P_2):

$$\begin{aligned} \delta_{x_t} &= P_1(r^2 + 2x'^2) + 2P_2x'y' \\ \delta_{y_t} &= P_2(r^2 + 2y'^2) + 2P_1x'y'. \end{aligned} \tag{5.19}$$

The radial and tangential components of lens distortion are summed to determine the total distortion displacement in each direction:

$$\begin{aligned} \delta_x &= \delta_{x_r} + \delta_{x_t} \\ \delta_y &= \delta_{y_r} + \delta_{y_t}. \end{aligned} \tag{5.20}$$

To correct for lens distortion, the image point locations on a real camera are shifted by the total distortion displacement values to determine their locations on a perspective-center camera.

$$\begin{aligned} x &= x' + \delta_x \\ y &= y' + \delta_y. \end{aligned} \tag{5.21}$$

Therefore, a point in object space (X, Y, Z) will appear on the real camera's sensor in image space at (x', y'), and it will appear on the perspective-center camera's sensor at (x, y). Combining Eqns. 5.17–5.21 yields the lens distortion equations:

$$\begin{aligned} x &= x' + x'(K_1r^2 + K_2r^4 + K_3r^6) + P_1(r^2 + 2x'^2) + 2P_2x'y' \\ y &= y' + y'(K_1r^2 + K_2r^4 + K_3r^6) + P_2(r^2 + 2y'^2) + 2P_1x'y'. \end{aligned} \tag{5.22}$$

Conversion from image space of the perspective-center camera (x, y) to the real camera (x', y') cannot be carried out explicitly because the lens distortion model is nonlinear in x' and y'; therefore, the Newton-Raphson method is used to convert target image locations of a perspective-center camera to a real camera.

5.5.2 Development of the Collinearity Equations

In the perspective-center camera there is no lens distortion, and the rays all pass through a single point (the perspective center) in the camera. With these assumptions, the relationship

between the location of point j in object space (X_j, Y_j, Z_j) and the corresponding point in image space $(x_{i,j}, y_{i,j})$ on photograph i can be described by a projective transformation:

$$\begin{bmatrix} X_j - X_{\mathrm{c}_i} \\ Y_j - Y_{\mathrm{c}_i} \\ Z_j - Z_{\mathrm{c}_i} \end{bmatrix} = \lambda_{i,j} \begin{bmatrix} r_{11} & r_{21} & r_{31} \\ r_{12} & r_{22} & r_{32} \\ r_{13} & r_{23} & r_{33} \end{bmatrix} \begin{bmatrix} x_{i,j} - x_0 \\ y_{i,j} - y_0 \\ -f_{\mathrm{c}} \end{bmatrix}, \tag{5.23}$$

where $(X_{\mathrm{c}_i}, Y_{\mathrm{c}_i}, Z_{\mathrm{c}_i})$ is the camera location of photograph i, and $\lambda_{i,j}$ is a scaling factor. Rearranging Eqn. 5.23 yields

$$\begin{bmatrix} x_{i,j} - x_0 \\ y_{i,j} - y_0 \\ -f_{\mathrm{c}} \end{bmatrix} = \frac{1}{\lambda_{i,j}} \begin{bmatrix} r_{11} & r_{12} & r_{13} \\ r_{21} & r_{22} & r_{23} \\ r_{31} & r_{32} & r_{33} \end{bmatrix} \begin{bmatrix} X_j - X_{\mathrm{c}_i} \\ Y_j - Y_{\mathrm{c}_i} \\ Z_j - Z_{\mathrm{c}_i} \end{bmatrix}. \tag{5.24}$$

The rotation matrix $\mathbf{R}$ is defined as

$$\mathbf{R} = \begin{bmatrix} r_{11} & r_{12} & r_{13} \\ r_{21} & r_{22} & r_{23} \\ r_{31} & r_{32} & r_{33} \end{bmatrix}, \tag{5.25}$$

with components

$$\begin{aligned}
r_{11} &= \cos\phi\cos\kappa \\
r_{12} &= \sin\omega\sin\phi\cos\kappa + \cos\omega\sin\kappa \\
r_{13} &= -\cos\omega\sin\phi\cos\kappa + \sin\omega\sin\kappa \\
r_{21} &= -\cos\phi\sin\kappa \\
r_{22} &= -\sin\omega\sin\phi\sin\kappa + \cos\omega\cos\kappa \\
r_{23} &= \cos\omega\sin\phi\sin\kappa + \sin\omega\cos\kappa \\
r_{31} &= \sin\phi \\
r_{32} &= -\sin\omega\cos\phi \\
r_{33} &= \cos\omega\cos\phi.
\end{aligned}$$

The rotation matrix $\mathbf{R}$ is developed from three consecutive rotations performed about the Z-axis (ω), X-axis (ϕ), and Y-axis (κ), in that order. Alias transformations (rotation of the coordinate system) are used instead of alibi transformations (rotation of the vector). Likewise, the rotations are accomplished with pre-multiplication of the rotation matrix.

Dividing the first and second rows of Eqn. 5.24 by the third yields the well-known collinearity equations. A more thorough derivation of the collinearity equations can be found in [40].

$$\begin{aligned} F = x - x_0 &= -f_c \frac{r_{11}(X - X_c) + r_{12}(Y - Y_c) + r_{13}(Z - Z_c)}{r_{31}(X - X_c) + r_{32}(Y - Y_c) + r_{33}(Z - Z_c)} \\ G = y - y_0 &= -f_c \frac{r_{21}(X - X_c) + r_{22}(Y - Y_c) + r_{23}(Z - Z_c)}{r_{31}(X - X_c) + r_{32}(Y - Y_c) + r_{33}(Z - Z_c)}. \end{aligned} \tag{5.26}$$

The camera location (X_c, Y_c, Z_c) and the Euler rotation angles (ω,ϕ,κ) comprise the external orientation parameters. The focal length (f_c) and principal point (x_0, y_0) comprise the internal orientation parameters.

5.5.3 Linearization of Collinearity Equations

The collinearity equations are linearized to find the external orientation parameters and the object point locations. The linearization is done using a first-order Taylor series approximation. The Taylor series expansion is given as

$$f(x) = \sum_{n=0}^{\infty} \frac{f^{(n)}(a)}{n!}(x - a)^n. \tag{5.27}$$

Removing all terms higher than first order leaves the approximation:

$$f(x) \approx f(a) + f'(a)(x - a). \tag{5.28}$$

For a function of multiple variables, the first-order Taylor series approximation is

$$f(x, y, z, ...) \approx f(x_o, y_o, z_o) + \frac{\partial f}{\partial x}(x - x_o) + \frac{\partial f}{\partial y}(y - y_o) + \frac{\partial f}{\partial z}(z - z_o). \tag{5.29}$$

Taylor expansion of the collinearity equations is written as

$$\begin{aligned} F = x - x_0 \approx F^0 &+ \left(\frac{\partial F}{\partial X_\mathrm{c}}\right)^0 (X_\mathrm{c} - X_\mathrm{c}^0) + \left(\frac{\partial F}{\partial Y_\mathrm{c}}\right)^0 (Y_\mathrm{c} - Y_\mathrm{c}^0) + \left(\frac{\partial F}{\partial Z_\mathrm{c}}\right)^0 (Z_\mathrm{c} - Z_\mathrm{c}^0) \\ &+ \left(\frac{\partial F}{\partial \omega}\right)^0 (\omega - \omega^0) + \left(\frac{\partial F}{\partial \phi}\right)^0 (\phi - \phi^0) + \left(\frac{\partial F}{\partial \kappa}\right)^0 (\kappa - \kappa^0) \\ &+ \left(\frac{\partial F}{\partial X}\right)^0 (X - X^0) + \left(\frac{\partial F}{\partial Y}\right)^0 (Y - Y^0) + \left(\frac{\partial F}{\partial Z}\right)^0 (Z - Z^0) \end{aligned} \tag{5.30}$$

$$\begin{aligned} G = x - x_0 \approx G^0 &+ \left(\frac{\partial G}{\partial X_\mathrm{c}}\right)^0 (X_\mathrm{c} - X_\mathrm{c}^0) + \left(\frac{\partial G}{\partial Y_\mathrm{c}}\right)^0 (Y_\mathrm{c} - Y_\mathrm{c}^0) + \left(\frac{\partial G}{\partial Z_\mathrm{c}}\right)^0 (Z_\mathrm{c} - Z_\mathrm{c}^0) \\ &+ \left(\frac{\partial G}{\partial \omega}\right)^0 (\omega - \omega^0) + \left(\frac{\partial G}{\partial \phi}\right)^0 (\phi - \phi^0) + \left(\frac{\partial G}{\partial \kappa}\right)^0 (\kappa - \kappa^0) \\ &+ \left(\frac{\partial G}{\partial X}\right)^0 (X - X^0) + \left(\frac{\partial G}{\partial Y}\right)^0 (Y - Y^0) + \left(\frac{\partial G}{\partial Z}\right)^0 (Z - Z^0), \end{aligned}$$

where the superscript ^{0} denotes variables evaluated at the initial guess value. Initial guess values are required for the external orientation parameters and object point locations because the collinearity equations are non-linear. The initial guess values are iterated on using the least-squares bundle adjustment described in Section 5.5.4.

5.5.4 Least-Squares Bundle Adjustment

A photogrammetric system of equations consists of a series of photographs taken of a set of targets. The center of each target is represented by an object point. The location of the camera for each photograph is described by the external orientation parameters. To solve the collinearity equations for the external orientation parameters and the object point locations, an iterative least-squares bundle adjustment is performed. Each photograph will be denoted with i and each object point will be denoted with j. The system of two observation equations given in Eqn. 5.30 is expressed in matrix form for a single point on a single photograph as

$$\begin{bmatrix} \dfrac{\partial F_{i,j}}{\partial \vec{\xi}_i} & \dfrac{\partial F_{i,j}}{\partial \vec{\zeta}_j} \\ \dfrac{\partial G_{i,j}}{\partial \vec{\xi}_i} & \dfrac{\partial G_{i,j}}{\partial \vec{\zeta}_j} \end{bmatrix} \begin{bmatrix} \Delta\vec{\xi}_i \\ \Delta\vec{\zeta}_j \end{bmatrix} = \begin{bmatrix} (x_{i,j} - x_0) - F_{i,j} \\ (y_{i,j} - y_0) - G_{i,j} \end{bmatrix}. \tag{5.31}$$

where $\vec{\xi}$ represents the external orientation parameters of the camera $(X_c, Y_c, Z_c, \omega, \phi, \kappa)$ and $\vec{\zeta}$ represents the object point coordinates (X, Y, Z). The partial derivatives of F with respect to the external orientation parameters are written with

$$\frac{\partial F}{\partial \vec{\xi}} = \begin{bmatrix} \frac{\partial F}{\partial X_c} & \frac{\partial F}{\partial Y_c} & \frac{\partial F}{\partial Z_c} & \frac{\partial F}{\partial \omega} & \frac{\partial F}{\partial \phi} & \frac{\partial F}{\partial \kappa} \end{bmatrix}, \tag{5.32}$$

and the partial derivatives of F with respect to the object point coordinates are given as

$$\frac{\partial F}{\partial \vec{\zeta}} = \begin{bmatrix} \frac{\partial F}{\partial X} & \frac{\partial F}{\partial Y} & \frac{\partial F}{\partial Z} \end{bmatrix}. \tag{5.33}$$

We write adjustments to the external orientation parameters $(\Delta\vec{\xi})$ and adjustments to the object point coordinates $(\Delta\vec{\zeta})$ as

$$\Delta\vec{\xi} = \begin{bmatrix} \Delta X_c \\ \Delta Y_c \\ \Delta Z_c \\ \Delta\omega_i \\ \Delta\phi_i \\ \Delta\kappa_i \end{bmatrix} = \begin{bmatrix} X_c - X_c^0 \\ Y_c - Y_c^0 \\ Z_c - Z_c^0 \\ \omega - \omega^0 \\ \phi - \phi^0 \\ \kappa - \kappa^0 \end{bmatrix} \qquad \Delta\vec{\zeta} = \begin{bmatrix} \Delta X \\ \Delta Y \\ \Delta Z \end{bmatrix} = \begin{bmatrix} X - X^0 \\ Y - Y^0 \\ Z - Z^0 \end{bmatrix}. \tag{5.34}$$

Each photograph introduces six unknowns: the external orientation parameters, which are the camera location (X_c, Y_c, Z_c) and the Euler angle rotation of the camera (ω, ϕ, κ). Each object point or target introduces three unknowns: the three point coordinates (X, Y, Z). Two observation equations (the linearized collinearity equations) can be written for each point on each photograph. For M photographs and N targets appearing in each photograph, there will be $6M + 3N$ unknowns and $2MN$ equations. There must be more equations than unknowns to have an over-determined system and use the least-squares bundle adjustment. Additional equations may be written from known geometric constraints. Constraint equations may specify one coordinate location of a target (either X, Y, or Z), a distance between two targets, or another geometric quantity.

An object point constraint equation is incorporated into the least-squares bundle adjustment by simply setting the object point coordinate equal to its constraint. For an object point with

known X-coordinate location (X_p), we write the constraint equation as

$$\left[1\right]\left[\Delta X_j\right] = \left[X_j^0 - X_p\right], \tag{5.35}$$

which is in the same form as Eqn. 5.31 and can be added to the matrix and solved simultaneously with the collinearity equations. Similar equations can be written for known Y- and Z-coordinate locations. A distance constraint equation is written as

$$C = d_{j_1,j_2} = \sqrt{(X_{j_1} - X_{j_2})^2 + (Y_{j_1} - Y_{j_2})^2 + (Z_{j_1} - Z_{j_2})^2}, \tag{5.36}$$

where j_1 and j_2 are two object points used in the distance constraint, and $d_{j1,j2}$ is the measured distance between these two points. A distance constraint is linearized with a first-order Taylor series approximation:

$$\left[\left(\frac{\partial C}{\partial \vec{\zeta}_{j_1}}\right)^0 \quad \left(\frac{\partial C}{\partial \vec{\zeta}_{j_2}}\right)^0\right]\begin{bmatrix}\Delta\vec{\zeta}_{j_1}\\ \Delta\vec{\zeta}_{j_2}\end{bmatrix} = \left[d_{j_1,j_2}^2 - C^0\right] \tag{5.37}$$

and can be directly incorporated into the least-squares bundle adjustment.

All of the observation equations and constraint equations are combined into a single system of equations written as

$$B\Delta = \epsilon, \tag{5.38}$$

where the matrix B contains the partial derivatives of the observation and constraint equations; Δ represents the corrections to the external orientation parameters and the object point locations; and ϵ is the vector of residuals. The goal is to minimize the residuals ϵ through an iterative process. The normal matrix is formulated as

$$N = B^T B, \tag{5.39}$$

and the correction vector Δ is calculated with

$$\Delta = N^{(-1)}\left(B^T\epsilon\right). \tag{5.40}$$

The initial guess values for the external orientation parameters and object point locations denoted

with ^{0} are adjusted as

$$\begin{bmatrix} \vec{\xi} \\ \vec{\zeta} \end{bmatrix} = \begin{bmatrix} \vec{\xi}^0 \\ \vec{\zeta}^0 \end{bmatrix} + \Delta. \tag{5.41}$$

The new approximations to the external orientation parameters and object point locations are used to re-calculate the B matrix and ϵ vector of residuals to get a new correction vector, Δ. This iterative process is repeated until convergence is achieved. The *Manual of Photogrammetry* 4th ed. [40] provides a more complete description, including how to populate the B matrix containing the partial derivatives, as well as an efficient computing algorithm for sparse matrices when each object point is only imaged in a few of the photographs.

5.6 Summary

The photogrammetry theory presented here provides the foundation for the reflector-absorber angles and absorber alignment measurements. Using photogrammetry to find the camera locations, the r-a angles and absorber position can be found from images taken by a close observer. The r-a angles may be used directly in beam-spread analysis or ray tracing to determine the collector intercept factor. In the next chapter, the implementation of the Observer method will be presented.

Chapter 6

Method

The Observer method requires two basic steps: data acquisition and image analysis. The measurement setup required before data acquisition is limited to the target setup. The data acquisition involves taking multiple photographs of the collector from different camera locations and calibrating the camera. For image analysis, the photogrammetry-camera-location technique used for all measurements is presented, followed by the image analysis required to find the absorber reflection and absorber for the r-a angle and absorber alignment measurements, respectively. The method is summarized with the practical considerations necessary to obtain high-quality data.

6.1 Data Acquisition

Before taking images of the collector, the test setup requires the placement or identification of targets on or around the collector. Targets are identifiable features that can be seen in multiple photographs and serve as reference points used to locate the camera relative to the collector. We classify targets as either intentional targets or natural targets. Intentional targets are designed for maximum accuracy and must be mounted on and around the collector before data collection begins. Natural targets are distinguishable features found already on or near the collector that can be used for photogrammetric purposes; natural targets typically result in lower accuracy but reduce setup time. The work contained herein is limited to intentional targets; however, if a robust algorithm is developed for finding natural targets, it can simply be substituted for the intentional target centroiding algorithm used here.

6.1.1 Targets

Intentional targets are designed to maximize the accuracy in the target locations in image space. Spheres are traditionally considered the most accurate intentional targets because the projection of a sphere into image space will be a circle no matter what angle the photograph is taken from. However, spheres make poor targets in outdoor natural lighting conditions because of the uneven distribution of light and shadow on the sphere. For uncontrolled lighting, a solid black circle mounted on a white background makes an excellent target. The black target should be constructed out of special light-absorbing flocked black paper to prevent uneven reflection of light off of the target. When using circular targets, careful attention must be paid to the size of the target; if the targets are too small, accuracy suffers due to poorly resolved target images. If the target size is too large, centroiding error is introduced by the elliptical shape of the targets in the images, as shown in Fig. 6.1 [9], and the nonlinearity of the lens distortion equations. The black circular target images should span about 5–10 pixels.

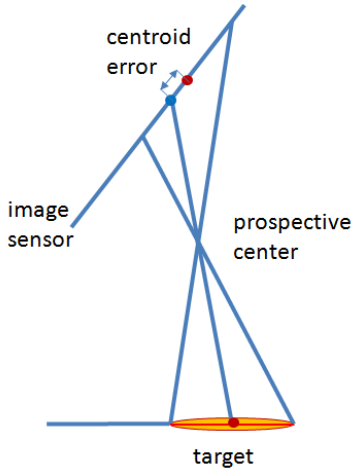

Figure 6.1: Illustration of the centroid error resulting from over-sized targets

Four targets should be placed on the corners of the collector section that is to be measured. These targets should be visible in every photograph. If an entire collector module will be measured in one test, the corner targets are placed on the corners of that module. If instead only a single reflector panel will be measured, the targets should be placed at the corners of the reflector panel.

Typically, the Observer method is used to measure an entire collector aperture from rim to rim. The collector length that can be measured in one test will depend on the field of view of the camera. Figure 6.2 shows recommended target placement when the camera field of view does not include the entire collector length. The corner targets are labeled 1 to 4.

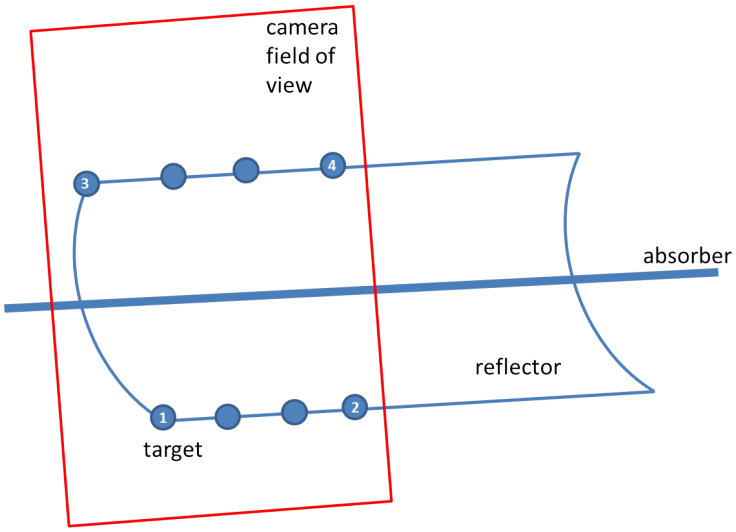

Figure 6.2: Target placement when measuring a portion of the collector length

Placing targets in addition to the four corner targets will increase the measurement accuracy. To maintain an easy setup, additional targets can be placed along the rims of the collector, as shown on Fig. 6.2. For most collector designs, the collector can be rotated to make the rims accessible from the ground, which makes placing targets along the rims straightforward.[1] Extra targets may also be placed on the ground around the collector.

After the targets are placed, the distance measurements along the collector length between corner targets should be taken. In Fig. 6.2, the distance between targets 1 and 2 and the distance between targets 3 and 4 should be measured. Additional distances can be measured to improve the measurement accuracy. A laser distance meter is recommended to measure these distances.

[1] If increased accuracy is desired, an alternative, custom target layout could be developed to maximize accuracy in exchange for a longer, more difficult setup process.

6.1.2 Images

Once the targets are placed, photographs of the parabolic trough solar collector are taken with the camera at different angles with respect to the optical axis of the collector. The collector must have some type of cylindrical absorber to create a reflected image; if a receiver absorber is not installed with the collector, and the reflector slope is the main focus of the test, a dummy absorber may be mounted in place of the actual receiver. In general, each photograph should show the entire collector module and absorber, although with special considerations a single reflector panel may be tested in the laboratory. The photographs should begin with the reflection of the absorber not visible in the collector. As the angle of the camera with respect to the collector changes, the reflection of the absorber should appear on the edge of the aperture and move across the entire aperture until it is no longer visible. Ideally, the angles at which the photographs are taken should be evenly spaced.

There are two options for obtaining the required images: move the camera across the aperture of the stationary collector or hold the camera stationary and rotate the collector. Because collectors are designed to track the sun on a single axis throughout the day, most installed collectors will have this rotational capability. The disadvantage of rotating the collector is that the receiver supports and frame may change shape due to changing gravitational loads as the collector rotates. Additionally, it is difficult to evaluate the collector in an orientation near 90° (facing straight up) because the stationary camera must be positioned directly above the collector at a sufficient distance to image the entire collector. When maximum accuracy is required and when evaluating the effects of gravitational loading, it is recommended to evaluate a stationary collector using a moving camera. Moving the camera across the aperture of the collector can be challenging; methods to achieve this, along with recommended camera specifications, are presented in Section 6.6. Figure 6.3 shows a sample of images taken for a measurement of the reflector-absorber angles.

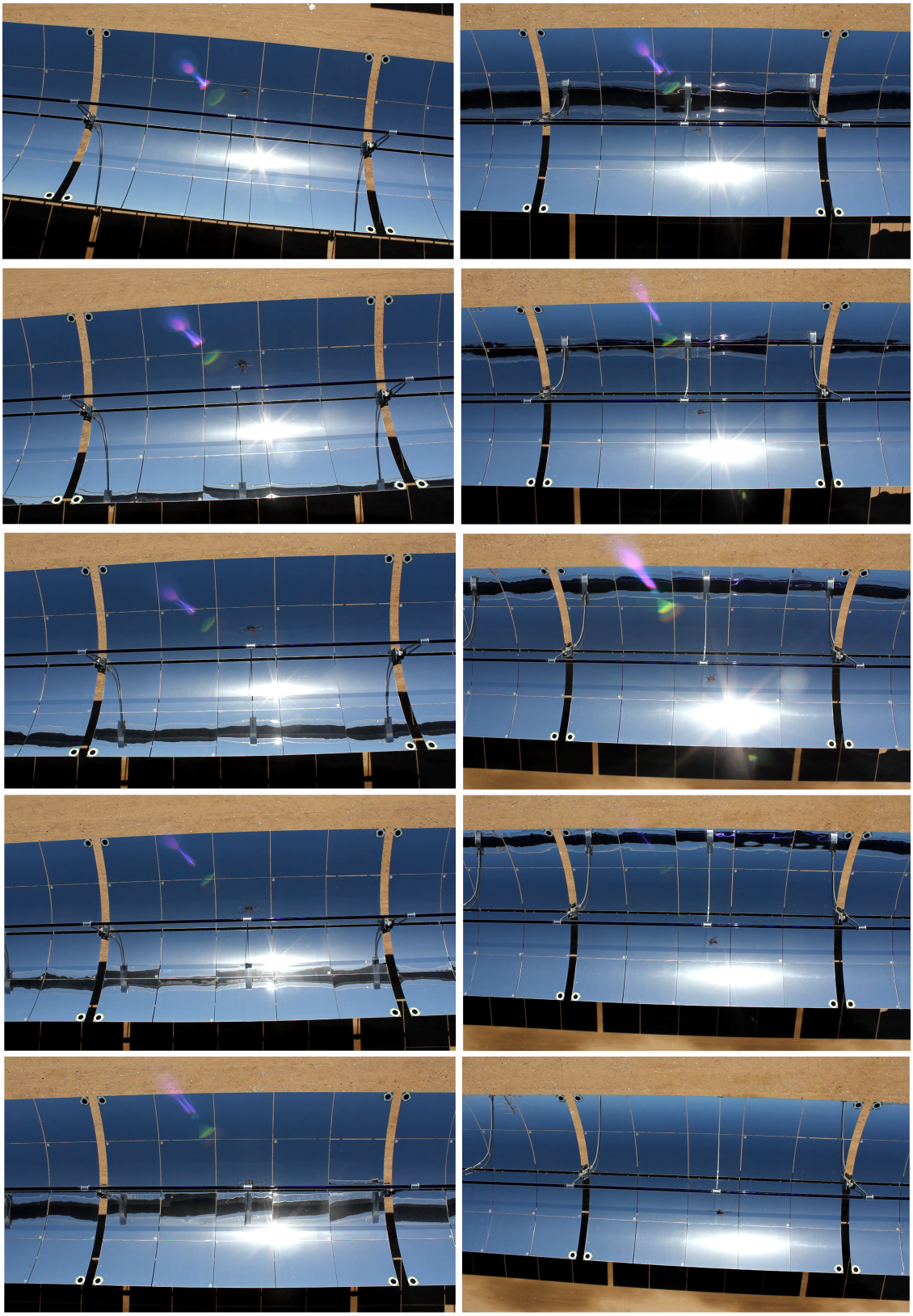

Figure 6.3: Sample images taken for reflector-absorber angles measurement

6.2 Camera Location

The camera location for each image in the series is found using photogrammetry least-squares bundle adjustment as described in Section 5.5. To use photogrammetry, the camera must be calibrated and the target images found in each photograph.

6.2.1 Camera Calibration

The camera may be calibrated before or after the collector images are taken. A complete camera calibration quantifies the ratio of the focal length to the sensor size, the principal point of the camera, and the radial and tangential lens distortion coefficients. Specifications provided by the camera manufacturer for sensor size and focal length are approximations and should not be used in calculations; these values should always be determined with a camera calibration. For the maximum possible accuracy, the calibration should be performed on the same scale and at the same distance as the measurement photographs of the collector. If this is not feasible, the calibration should be performed at a sufficient distance so that the camera can be focused at infinity. This ensures that the focal length of the camera does not change between the calibration and collector measurement.

There are many software packages that can be used to perform a camera calibration. For the Observer method, we have used both a camera calibration toolbox for MATLAB developed by CalTech, which is available online [3] and a commercial software package, PhotoModeler [17]. Both of these software packages supply a calibration grid template that should be printed as large as possible (usually 1 m^2). Photographs of the grid are taken from all sides and the software package is used to analyze the images and produces a camera calibration. The advantage of the PhotoModeler software is that the geometry of the calibration target need not be known, but can be calculated during the calibration process using bundle adjustment; however, this may lead to a less accurate camera calibration than when using a known calibration grid. Other commercial photogrammetry software packages exist that are capable of performing camera calibrations, but experience with the

Observer method is limited to the previously mentioned options. Specific guidelines for the camera calibration are provided with each software package.

6.2.2 Target Image Centroiding

The location of each target image is approximated by finding the centroid of the black circular target image in each photograph. A two-step target centroid process was developed to minimize the amount of user input required. The algorithm begins with user input locations for each target in the first image. The image is cropped to a square region surrounding the target image with size specified by the user. The size of the square region of interest should be large enough to include the entire target with a buffer of about 5–10 pixels around the target. To find the target locations in each subsequent image, the first step is to track the target region from one image to the next. The pixel intensity across the square region including the target is compared with an equal-sized region in the following image that is located within some user-defined distance of the target centroid in the previous image. The location of the square region in the following image is determined as that which minimizes the sum of the absolute value of the difference in pixel intensity with the square region in the previous image. This first step provides a good estimate of the target location in each photograph.

The second step in this process accurately defines the target centroid location. We have developed a contour analysis method that provides a good compromise between accuracy and speed. First, a set of contour lines across the target region are calculated. The contour lines are then filtered using several criteria that increase the likelihood that the contour line lies around the edge of the target. The contour line must be a closed circuit beginning and ending at the same location, and the length of the contour line is restricted relative to the size of the target region. Each contour line that conforms to these filters is then fit with an ellipse using a simple linear least-squares algorithm.[2] All of the real ellipses produced from the contour lines are then filtered

[2] The linear least-squares ellipse fit was originally compared to a non-linear least-squares ellipse fit. The difference in centroid location for the two methods is on the order of 10^{-3} pixels for this application; thus, the linear method was chosen for speed.

by comparing the contour length to the circumference of the ellipse to determine if the contour line is close enough to an ellipse to be included in the final centroid estimate. The centroid is finally determined by averaging the center of all the remaining best-fit ellipses. Figure 6.4 shows an image of a target that is about 20 pixels in diameter (larger than ideal for illustrative purposes). The contour lines are overlaid on the image in blue, and the ellipses fit to those contour lines appear in red. The averaged center of the ellipses is shown as a white dot.

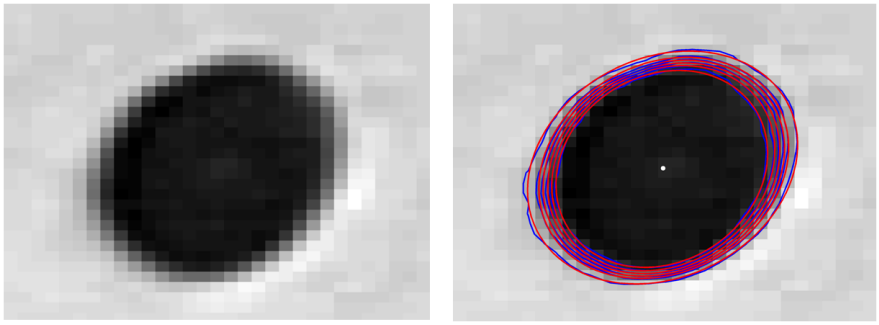

Figure 6.4: Image of intentional target with overlaid contour lines in blue and ellipses in red

6.2.3 Photogrammetry Bundle Adjustment

Once the camera is calibrated and the target image locations found, photogrammetry bundle adjustment is used to find the camera locations. The collector is used to establish the reference coordinate system. A parabolic trough collector is defined by its length (l_c), aperture width (w_{ap}), and focal length (f). By carefully placing targets relative to known geometric locations on the collector (i.e., the rim, vertex, ends of the collector), constraint equations can be used to provide coordinate locations for those targets.

A minimum of seven constraint equations and three targets are required to define the orientation of the coordinate system. Three constraints define the origin or translation of the coordinate system, three constraints define the axes or rotation, and the seventh constraint defines the scaling. For example, if targets are placed on the collector corners as shown in Fig. 6.5, targets 1, 2, and 3 can be used to define the coordinate system. In this case, three constraint equations are

written for z-coordinates, $Z_1 = Z_2 = Z_3 = (w_{ap}/2)^2/(4f)$; two constraint equations are written for x-coordinates, $X_1 = X_2 = w_{ap}/2$; one constraint equation is written for a y-coordinate, $Y_1 = -l_c/2$; and one constraint equation is written for the distance between points 1 and 2, $d_{12} = l_c$. Using these constraints, the coordinate system is referenced to a plane across the aperture of the collector. However, this method leaves the coordinate system very susceptible to errors in the placement of these three targets. An error in the z-placement of a single target will tend to tilt the entire coordinate system. To improve the accuracy of the location of the coordinate system relative to the collector, additional constraint equations should be used along with additional targets, if possible.

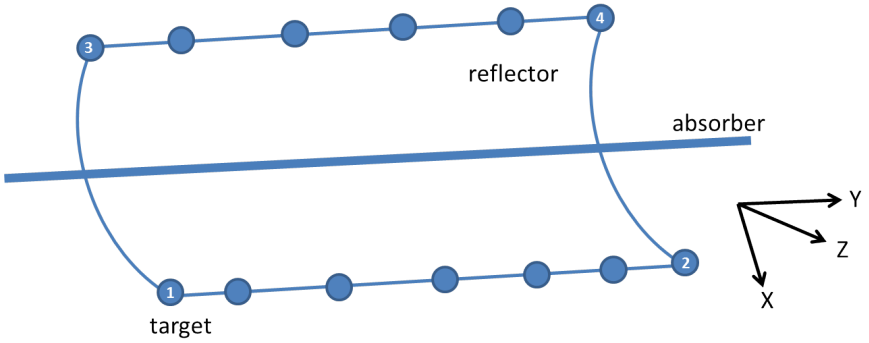

Figure 6.5: Schematic of parabolic collector with targets placed on the corners and along the rims

Targets are placed on the corners and rims of the collector as shown on Fig. 6.5. The location of the collector rims is typically known quite accurately based on the collector design with $X_{rim} = \pm w_{ap}/2$ and $Z_{rim} = {w_{ap}}^2/(4f)$. Constraint equations in X and Z can be written for each target placed along the rim. The result is that the reference plane across the aperture of the collector becomes a least-squares, best-fit plane through all of the targets. Two additional constraint equations are written for y-coordinates at one end of the collector ($Y_1 = Y_3 = -l_c/2$), and two distance constraints are written for the collector length along each rim ($d_{12} = d_{34} = l_c$). No constraint equations are written for additional targets placed on the ground around the collector unless their positions relative to the collector are known.

To determine the number of photographs required to provide an over-determined system of equations for a specific number of targets, we assume that constraints provide seven equations.

Although, a couple dozen or more constraint equations may actually be written, for the proposed setup, constraint equations in excess of seven only provide increased accuracy for the original seven constraints defining the coordinate system. For M photographs and N targets appearing in each photograph, there will be $6M + 3N$ unknowns and $2MN + 7$ equations. A minimum of four targets are needed regardless of the number of photographs. When using four targets, at least three photographs are required. If six or more targets are used, a minimum of two photographs can be used. For the r-a angle measurement, there will always be many more photographs than required for the photogrammetry bundle adjustment; however, if the absorber alignment is being measured independently of the r-a angles, care should be taken to ensure that the minimum number of photographs is met.

6.3 Reflector-Absorber Angles

To measure the reflector-absorber angles, the camera location must be determined as described above, and the location of the absorber reflection must found on the collector. To find the location of the absorber reflection on the collector, the reflector must be identified in each photograph. The extent of the reflector that is being measured constitutes the region of interest on each photograph. All image information outside of the region of interest can be discarded. Within the region of interest, the location of the absorber reflection for a series of photographs can be used to create an absorber reflection plot, as shown for a perfect collector in Fig. 5.12 and described in Section 5.1.5. The reflector-absorber angles can then be calculated from the absorber reflection plot.

6.3.1 Region of Interest

Instead of using traditional image-processing techniques such as edge finding or blob analysis to locate the region of interest designated by the reflector, the reflector is located using the collinearity equations. The reflector surface is assumed to conform to the design parabola. Because the target constraints were developed from that design parabola, the camera location found using

photogrammetry is referenced to the vertex of the design parabola. Points on the design parabola are calculated with

$$Z = \frac{X^2}{4f}. \tag{6.1}$$

The surface of the design parabola in object space is discretized with a uniform grid of points, as shown in Fig. 6.6. This grid of points will be the points at which the r-a angles are measured. If

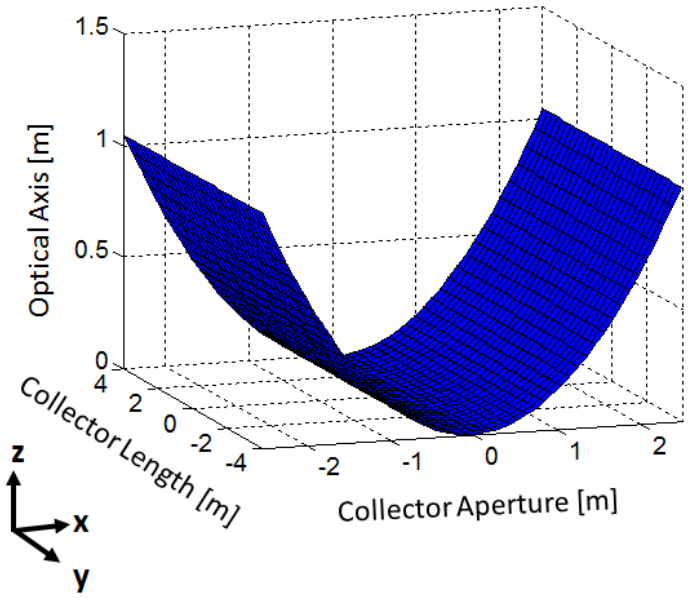

Figure 6.6: Uniform grid of points discretizing the design parabolic collector

the r-a angles are to be measured with maximum spatial resolution, the grid should be fine enough to sample every pixel in the original photograph. Spatial resolution is the distance between the intersection points on the parabola of rays from two adjacent pixels and will be explained in more detail in Chapter 7.

The location of the reflector in image space is found by substituting the point locations shown in Fig. 6.6 into the collinearity equations (Eqn. 5.26) to find the corresponding image points for a perspective-center camera (x, y). The image points are converted to the real camera sensor using the lens distortion model 5.22. Points in image space are then converted to pixels $(x_{\mathrm{I}}, y_{\mathrm{I}})$ by simply

scaling and shifting them:

$$x_{\mathrm{I}} = \left(x' + \frac{s_{\mathrm{x}}}{2}\right)\left(\frac{N_{\mathrm{x}}}{s_{\mathrm{x}}}\right)$$
$$y_{\mathrm{I}} = \left(y' - \frac{s_{\mathrm{y}}}{2}\right)\left(-\frac{N_{\mathrm{y}}}{s_{\mathrm{y}}}\right), \tag{6.2}$$

where N_{x} and N_{y} are the number of pixels across the sensor width and height, respectively, and s_{x} and s_{y} are the width and height of the image sensor. Note that the conversion from image space to pixels for the height of the sensor is flipped because an image is defined with pixel (1,1) in the top left corner. Once the location of the reflector surface is found in pixels, it can be superimposed on the photograph, as shown in Fig. 6.7.

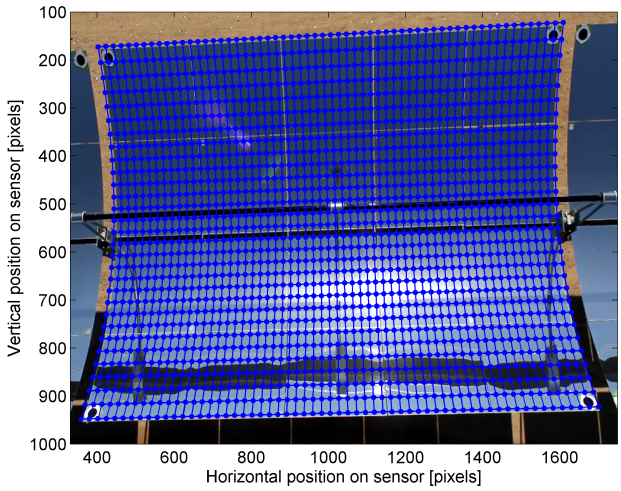

Figure 6.7: A photograph with the uniform grid of points across the reflector surface superimposed on it

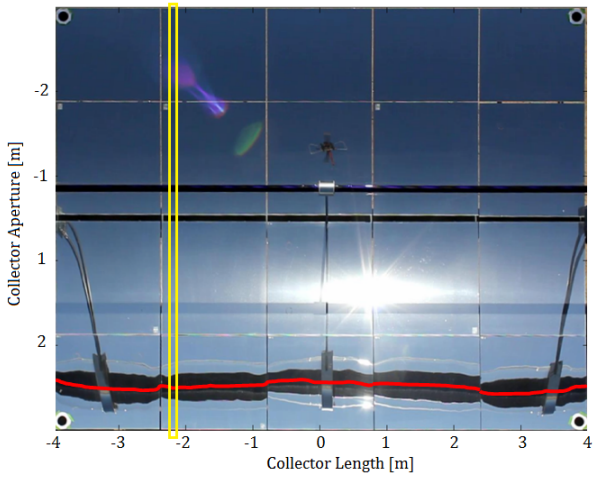

Figure 6.8: Parallax-corrected image of the reflector surface with a single slice along the collector length highlighted in yellow

A new image is created that includes only the reflector region of interest by interpolating the intensity values of the original photograph at the point locations on the reflector. In doing so, the image of the reflector that is created has been corrected for the effect of parallax. The location of each pixel in this image corresponds to a location on the parabolic reflector. Figure 6.8 shows the image of the reflector. The reflection of the absorber can be seen clearly near the bottom of the collector with its centerline highlighted in red. The reflection of the radio-controlled helicopter used to take the photograph can also be seen in the image just above the receiver.

6.3.2 Absorber-Reflection Plot

An absorber-reflection plot shows the location of the absorber reflection in all of the images for a single position along the longitudinal axis of the collector (referred to as a slice). To characterize the entire region of interest, absorber-reflection plots are created for each position along the collector length. The number of slices is equal to the number of points along the Y-axis on the uniform grid. The yellow rectangle in Fig. 6.8 highlights a single slice along the collector length. An absorber-reflection plot is created by taking that same slice from each photograph and combining them into a single image, as shown in Fig. 6.9. The x-axis on top shows that about 400 photographs were used to create this absorber-reflection plot.

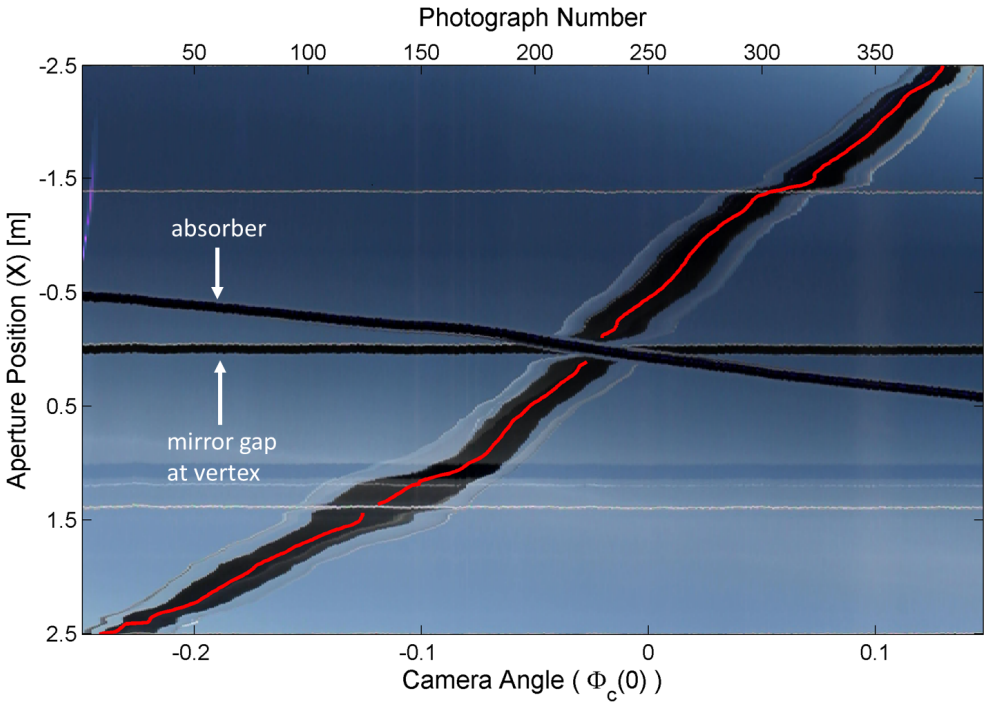

Figure 6.9: Absorber-reflection plot for a single slice along the collector length (highlighted in yellow in Fig. 6.8) for all camera positions with the center of the absorber reflection superimposed in red

The r-a angles are determined from Eqn. 6.3 originally presented in Section 5.1.5:

$$\theta_{\mathrm{ra}}(X) = \frac{1}{2}\tan^{-1}\left(\frac{X_{\mathrm{c}} - X}{Z_{\mathrm{c}} - Z}\right), \tag{6.3}$$

where X and Z are points on the design parabola at which the absorber reflection appears for a corresponding camera location $(X_{\mathrm{c}}, Z_{\mathrm{c}})$. The camera locations for each photograph, i, were found using photogrammetry $(X_{\mathrm{c,i}}, Z_{\mathrm{c,i}})$. The photograph number $i(X)$ at which the absorber reflection appears at point X on the parabola is given by the centerline of the absorber reflection shown in red. Because the camera positions are located close together, the camera position $(X_{\mathrm{c,i}}, Z_{\mathrm{c,i}})$ can be found for non-integer values of i by interpolating between the known camera positions.

6.3.3 Absorber-Reflection Centerline

The centerline of the absorber reflection in each absorber-reflection plot is found using a set of contour lines. The difficulty required to find the absorber-reflection centerline depends on what else the collector is reflecting in each image. On a clear day with no clouds and the collector aimed vertically at the sky, the background reflection will be blue sky, as shown in Fig. 6.9. For these images, finding the absorber-reflection centerline is straightforward. The black absorber labeled in Fig. 6.9 is removed and replaced with white using blob analysis so that it does not interfere with the absorber reflection. Contour lines are then calculated using a marching-squares algorithm for a set of user-defined intensity levels that are based on the image exposure. It is not crucial that the contour lines mark the edge of the absorber reflection, but only that they are equidistant from the absorber-reflection centerline. Figure 6.10 shows an absorber-reflection plot with the absorber blocked out in white and eleven contour lines. In some places, the contour lines are so close together that only the top contour line in red can be seen. From these contour lines, a single contour line on each side of the absorber is selected to represent the edges of the absorber reflection. These two contour lines are selected based on the steepest gradient of image intensity across multiple contour levels and then averaged at each point on the aperture to determine the absorber-reflection centerline.

If the collector is aimed at the horizon and the background reflection includes shadows and objects on the ground, the absorber reflection can be more difficult to locate. The procedure is the same as described above; however, there will most likely be false edges detected in the background

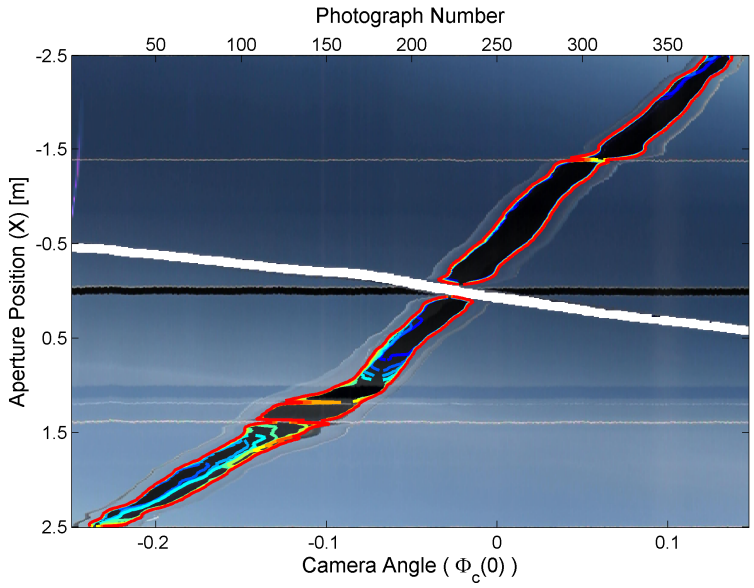

Figure 6.10: Absorber-reflection plot with contour lines superimposed

reflection. In this case, filters are used to remove any false edges. Filters that have proved useful in identifying the correct contour lines include the size of the contour line and the position and angle of the contour line across the image. Additional filters are created as needed for specific sets of images. Once a set of effective filters is identified for a single absorber-reflection plot, it can typically be applied to all of the absorber-reflection plots created during that test. Figure 6.11 shows an absorber-reflection plot with background reflection of both sky and ground. Shadows on the ground make it more difficult to find the centerline of the absorber reflection near the collector vertex as highlighted in red.

6.4 Absorber Alignment

Once the reflector-absorber angles are measured, more specific error information can be obtained by measuring the absorber location and then subtracting the effective slope errors from the r-a angles to determine the reflector surface slope errors. This novel absorber alignment measurement technique was developed specifically for the Observer method; however, it can be used

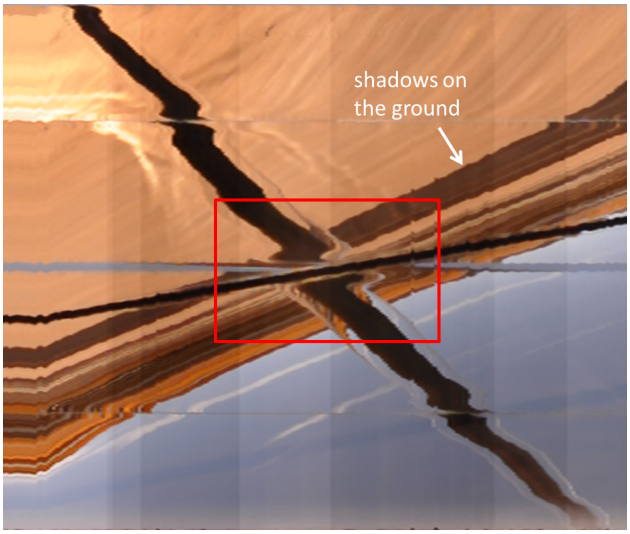

Figure 6.11: Absorber-reflection plot with noisy background reflection including shadows on the ground

independently or in conjunction with measurement of the r-a angles. The absorber alignment is measured by taking at least two photographs from opposite sides of the aperture of the entire collector, including the absorber. The camera locations are found using photogrammetry as described in Section 6.2. Each photograph of the absorber can then be used to measure the location of the projection of the absorber onto the focal-line plane.

6.4.1 Measurement Setup

The camera should be positioned at about 45° angles from the optical axis of the collector at its vertex. The photographs should be taken such that the collector fills as much of the image as possible. A minimum of two photographs, one from each side of the aperture, should be taken as shown in Fig. 6.12.

To position the camera at 45° angles to the collector, some means of elevating the camera must be available. If the collector is oriented straight up at 90° from the horizon, the camera must be elevated on each side of the aperture to reach an appropriate location. The most appropriate equipment for positioning the camera will depend on the collector geometry and the environment around the collector.

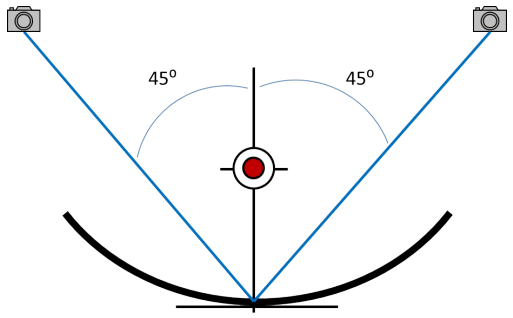

Figure 6.12: Recommended camera positions for measuring the absorber alignment

Photographs taken during the measurement of the reflector-absorber angles may be able to satisfy the requirement for the absorber measurement. The absorber must span a width of at least 35 pixels in each image to accurately locate the absorber (see Section 7.4). Likewise, to triangulate the absorber position along the optical axis (Z_{a}), the angle between camera locations (X_{c_1},Z_{c_1}) and (X_{c_2},Z_{c_2}) must be sufficiently large. Ideally, the angle between absorber photographs should be 90° when possible.

6.4.2 Projection of the Absorber

If the camera location is known, the projection of the absorber onto the focal-line plane can be measured in each photograph. The projection of the absorber onto the focal-line plane is carried out in the same manner as locating the absorber reflection for the r-a angles. A uniform grid of points is created across the plane at the focal line of the collector, perpendicular to the optical axis (focal-line plane), as shown in Fig. 6.6. The parabolic trough reflector is also discretized; although the reflector points are not used to find the absorber location, they are useful here as a visual guide. As with the r-a angles measurement, the grid should be fine enough to sample every pixel across the image of the absorber so that no information is lost.

As with the reflector, the point locations on the focal-line plane in image space for the perspective-center camera are found by solving the collinearity equations explicitly. The image points are then converted to a real camera using the lens distortion model. The image point locations for the real camera are superimposed on each photograph. Figure 6.14 shows a photograph

of a collector on which a uniform grid of points across the reflector and a uniform grid of points across the focal-line plane are superimposed.

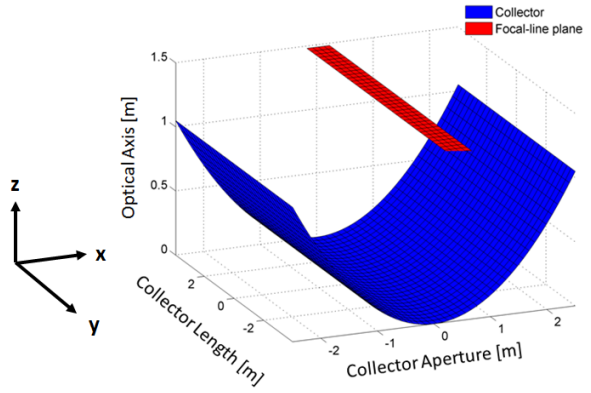

Figure 6.13: Uniform grid of points discretizing the parabolic collector (blue) and the focal-line plane (red)

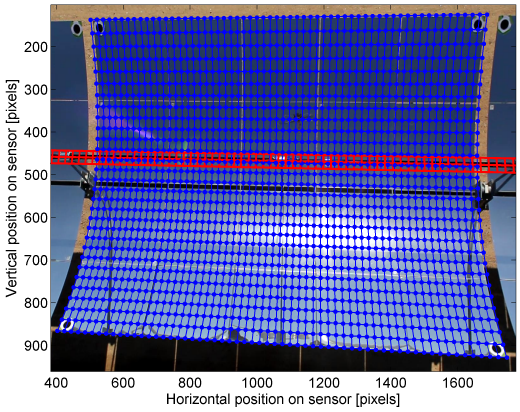

Figure 6.14: Uniform grid of points across the focal-line plane superimposed onto a photograph of the collector (red)

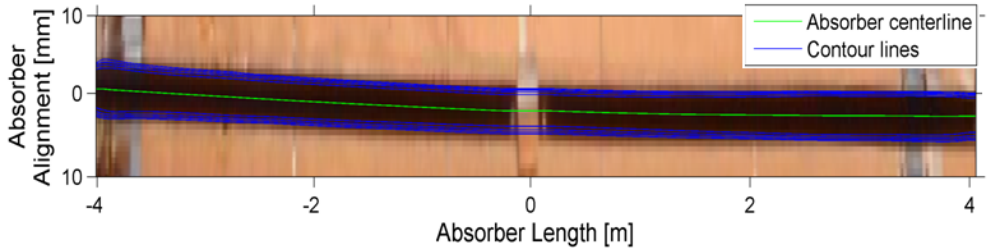

Figure 6.15: Parallax-corrected photograph of the focal-line plane showing the absorber with contour lines and the absorber centerline overlaid on it

The intensity value at the location of each point on the focal-line grid is determined using linear interpolation based on the intensity values in the original photograph. Figure 6.15 shows the resulting image of the absorber at the focal-line plane in which the location of the absorber directly corresponds to the measured offset of the absorber projected onto the focal-line plane (X_{f}).

The centerline of the absorber image is found in the same manner as the absorber reflection centerline was found using contour lines. Once the location of the centerline is known in pixels, it can be directly converted to an offset from the focal line in millimeters because the image of the absorber was created on a known uniform grid. To simplify processing, each photograph of the

absorber is first filtered using blob analysis to remove gaps in the image of the absorber due to the receiver supports. Contour lines are calculated at discrete intensity levels across the image and then filtered to remove noise and false edges. Because there is much less intensity variation across the absorber image than across the absorber reflection image, all of the remaining contour lines are averaged to find the centerline of the absorber. Figure 6.15 shows the image of the absorber overlaid with the final contour lines and the averaged centerline.

The absorber location $(X_\mathrm{a}, Z_\mathrm{a})$ at each point along the length of the collector is found by substituting each camera position $(X_\mathrm{c}, Z_\mathrm{c})$ and location of the absorber projection $(X_\mathrm{f}, Z_\mathrm{f})$ into Eqn. 5.12 to create a system of linear equations and then solving for the absorber position using the least-squares method.

6.5 Reflector Slope Errors

The reflector surface slope errors can be calculated from the measured r-a angles and absorber position with:

$$\theta_\mathrm{r} = \theta_\mathrm{ra} - \theta_\mathrm{a}. \tag{6.4}$$

Once the reflector slope errors are known, measurement error can be reduced by fitting a quadratic surface to the reflector slope. This technique is used by other reflector surface slope measurement tools including both VSHOT and SOFAST and is important when testing a single reflector panel oriented arbitrarily in space. For a single panel, it is difficult to create a reference plane to the design parabola using photogrammetry targets as is done for full collector modules. Likewise, the shape of a single reflector panel that is not mounted on its intended frame may be largely unknown because the frame is essential in creating the parabolic shape. To avoid measurement errors caused by the unknown shape of the reflector panel, the slope errors are minimized by fitting a second-order polynomial to the surface. The slope errors become the difference between the measured reflector slope and the slope of the second-order polynomial. An iterative, least-squares method is used to perform this fit, as described in Appendix B.

This best-fit quadratic technique is useful in the laboratory when measuring a single reflector panel whose shape is largely unknown. However, a simpler fitting technique can be applied when the reflector shape is well known, but the targets cannot be placed accurately with respect to the aperture plane of the collector. In this case, the measured slope errors can be fit to a parabolic surface by rotating the parabolic collector about its longitudinal axis. A rotation of the entire coordinate system about the longitudinal axis of the parabola will appear as a bias slope error. To fit the reflector slope errors to the design parabolic surface rotated about the longitudinal axis, the average slope error is calculated and subtracted from the reflector slope errors, resulting in the best-fit slope errors based on the rotated design parabola.

Whichever fitting technique is used on the reflector surface slope errors, it is essential to remember than no fitting should be performed directly on the reflector-absorber angles. Data fitting should only be applied to reflector surface slope errors. Performing a quadratic best-fit on measured r-a angles tends to remove most of the effective slope errors due to absorber misalignment, while introducing erroneous errors at the corners of the collector. Even performing a simple rotational fit about the longitudinal axis may remove errors due to absorber misalignment. An absorber misalignment along the transverse axis causes a non-zero average of effective slope errors across the entire collector that will contribute to a bias error in the r-a angles.

6.6 Practical Considerations

To use the Observer method in practice, several practical issues must be addressed. Positioning the camera relative to the collector is non-trivial. Several different mounting platforms have been tested to determine their effectiveness; the lessons learned are presented here. Likewise, general guidelines are presented here to aid in selecting a camera. Most importantly, care should be taken with the types of camera lenses and sensors used for Observer measurements.

6.6.1 General Camera Requirements

The main hardware requirement for Observer measurements is the digital camera. The specific camera requirements vary greatly from application to application. For example, the type of camera used for measuring a collector in the laboratory where the camera can be positioned with high precision and measurement time can be extended may be quite different from a camera used to measure multiple collectors from a radio-controlled helicopter in the field. However, there are several requirements to keep in mind when selecting a camera, the most important of which is a fixed-focal-length lens. It is imperative that the focal length of the lens not change between photographs. If you are using a variable focal-length lens, the lens must be fixed at a single focal length and maintain that focal length throughout the entire measurement, even when turning on and off the camera. If the camera will be used for multiple applications in which different focal lengths would be needed, a camera with interchangeable lenses should be selected. As a general guideline, the shortest focal-length lens without obvious fish-eye distortion should be used. A wide-angle lens allows a wider angle between photogrammetry targets visible in the camera's field of view (FOV), improving the accuracy of the camera location measurement, which is crucial to attaining low measurement uncertainty. The Observer method has been implemented successfully with a 12-mm focal-length lens.

Equally as critical to the Observer method is the camera sensor. Ideally, a large-format sensor should be used. Nikon and Canon typically use 23.6 × 15.6 mm and 22.2 × 14.8 mm sensors in their digital single-lens reflex (DSLR) cameras, respectively. Using a large-format sensor contributes to a wider FOV and tends to reduce noise. There are two types of digital camera sensors currently in use: CCD (charge-coupled device) and CMOS (complementary-metal-oxide-semiconductor). Both sensors have proven effective for the Observer method when taking still images; however, CMOS sensors should generally not be used when taking images in video mode. When taking still images, both sensor types use a global shutter; however, in video mode, a CCD sensor uses a global shutter, whereas a CMOS sensor uses a rolling shutter. With a global shutter, the entire sensor is exposed at

the same time. For low shutter speeds, rapid camera movement will cause blur in the image taken with a global shutter. A rolling shutter exposes different portions of the sensor at different times. Typically, the sensor is exposed from top to bottom by rolling the shutter across the sensor so that only part of the sensor is exposed at any point in time. With a rolling shutter, camera movement can result in stretch or compression of the images. Increasing the shutter speed on a video using a rolling shutter will decrease the exposure time for each pixel; however, the extent to which it will impact the time lag between exposing the first and last pixels on the sensor is held proprietary by camera manufacturers. Experience has shown that a global shutter is always preferable to a rolling shutter for the Observer measurement. For applications with a stationary camera and a slowly rotating collector, a rolling shutter may be acceptable. Whenever the motion of the camera or collector cannot be precisely controlled at a very slow, steady speed, rolling shutters should not be used.

The resolution of the camera is another important considerations. The resolution of the camera is the number of pixels across the height and width of an image. A higher resolution camera will typically yield more accurate results for a fixed measurement setup. Specifically, the accuracy in the absorber location measurement in the X-direction depends heavily on the image resolution. When solving for the combination of slope error and absorber errors without need to distinguish between the two types of errors, a lower resolution is acceptable. The impact of camera resolution on measurement uncertainty is explored in detail in Chapter 7.

The frame rate of a camera is the number of images that can be acquired in one second. The frame rate affects the speed at which the images can be acquired. For low frame rates, the image acquisition time can be increased to obtain the same number of photographs as with a higher frame rate so that the uncertainty is unchanged. The frame rate need only be considered if there is no control over the speed of the camera motion or collector rotation or a particularly short measurement time is required.

6.6.2 Camera Mounting Platforms

The greatest flexibility in camera position was obtained by mounting the camera on a multi-axis gimbal on a radio-controlled (R-C) helicopter. With a skilled pilot or sophisticated autopilot, the helicopter can be maneuvered into any position with respect to the collector; the gimbal can then be used to aim the camera at the collector. A stabilization platform on the helicopter greatly reduces vibrations and improves image quality. Using way points, the helicopter can be programmed to survey multiple collectors with minimum required operator control. Sophisticated autopilots can also be used to maintain the orientation of the camera's FOV relative to the collector and maintain a constant camera height. Both a traditional single-rotor, gas-powered R-C helicopter and a selection of smaller multi-rotor electric copters were successful in positioning the camera. The larger, gas-powered, single-rotor helicopter operated more successfully in windy conditions and was able to carry a larger payload for a longer flight time. Figure 6.16 shows a photograph of the most successful R-C helicopter used. This helicopter was constructed and flown by Northwest Aero Pix. The camera can be seen mounted below the helicopter and aimed at the ground.

Figure 6.16: Radio-controlled helicopter designed and flown by Northwest Aero Pix

Significant differences were experienced between R-C helicopters with and without stabiliza-

tion platforms. Without a stabilization platform, the camera cannot be positioned so that the collector fills the FOV because unpredictable motion of the helicopter would frequently move the collector outside the FOV. In this case, the camera must be pointed straight down and no attempt made to track the collector as the camera moves across the aperture. The collector can only fill less than half of the FOV so that the collector remains visible as the camera scans across the collector. Additionally, a wide buffer is needed around the collector to ensure that the collector remains visible. Figure 6.17 shows a collector relative to the FOV for a non-tracking and tracking camera. A sophisticated autopilot and camera stabilization platform made it possible for the operator to

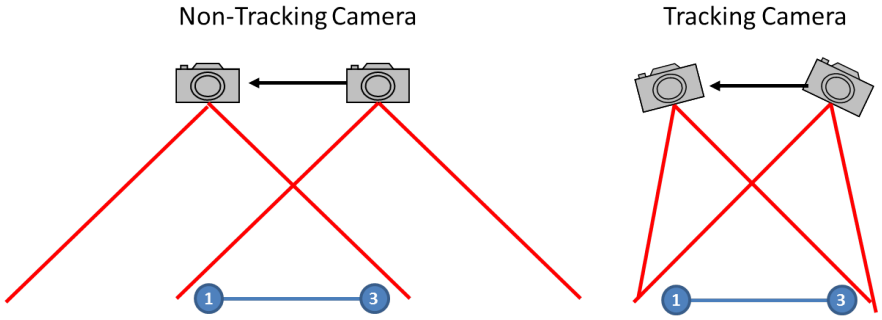

Figure 6.17: The camera's field of view for a non-tracking and tracking camera

track the collector with the remote-controlled gimbal. The camera was thus positioned so that the collector filled a much larger portion of its field of view. A small buffer is still required around the collector to account for small unpredictable movements of the helicopter. Because targets are mounted on the corners of the collector, filling the camera's FOV with the collector increases the accuracy of the camera location measurement and thus reduces uncertainty in the r-a angles.

Success was also achieved positioning the camera with a 50-ft extendable mast attached to a truck hitch. The camera is mounted on the top of the mast in its retracted position about 9 ft above the ground. A radio-controlled gimbal system with wireless image transfer is used to see the camera's FOV, make adjustments to the orientation of the camera, and take photographs. The collector is oriented between 0° and 45° above the horizon, and the mast is deployed vertically while taking photographs of the collector. There is a fairly high level of user involvement required to keep

the camera pointed at the collector because the mast is not especially stable and tends to sway even in low winds; however, with this system, the camera can be positioned so that the collector fills a large portion of the camera's field of view. Using the mast system, a single collector can be surveyed in about 15 minutes. Unfortunately, the geometry of the setup limits the orientation of collectors measured to less than 45° above the horizon. Figure 6.18 shows a photograph of the mast in action.

Figure 6.18: Extendable mast with the camera mounted on a multi-axis gimbal taken at Xcel Energy's Cameo Power Plant

In the laboratory, the r-a angles were successfully measured by mounting the camera on a vertical lift and scanning it across the aperture of a reflector panel. For a panel mounted with its transverse axis parallel to the optical axis, the camera was mounted on a tripod with wheels and scanned horizontally across the aperture. A more permanent measurement setup could be created in the laboratory with a track system mounted on the ceiling that enabled smooth movement of the camera across a reflector facing up. However, this setup has not yet been tested or implemented. Other camera-mounting platforms that have been tested with less success are described in Appendix C.

Chapter 7

Uncertainty Model

7.1 Overview

A detailed photograph generation and analysis code was developed to provide initial validation for the Observer method and to determine how the uncertainty depends on the test parameters. The code generates photographs of the absorber and reflection of the absorber based on user-defined camera parameters, collector design, and known absorber position and reflector slope errors. The computer-generated photographs are then analyzed in the same manner that real photographs would be analyzed to find the reflector-absorber angles, absorber alignment, and reflector slope errors.

7.1.1 Photograph Generation

To generate a photograph, each pixel on the camera sensor is represented by a single ray. The rays are traced from the sensor into a three-dimensional scene containing the camera, collector, and absorber. Each ray is classified as either a hit or miss in each of the following categories:

(1) Hit/Miss the collector

(2) Hit/Miss the absorber directly

(3) Hit/Miss the absorber after reflection off the reflector.

A logical array is created equal to the size of the camera sensor in pixels for each of the above categories. A complete photograph is created from the three arrays using simple logical arguments,

such as a ray that misses the collector or hits the absorber directly cannot hit the absorber after reflection.

Collector design

The collector is composed of a reflector and an absorber that are each defined independently within the same coordinate system. The position of the reflector surface is represented with a second-order polynomial. The slope of the reflector surface is described as a set of slope errors applied to the partial derivatives of the quadratic surface. Because displacement errors between the quadratic surface and the actual reflector shape have significantly smaller effects than slope deviations on the direction of reflected rays, this model provides a good description of the relationship between incident and reflected rays. The general quadratic equation used to model the collector surface is given in Eqn. 7.1:

$$Z(X,Y) = aX^2 + bXY + cX + dY^2 + fY + h \tag{7.1}$$

with

$$|X| \leq \frac{w_{\text{ap}}}{2} \quad \text{and} \quad |Y| \leq \frac{l_{\text{c}}}{2},$$

where w_{ap} is the aperture width, and l_{c} is the length of the collector. For an ideal parabola with focal length (f), the coefficient, a, is equal to $\frac{1}{4f}$ and the other coefficients are all equal to zero. Additional reflector surface slope errors θ_{r} and $\theta_{\text{r,long}}$ in the transverse and longitudinal directions, respectively, are added to the reflector surface model to represent striations or dents commonly found on reflectors.

The absorber is defined by the location of its centerline relative to the vertex of the collector $(X_{\text{a}}, Z_{\text{a}})$ and its diameter (D_{a}). At this time, only straight absorber tubes located parallel to the focal line are modeled due to the added complexity of mathematically describing a rotated cylinder. The receiver glass envelope is, likewise, defined by its centerline and inner and outer diameters, as well as its index of refraction. The absorber is not necessarily concentric to the glass envelope.

Camera parameters

The central-perspective model with radial and tangential lens distortion is used to describe the camera (Section 5.5.1). The central-perspective model is defined by its sensor size, s_x, s_y, focal length, f_c, principal point, x_0, y_0, and lens distortion coefficients K_1, K_2, K_3, P_1, P_2. The external orientation parameters describing the camera location relative to the collector vertex, $X_\mathrm{c}, Y_\mathrm{c}, Z_\mathrm{c}$, and Euler angle rotation, ω, ϕ, κ, are provided for each photograph.

Generating rays

All of the rays traced from the camera can be treated as though they emanate from the camera location. In image space, the camera location is represented by the perspective center of the camera. The direction of a ray in object space originating from the camera ($\vec{r}_\mathrm{c}$) that corresponds to image point (x, y) on a perspective-center camera is calculated with

$$\vec{r}_\mathrm{c} = -R^{-1} \begin{bmatrix} x \\ y \\ -f_\mathrm{c} \end{bmatrix}, \tag{7.2}$$

where R is the rotation matrix (Eqn. 5.25) calculated from the external orientation parameters of the camera.

Intersection with reflector surface

An intersection point of an incident ray with the quadratic surface $(X_\mathrm{t}, Y_\mathrm{t}, Z_\mathrm{t})$ is determined by parameterizing in the direction of the incident ray from the camera as given in

$$\begin{bmatrix} X_t \\ Y_t \\ Z_t \end{bmatrix} = \begin{bmatrix} X_c \\ Y_c \\ Z_c \end{bmatrix} + t\vec{r}_\mathrm{c}. \tag{7.3}$$

The parameter, t, is found by substituting $(X_\mathrm{t}, Y_\mathrm{t}, Z_\mathrm{t})$ in Eqn. 7.3 into (X, Y, Z) in Eqn. 7.1 and solving for t, which yields a quadratic function of t for which the solution is the well-known quadratic

equation:

$$t = \frac{1}{2A}\left(-B \pm \sqrt{B^2 - 4AC}\right) \tag{7.4}$$

with coefficients

$$\begin{aligned} A &= a{r_{\mathrm{c}_x}}^2 + b r_{\mathrm{c}_x} r_{\mathrm{c}_y} + c{r_{\mathrm{c}_y}}^2 \\ B &= 2aX_{\mathrm{c}} r_{\mathrm{c}_x} + b\left(X_{\mathrm{c}} r_{\mathrm{c}_y} + Y_{\mathrm{c}} r_{\mathrm{c}_x}\right) + 2cY_{\mathrm{c}} r_{\mathrm{c}_y} + d r_{\mathrm{c}_x} + g r_{\mathrm{c}_y} - r_{\mathrm{c}_z} \\ C &= a{X_{\mathrm{c}}}^2 + bX_{\mathrm{c}}Y_{\mathrm{c}} + c{Y_{\mathrm{c}}}^2 + dX_{\mathrm{c}} + gY_{\mathrm{c}} + h - Z_{\mathrm{c}}. \end{aligned} \tag{7.5}$$

The parameter, t, is then substituted back into Eqn. 7.3 to find the intersection point $(X_{\mathrm{t}}, Y_{\mathrm{t}}, Z_{\mathrm{t}})$. In order for the ray to intersect the parabolic collector, the intersection point must lie within the length and aperture constraints of the collector. Specifically, the following two conditions must be satisfied:

$$\begin{aligned} |X_t| &\leq \frac{w_{\mathrm{ap}}}{2} \\ |Y_t| &\leq \frac{l_{\mathrm{c}}}{2}. \end{aligned}$$

Reflection

In this model, if a ray intersects the reflector surface of the collector, it is specularly reflected. The incident ray, reflected ray, and surface normal are described by their unit vectors $\vec{r}_{\mathrm{c}}$, $\vec{r}_{\mathrm{r}}$, $\vec{n}$, respectively. The reflected ray is thus calculated using Snell's Law (Eqn. 7.6):

$$\vec{r}_{\mathrm{r}} = \vec{r}_{\mathrm{c}} - 2(\vec{n} \cdot \vec{r}_{\mathrm{c}})\vec{n}. \tag{7.6}$$

The ideal surface normal is found by taking the gradient of the quadratic surface (Eqn. 7.1) at the intersection point $(X_{\mathrm{t}}, Y_{\mathrm{t}}, Z_{\mathrm{t}})$. The gradient of the quadratic surface is given in Eqn. 7.7. The surface normal including reflector slope errors, θ_{r}, is given in Eqn. 7.8:

$$\nabla = \begin{bmatrix} (2aX + bY + d) & (bX + 2cY + g) & 1 \end{bmatrix} \tag{7.7}$$

$$\vec{n} = \begin{bmatrix} -\tan\left[\tan^{-1}\left(\nabla_x\right) - \theta_{\mathrm{r}}\right] & -\tan\left[\tan^{-1}\left(\nabla_y\right) - \theta_{\mathrm{r,long}}\right] & 1 \end{bmatrix}. \tag{7.8}$$

Intersection with Absorber

To determine whether a ray intersects the absorber, the receiver glass and receiver absorber are both modeled as perfect cylinders. An incident ray is traced through the receiver in multiple steps:

(1) Intersection with outer edge of the glass

(2) Refraction through the glass envelope

(3) Intersection with the inner edge of the glass

(4) Refraction into the annulus between the absorber and glass envelope

(5) Intersection with the absorber.

Intersection with a Cylinder

The equation of a cylinder with diameter, D_a, and center (X_a, Z_a) is given by

$$(X - X_a)^2 + (Z - Z_a)^2 = \frac{1}{4} D_\mathrm{a}^2. \tag{7.9}$$

To simplify the solution, two additional variables are defined:

$$\Delta X = X_a - X$$

$$\Delta Z = Z_a - Z.$$

Solving for the intersection point between a ray, $\vec{r}$, and cylinder yields a distance of

$$t = \frac{r_x \; r_z \; \Delta X + r_z^2 \; \Delta Z \pm r_z \; A}{r_z (r_x^2 + r_z^2)} \tag{7.10}$$

with

$$A = \sqrt{r_z^2 (\frac{1}{4} D_\mathrm{a}^2 - \Delta X^2) + r_x^2 (\frac{1}{4} D_\mathrm{a}^2 - \Delta Z^2) + 2 \; r_x \; r_z \; \Delta X \; \Delta Z}.$$

A solution of two distinct real roots for the distance (t) means that the ray intersects the cylinder twice. The shorter distance is the first intersection point and the value of interest. For a single

distinct real root, the ray is tangent to the cylinder. If the distance has a non-zero imaginary part, the ray does not intersect the cylinder. The ray $\vec{r}$ in Eqn. 7.10 represents the incident ray and can be a ray from the camera, a ray reflected from the collector, or a ray coming from either edge of the glass envelope.

Refraction

A ray passing through the glass envelope is refracted at both glass interfaces. The ratio of the index of refraction of the first medium to the index of refraction of the second medium is n_{12}. The incident ray, refracted ray, and surface normal are described by their unit vectors $\vec{r}_{\mathrm{i}}$, $\vec{r}_{\mathrm{t}}$, $\vec{n}$, respectively. The refracted ray is thus calculated using Eqn. 7.11:

$$\begin{aligned} \vec{z} &= n_{12}\left(\vec{r}_{\mathrm{i}} - (\vec{r}_{\mathrm{i}} \cdot \vec{n})\vec{n}\right) \\ \vec{r}_{\mathrm{t}} &= \vec{z} - \left(\sqrt{1 - |\vec{z}|^2}\right)\vec{n}. \end{aligned} \tag{7.11}$$

7.1.2 Camera Location

To reduce processing time, targets are not included in the generated images. The camera location is found independently of the generated images. The camera uncertainty includes errors in the placement of targets, errors in the target image centroids, and errors in the camera calibration parameters. The true target image locations for the perspective-center camera are determined with the collinearity equations (Eqn. 5.26) based on the true camera and target locations. The target image locations are converted to a real camera using the Newton-Raphson method to solve the lens distortion equations (Eqns. 5.22). Random errors are added to the target image locations of the real camera to represent image processing errors (centroiding errors for intentional targets). The target image locations are then converted back to the perspective-center camera with random errors included in the lens distortion coefficients.

Random errors are also applied to the distance and target coordinate constraints. Photogrammetry bundle adjustment, as described in Section 5.5.4, is then used to find the camera locations and target locations in object space. The calculated camera locations can be compared to

the true camera locations to determine the error in camera location due to the combined effects of target centroiding error, camera calibration error, constraint target placement error, and distance measurement error.

7.1.3 Image Analysis

The computer-generated images are analyzed in the same manner that real images are analyzed. The absorber location is found by projecting a uniform grid of points along the focal-line plane and locating the centerline of the absorber image in each photograph, as described in Section 6.4. The reflector-absorber angles are found by projecting by a uniform grid of points onto the reflector surface in each photograph and locating the reflection of the absorber, as described in Section 6.3. The reflector slope errors are then found by subtracting the effective slope errors (Eqn. 5.7) due to the absorber position from the reflector-absorber angles.

7.1.4 Application

The measurement uncertainty for a set of data acquired in the field or laboratory can be calculated directly by inputing the model parameters directly from the measurement data. To determine the uncertainty for a specific measurement, the measured r-a angles are used as the input for generating photographs. Likewise, the camera positions and number of photographs for the model are taken directly from the camera positions measured during the test. Using the measured data in the uncertainty model provides not only a more accurate measurement uncertainty, but also, gives the spatial variation of the measurement uncertainty across the collector due to the possible nonuniformity of the camera positions.

7.2 Model Convergence

If there is no uncertainty, the output absorber position and r-a angles should approach the input absorber position and r-a angles. Discrepancies between the inputs and outputs are a function of the resolution of the computer-generated photographs and errors inherent in the Observer method.

As the resolution of the photographs increases, the model should converge to a non-zero difference between inputs and outputs. The remaining discrepancy between input and output absorber position and r-a angles is the error inherent in the Observer method. This error includes refraction and longitudinal slope errors. Refraction is included during the image generation; however, the Observer measurement cannot measure the location of the receiver glass relative to the absorber and thus assumes there is no glass envelope. Likewise, longitudinal slope errors are included in the image generation; however, the Observer method cannot distinguish between a surface slope error in the longitudinal and transverse directions. The Observer measurement, therefore, includes errors in the r-a angles due to unknown longitudinal slope errors, as described in Section 5.2. To demonstrate the model convergence with zero uncertainty in the model parameters, a resolution refinement study was performed.

7.2.1 Resolution

There are two components of resolution in the Observer method: spatial and angular resolution. The spatial resolution is the spatial frequency along the collector or across the aperture in object space of image pixels. Due to the effect of parallax, the spatial resolution is not constant; however, it does not vary significantly across the collector aperture and can be well approximated with its average for typical measurement setups. The spatial resolution will be represented by its inverse, the linear distance between adjacent pixels in object space, which we will call the spatial resolution indicator. The average spatial resolution indicator for the absorber measurement is approximated with Δx_{abs}, which is the average distance in the transverse direction at the focal line between two adjacent pixels. The average spatial resolution indicator for the r-a angle measurement is approximated with Δx_{ap}, which is the average distance along the X-axis (Y=0, Z=0) between two adjacent pixels. The average spatial resolution indicators are calculated with

$$\Delta x_{\text{abs}} = \frac{s_y}{f_{\text{c}} N_y} \sqrt{X_{\text{c}}^2 + (Z_{\text{c}} - f)^2} \tag{7.12}$$

$$\Delta x_{\text{ap}} = \frac{s_y}{f_{\text{c}} N_y} \sqrt{X_{\text{c}}^2 + Z_{\text{c}}^2}, \tag{7.13}$$

where the collector is defined by its focal length, f. The camera is located at (X_c, Z_c). The camera sensor height is s_y, and there are N_y pixels across the sensor height. The camera lens focal length is f_c. The camera is oriented with the sensor height along the transverse axis of the collector and the sensor width along the longitudinal axis of the collector. If the camera is rotated 90°, the spatial resolution indicators should be calculated with respect to the sensor width instead of height. The average spatial resolution indicator along the Y-axis (Δy_{ap}) is also of importance to the r-a angle measurement; however, because typical camera sensors have nearly square pixels, we assume that $\Delta x_{ap} \approx \Delta y_{ap}$. Figure 7.1 shows the spatial resolution for the absorber position and r-a angle measurements.

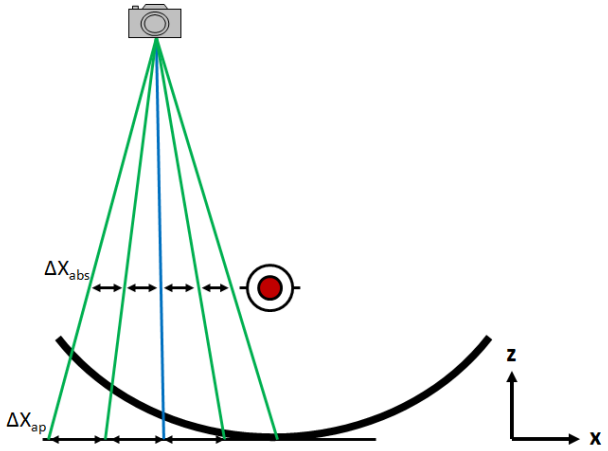

Figure 7.1: The concept of spatial resolution for the Observer method

The angular resolution only applies to the r-a angle measurement and is the angular frequency of photographs. The angular resolution varies from one point on the collector to another as well as between different photographs; however, these variations are small for typical measurement setups. The angular resolution will be represented with its inverse, the difference in camera angles between two consecutive photographs for a point on the collector, which we will call the angular resolution indicator. The angular resolution indicator is approximated by its average, $\Delta\Phi_c$, found with

$$\Delta\Phi_c = \frac{1}{M-1}\sum_{i=1}^{M-1}\left|\tan^{-1}\left(\frac{X_{c,i}}{Z_{c,i}}\right) - \tan^{-1}\left(\frac{X_{c,i+1}}{Z_{c,i+1}}\right)\right|, \tag{7.14}$$

where i denotes a particular photograph, and M is the number of photographs. For a fixed mea-

surement setup, the angular resolution is related to the number of photographs taken from one side of the aperture to the other. As the number of photographs increases, the resolution is refined. However, for different camera-collector distances, the number of photographs required to achieve a desired angular resolution varies. Figure 7.2 shows the concept of angular resolution with the angles approximated as $\Delta\Phi_c$. A camera located at a distance $Z_{c,1}$ requires more photographs than a camera located at a farther distance, $Z_{c,2}$, to achieve the same angular resolution.

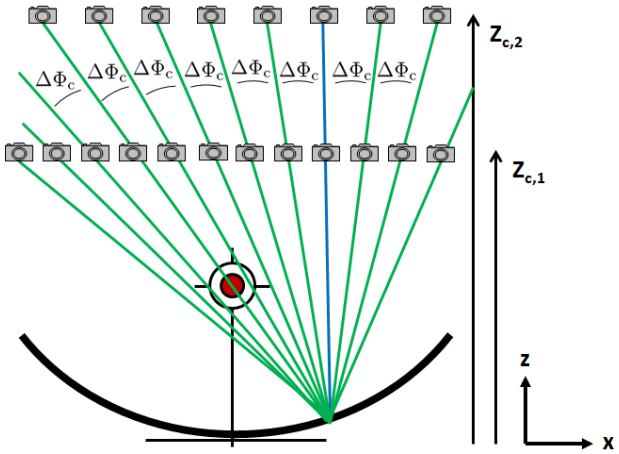

Figure 7.2: The concept of angular resolution for the Observer method

7.2.2 Absorber Alignment

To demonstrate convergence for the absorber alignment, the spatial resolution across the absorber was increased from about Δx_{ap}= 40 mm to 1 mm. This was equivalent to increasing the camera resolution from (178 × 268) pixels to (5696 × 8576) pixels for the Nikon D300 camera with 20-mm lens positioned at (X_c, Z_c) = (-7,7) m and (7,7) m. The collector geometry is an LS-2 with the absorber offset 3 mm toward the rim (X) and 5 mm toward the vertex (Z). The receiver glass is centered at the focal line so that the receiver absorber and glass are not concentric. Figure 7.3 shows the error in the calculated absorber position as a function of the image resolution. Comparing the error in X_a to Z_a, it is obvious that the absorber position in X is significantly more dependent on the spatial resolution than the absorber position in Z.

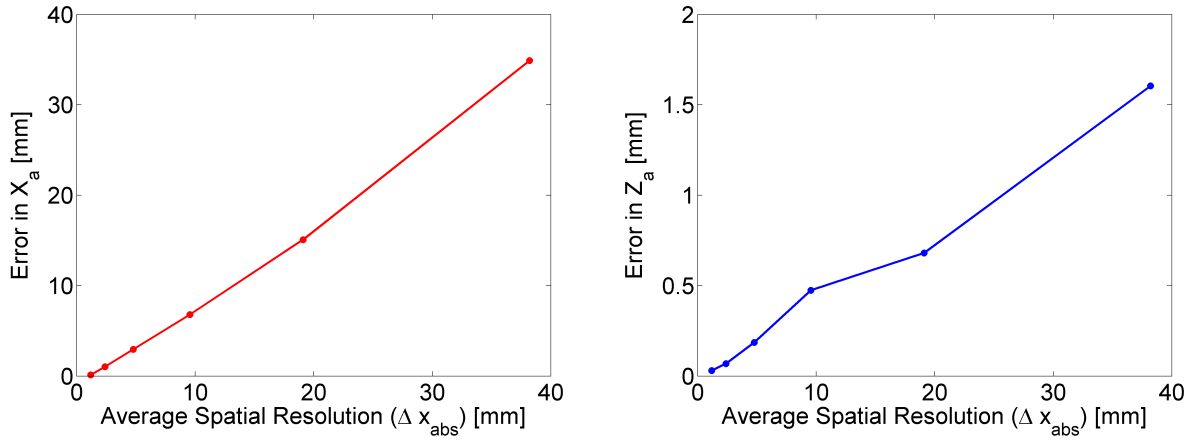

Figure 7.3: Convergence of the absorber position error for zero uncertainties

Instead of leveling out to a constant value, the error approaches zero. Therefore, we conclude that the error due to the effects of refraction is less than or equal to the error in the absorber measurement with the finest resolution. From Fig. 7.3, we see that the error in the absorber measurement due to refraction is less than 0.1 mm in each direction. Changing the receiver absorber and glass positions did not significantly change the results.

7.2.3 Reflector-Absorber Angles

As with the absorber position, increasing the angular and spatial resolutions for the r-a angles will reduce the difference between the input and output r-a angles to a constant error. For the r-a angles, this error is caused by both refraction and longitudinal slope errors. It was shown with the absorber model results that the refraction has a very small effect; therefore, the majority of the constant error in the r-a angles can be attributed to longitudinal slope errors. The ill effect of longitudinal slope errors can be minimized by increasing the distance between the camera and collector and positioning the camera near the center of the collector longitudinally, as described in Section 5.2. To demonstrate this effect, the sinusoidal pattern of longitudinal errors:

$$\theta_{\mathrm{r,long}} = 0.005 \sin \frac{Y}{10 w_{\mathrm{ap}}} \sin \frac{X}{10 w_{\mathrm{ap}}} \tag{7.15}$$

shown in Fig. 7.4 is used with a constant 0-mrad transverse slope error. The error in r-a angle measurement due to longitudinal slope errors is independent of the transverse slope errors.

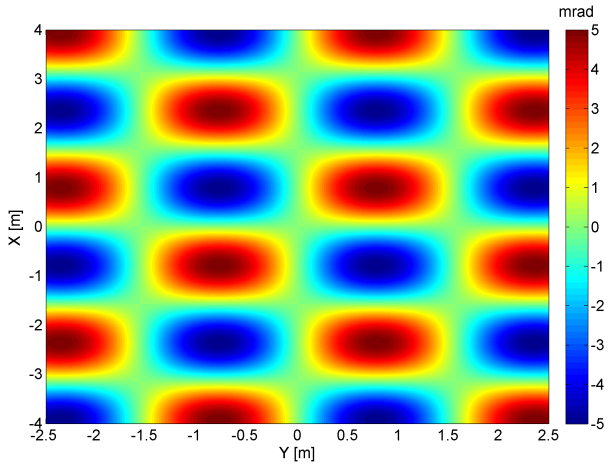

Figure 7.4: Input longitudinal slope errors

Figure 7.5 shows the error in output r-a angles caused by the longitudinal slope errors for camera distances of 20 m and 10 m. As expected, the errors in the r-a angles increase toward the ends of the collector because the longitudinal incidence angle (the angle of the incident ray from the camera along the longitudinal axis) increases away from the center of the collector. Likewise, the error in r-a angles increases as the camera moves closer to the collector because, once again, the longitudinal incidence angle increases.

To demonstrate model convergence for the r-a angles, the average spatial resolution was increased by increasing the number of pixels in the images, and the average angular resolution was increased by increasing the number of photographs. The camera distance is set to 15 m, and the model uncertainties are set to zero. The absorber is offset from the vertex by 3 mm in X and 5 mm in Z. A custom reflector transverse slope error map was created for this test using real, measured data from a single reflector panel and repeating it in different orientations, as shown in Fig. 7.6. This map represents high-frequency slope errors in the X- and Y-direction, the measurement of which especially depends on the spatial and angular resolution of the data. The longitudinal slope errors used are given in Fig. 7.4. The error in r-a angles is represented with the 0.95 error percentile,

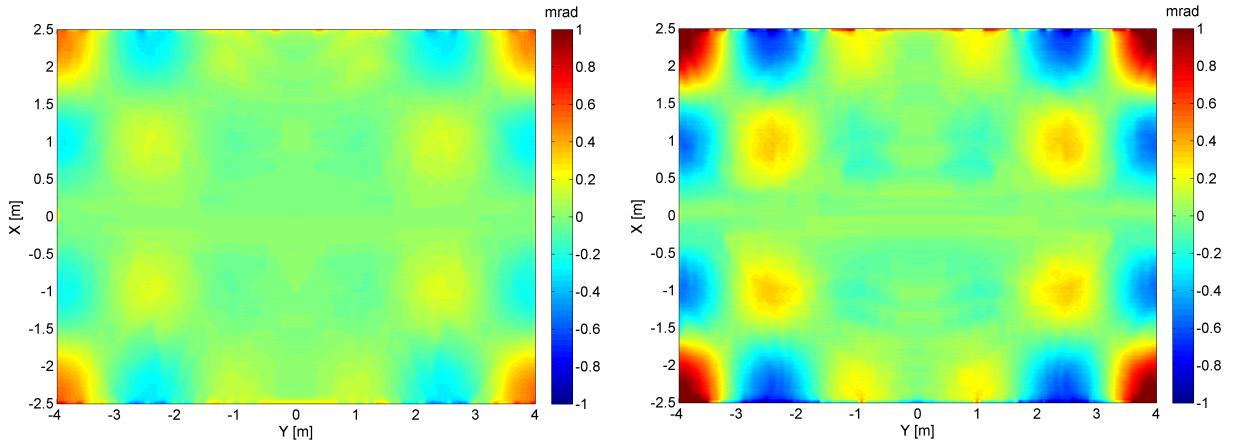

Figure 7.5: Error in the calculated r-a angles for zero uncertainties with longitudinal slope errors given in Fig. 7.4 for camera distances of 20 m (left) and 10 m (right)

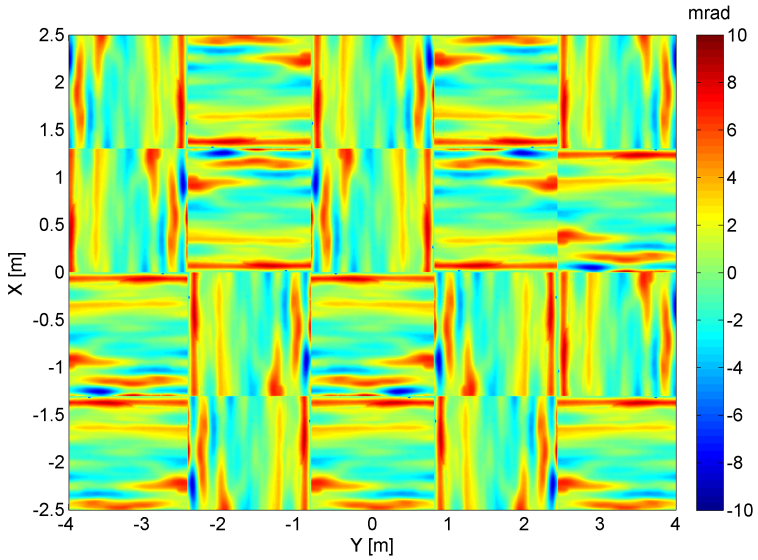

Figure 7.6: Input transverse slope errors

meaning that 95% of the differences between input and output r-a angles are below that value. This reduces the impact of large errors that may occur due to slope error discontinuities at reflector edges. Figures 7.7 and 7.8 show the error in r-a angles as a function of the spatial resolution indicator and angular resolution indicator, respectively. The error levels off to about 0.2 mrad, which is due to the longitudinal slope errors. For the case with zero longitudinal slope errors, the error in the calculated r-a angles approaches zero.

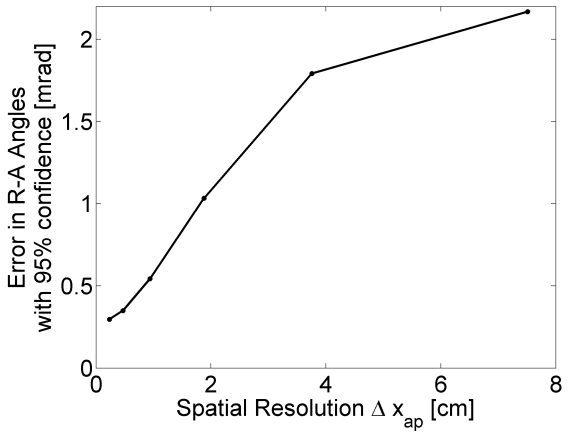

Figure 7.7: Convergence of the r-a angles error with constant angular resolution indicator of 0.8 mrad

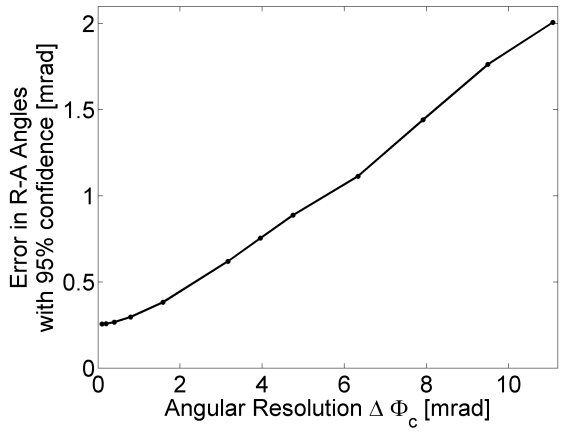

Figure 7.8: Convergence of the r-a angles error with constant spatial resolution indicator of 2.3 mm

7.2.4 Experimental Data

In addition to the model results, a set of real data was used to demonstrate the effect of angular resolution on the measurement of r-a angles. The data used here were taken with a stationary camera mounted on the ground imaging a rotating collector. The collector rotated smoothly so that the photographs are evenly spaced across the collector aperture. The data were first analyzed using the full 950 photographs as the baseline case. The data were then analyzed eight more times using only a fraction of the photographs for each analysis. Figure 7.9 shows an absorber-reflection plot created with 950 photographs compared to an absorber-reflection plot created with about 30 photographs.

As the number of photographs decreases, the angular resolution decreases and rapidly changing r-a angles across the aperture can no longer be resolved. For each resolution case, the maps of r-a angles was compared to the highest resolution case to determine the normalized error in the r-a angles due to decreased angular resolution. Figure 7.10 shows the normalized error for a 90% confidence as a function of the angular resolution (left) and number of photographs (right). A 90% confidence was used because the highest 10% of errors tend to be due to very large errors around the mirror edges, which will typically be discounted as noise in the measurement.

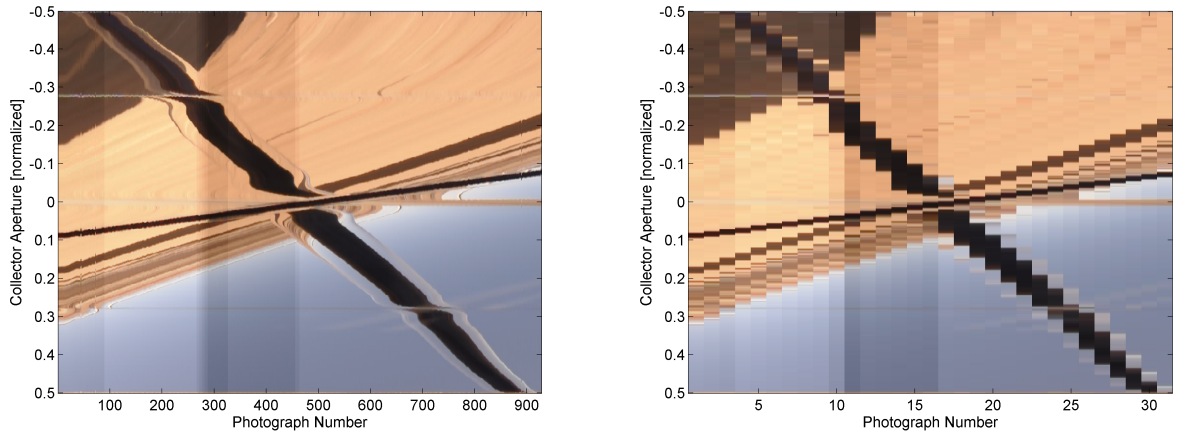

Figure 7.9: Absorber-reflection plots with high angular resolution ($\Delta\Phi_c \approx 0.5$ mrad) on the left and low resolution ($\Delta\Phi_c \approx 16$ mrad) on the right

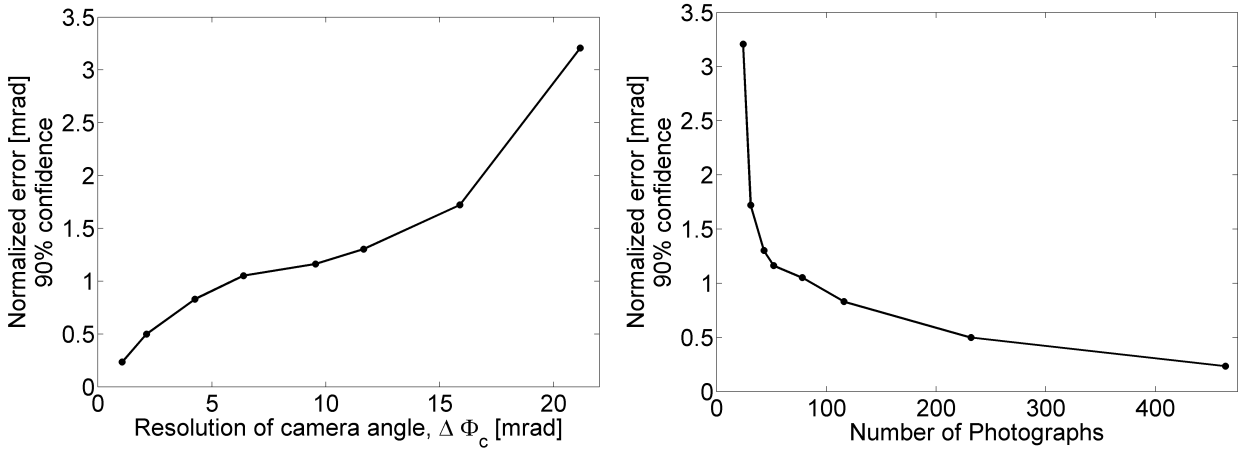

Figure 7.10: Normalized error in the r-a angles for a 90% confidence as a function of angular resolution indicator (left) and number of photographs (right)

To accurately perform a similar study with the spatial resolution, multiple sets of data should be taken with the camera set to different resolutions. The targets must be re-sized specifically for each camera resolution. Due to the rather limited camera resolution settings, this study was not performed. Instead, to demonstrate the concept of spatial resolution with real data, the data set from the angular resolution study was used again. The camera locations were found using the full-resolution images. The images were then uniformly sampled to decrease their resolution. The reduced photographs were analyzed using the original camera locations. From an original

resolution of 1280 × 720, the resolution was reduced to 640 × 360, 320 × 180, 160 × 90, and 80 × 45. Figure 7.11 shows absorber-reflection plots with full and reduced resolution.

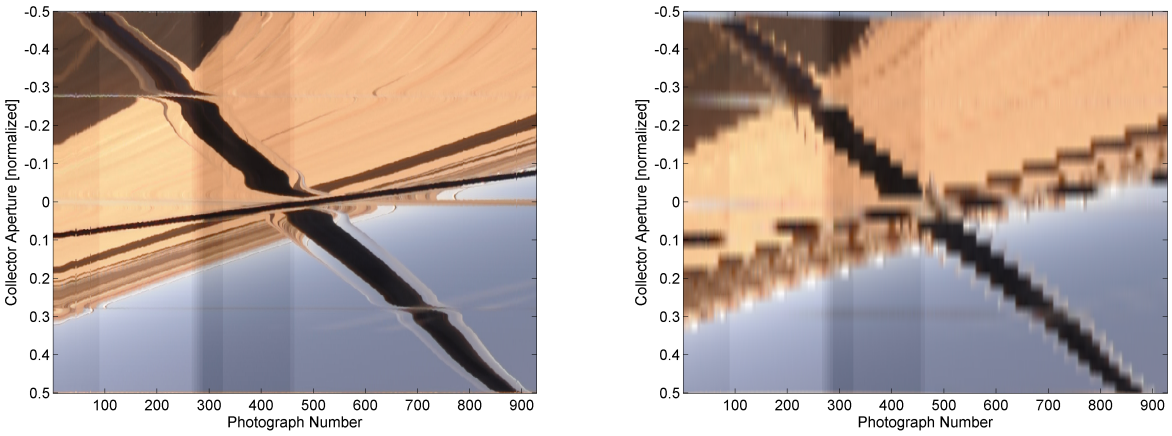

Figure 7.11: Absorber-reflection plots with high spatial resolution ($\Delta x_{\text{ap}} \approx 1$ cm) on the left and low spatial resolution ($\Delta x_{\text{ap}} \approx 15$ cm) on the right

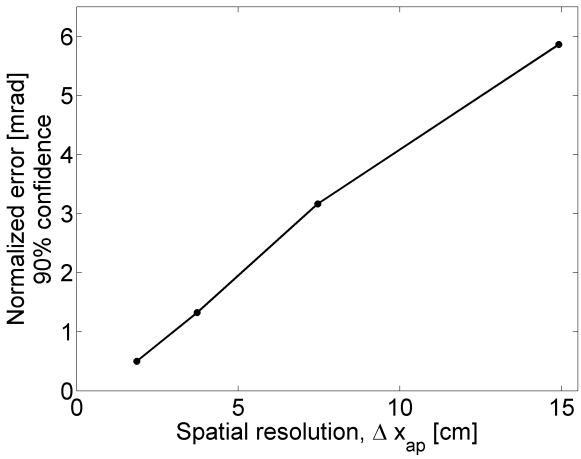

Figure 7.12: Normalized error in the r-a angles for a 90% confidence as a function of the spatial resolution indicator

7.3 Model Parameters

To determine the uncertainty in the Observer measurement, non-zero error sources must be included in the Monte Carlo uncertainty model. The error sources included in the uncertainty model include the following:

- Target coordinate constraints
- Distance constraints
- Camera focal length
- Camera principal point
- Camera lens distortion coefficients
- Target image locations
- Absorber image centerline
- Absorber-reflection image centerline.

Normal distributions of random error with average values $\mu = 0$, and standard deviations, σ, are specified for each uncertainty source.

Target coordinate constraint uncertainty accounts for discrepancies between the physical target locations and the target coordinate constraint values. Target coordinate constraints are typically based on the collector design. Errors between the collector design shape and the actual collector shape are accounted for in the target coordinate constraint errors. Additionally, differences between the assumed placement of the targets and the actual placement are included in this error term. The target coordinate constraint uncertainty is highly dependent on the specific collector being measured. Reflector position tolerances vary between manufacturers and even collectors. Therefore, a range of target coordinate uncertainties are used in the model from $\sigma = 1$ mm to $\sigma = 10$ mm.

The distance constraint uncertainty accounts for discrepancies between the physical distance between two targets and the measured distance. If the distance constraint values are measured with a laser distance meter or measuring tape, the distance constraint error should reflect the error in that measurement device. State-of-the-art laser distance meters claim uncertainties of ± 1.5 mm, with additional errors arising from the placement of the laser distance meter with respect to the target center. The distance constraint uncertainty is, therefore, approximated with $\sigma = 3$ mm.

Uncertainty in the camera calibration includes errors in the lens focal length, principal point, and lens distortion coefficients. The camera calibration uncertainty includes errors in the cali-

bration procedure, differences between the lens distortion model and the actual performance of the camera, as well as changes in the lens between taking the calibration photographs and taking the measurement photographs. Camera calibration uncertainty was estimated using the Caltech MATLAB calibration toolbox. The uncertainty for the Nikon D300 with 20 mm focal-length lens is estimated as $\sigma = 3 \times 10^{-3}$ mm in the focal length, $\sigma = 5 \times 10^{-3}$ mm in the principal point, and $\sigma = 1 \times 10^{-6}, 1 \times 10^{-8}, 2 \times 10^{-6}, 3 \times 10^{-6}$ mm in K_1, K_2, P_1, and P_2, respectively. For this camera, as is often the case, only two radial distortion coefficients were needed.

Target image location uncertainty is due to errors in the image centroiding algorithm for intentional targets, as well as distortion of the target image. For appropriately sized intentional circular targets and even lighting across the whole target image (no partial shadowing of the image), the target image location uncertainty is estimated to be $\sigma = 0.1$ pixels [7].

Uncertainty in the centerline of the absorber image and the absorber image reflection account for errors in the image processing algorithms used to find those centerlines. False edges found with the contour algorithms that are not correctly filtered can result in errors in the centerline location. Additionally, uneven lighting on the absorber or absorber reflection can result in errors in the centerline location. Uncertainty in the absorber and absorber-reflection image centerlines is estimated at $\sigma = 1$ pixel based on the author's experience with the implemented algorithms.

There are several additional possible uncertainty sources that were not included in this model. Positional errors in the reflector surface are treated exclusively as reflector slope errors. If the reflector surface shape is largely unknown, deviations between the reflector position and its assumed position may cause errors in the r-a angle measurements. If the absorber alignment is measured, a surface fit can be applied to the reflector slope errors to minimize position errors; however, no corrections can be made to the r-a angles if the absorber alignment is not measured. The bending of rays due to changes in atmospheric refraction is also ignored. High temperatures near the receiver and the ground in the desert affect the index of refraction, causing light rays to bend, which could introduce errors in the r-a angle and absorber measurements. Finally, the absorber is assumed to be stationary. In the field, fluid movement in the absorbers may cause vibrations, changing the

absorber position over time.

7.4 Absorber Position Uncertainty

The image generation and analysis uncertainty model developed for the Observer method was used to evaluate the uncertainty in the absorber alignment measurement. The camera used for the uncertainty analysis is a Nikon D300 that takes high-resolution photographs at 4288 × 2848 pixels. The collector geometry is an LS-2. The absorber is offset 3 mm toward the rim (X) and 5 mm toward the vertex (Z). The receiver glass envelope is centered at the focal point. Targets are located at the four corners of the collector, with additional targets added along the rims. A total of twelve targets are used unless otherwise specified. Two photographs are taken at positions (X_c, Z_c) = (-7,7) m and (7,7) m aligned at the center of the collector along its length (Y_c=0). With a convergence criterion of 10^{-5} m, the uncertainty with a 95% confidence converged around 500 model runs.

The spatial resolution for the absorber alignment measurement is indicated with Δx_{abs} as given in Eqn. 7.12, which is the linear distance between adjacent pixels along the focal-line plane of the collector. As the spatial resolution increases the distance between pixels, (Δx_{abs}) decreases, reducing the uncertainty in the absorber alignment measurement because there are more pixels across the absorber image. Figure 7.13 shows the uncertainty in absorber alignment measurement as a function of the spatial resolution indicator. The spatial resolution was varied by changing the number of pixels across the image sensor with all other variables held constant. From Fig. 7.13, we recommend a minimum value of about $\Delta x_{abs} = 2$ mm for the absorber alignment measurement.

To understand the dependence of absorber position measurement on target placement accuracy, the target location uncertainty was varied from $\sigma = 0$ mm to $\sigma = 10$ mm while the other uncertainty values were held constant. The uncertainty in the absorber measurement for a 95% confidence is shown in Fig. 7.14. For this setup, to measure the absorber position within ±5 mm, uncertainty in the target constraints should be less than $\sigma = 8$ mm.

To determine the effect that number of targets has on the absorber position uncertainty, the

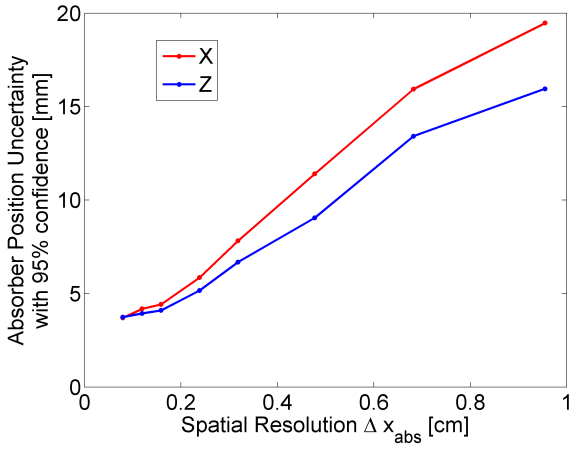

Figure 7.13: Uncertainty in the absorber alignment with changing camera resolution

target location uncertainty was set to $\sigma = 5$ mm, and the number of targets was varied between 6 and 20, with the additional targets spaced evenly along the rims. Figure 7.15 shows the uncertainty in the absorber measurement for a 95% confidence. As expected, the absorber position uncertainty decreases as the number of targets increases. This decrease in uncertainty is attained at the cost of a longer setup time required to place additional targets.

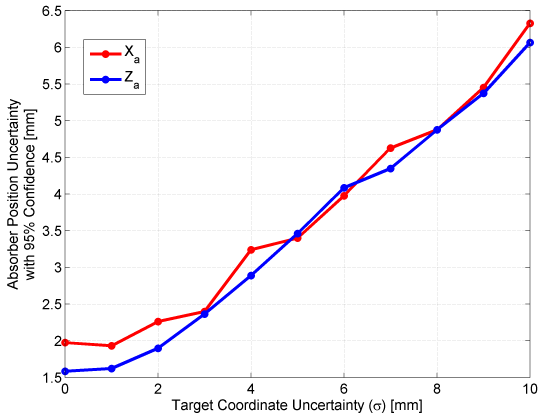

Figure 7.14: Absorber position uncertainty with 95% confidence as a function of target constraint uncertainty σ

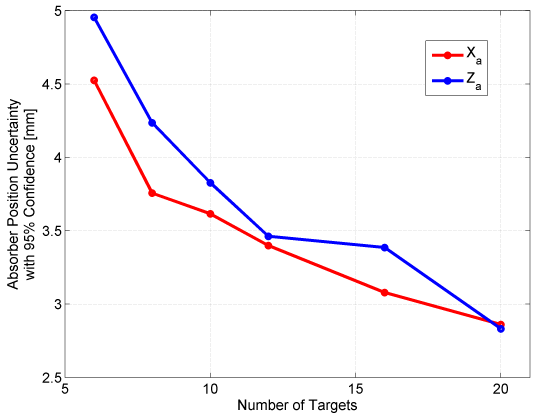

Figure 7.15: Absorber position uncertainty with 95% confidence as a function of number of photogrammetry targets

7.5 Reflector-Absorber Angle Uncertainty

To investigate the uncertainty in the r-a angle measurement, the same LS-2 parabolic trough collector with the absorber positioned at $(X_\mathrm{a}, Z_\mathrm{a})$=(3,-5) mm was used with the transverse and longitudinal slope errors given in Figs. 7.4 and 7.6. The uncertainty values given in Section 7.3 are used for the model parameters with the target coordinate constraint uncertainty set to $\sigma = 5$ mm unless otherwise stated. The Prosillica GE1910C camera with resolution 1920 $\times$ 1080, which has successfully been used with a R-C helicopter platform to measure r-a angles, was used unless otherwise stated. As with the absorber alignment measurement, the uncertainty in the r-a angles decreases as the number of targets is increased or the accuracy of the target coordinate constraints is increased. Unlike the absorber alignment, the uncertainty in the r-a angles measurement depends on several additional test parameters.

The uncertainty in the r-a angle measurement depends mainly on three test parameters: the spatial resolution, angular resolution and camera-target angle. The angular and spatial resolutions are both defined in Section 7.2. The camera-target angle (θ_ct) is the angle between the camera and the two widest targets in the transverse direction. If targets are only placed along the rims of the collector, the camera-target angle can be calculated with

$$\theta_\mathrm{ct} = 2\tan^{-1}\left(\frac{w_\mathrm{ap}}{2(Z_\mathrm{c} - (w_\mathrm{a}/2)^2/(4f)}\right), \tag{7.16}$$

where w_ap is the aperture width, and Z_c is the camera height. Figure 7.16 illustrates the camera-target angle. The target spacing is the distance between targets 1 and 4 or 2 and 3.

As the camera-target angle increases, the camera positions can be measured more accurately, reducing the r-a angle measurement uncertainty. Figure 7.17 shows the uncertainty in the r-a angles with a constant angular resolution indicator of $\Delta\Phi_\mathrm{c} = 6.1$ mrad and a constant spatial resolution indicator of $\Delta x_\mathrm{ap} = 8.4$ mm. The camera-target angle is varied from 5°–40° by changing the target placement. Instead of positioning targets on the collector, the targets are positioned on the ground to achieve the specified camera-target angle. For real measurements, targets should be placed on the ground and on the collector with target coordinate constraints only written for those targets

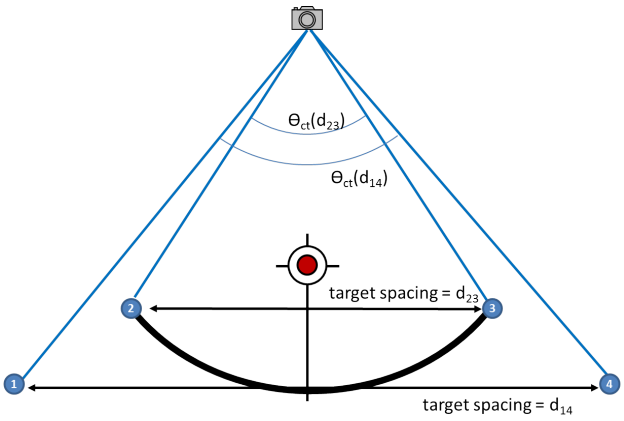

Figure 7.16: Illustration of the camera-target angle for targets placed on the rims of the collector and on the ground

on the collector. It can be seen in Fig. 7.17 that to achieve maximum accuracy the camera-target angle should be at least 20°. Camera target angles lower than 10° should not be used due to the resulting high uncertainty in the r-a angles.

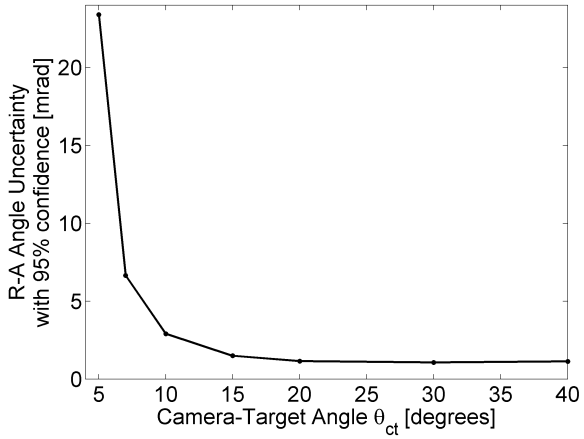

Figure 7.17: Uncertainty in the r-a angles with constant angular and spatial resolutions using six targets

The angular resolution is represented with $\Delta\Phi_c$ given in Eqn. 7.14, which is the average angular difference between consecutive photographs relative to the vertex of the collector. As the angular resolution increases, by taking photographs closer together, the test parameter, $\Delta\Phi_c$, decreases, which reduces the uncertainty in the r-a angle measurement. Figure 7.18 shows the

uncertainty in r-a angles for a constant spatial resolution indicator of $\Delta x_{\text{ap}} = 8.4$ mm and a constant camera-target angle of 15°. Examining Fig. 7.18, we see that $\Delta\Phi_{\text{c}} \leq 6$ mrad is desireable for minimum measurement uncertainty.

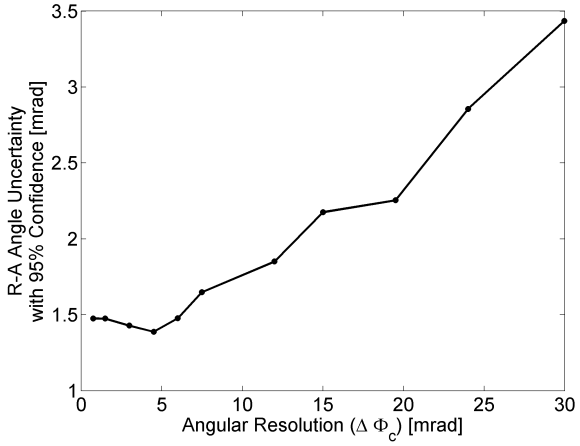

Figure 7.18: Uncertainty in the r-a angles with a constant spatial resolution and camera-target angle using six targets

The spatial resolution is represented with Δx_{ap} given in Eqn. 7.13, which is the linear distance between adjacent pixel intersections with the X-Y plane at the vertex of the collector. Increasing the spatial resolution decreases the test parameter Δx_{ap} so that the collector image comprises more pixels, reducing the r-a angle measurement uncertainty. Figure 7.19 shows the uncertainty in r-a angles with a constant angular resolution indicator of $\Delta\Phi_{\text{c}}$= 6.1 mrad and a constant camera-target angle of $\theta_{\text{ct}} = 15°$. From this figure, we can see that the uncertainty begins to level off at its minimum value around $\Delta x_{\text{ap}} = 2.5$ cm. The measurement uncertainty in the r-a angles for the recommended test parameter values of $\Delta x_{\text{ap}} = 2.5$ cm, $\Delta\Phi_{\text{c}} = 6$ mrad, and $\theta_{\text{ct}} = 20°$ is ±1 mrad with a 95% confidence using 12 targets.

It is clear that to reduce measurement uncertainty in the r-a angles, the spatial resolution, angular resolution, and camera-target angle should all be increased; unfortunately, these three test parameters are each correlated to multiple test variables. The test variables that are controllable by the operator include camera height, camera resolution, number of photographs, and target spacing.

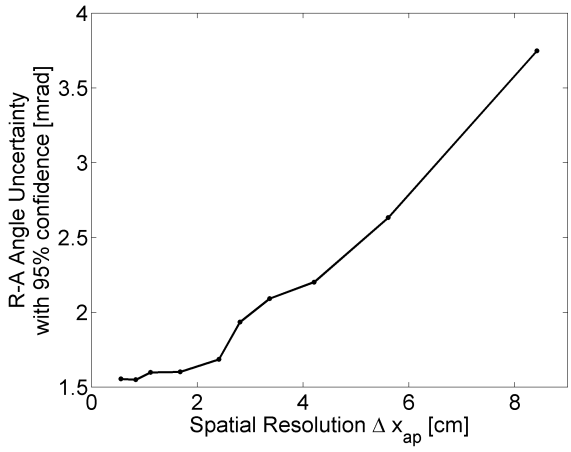

Figure 7.19: Uncertainty in the r-a angles with a constant angular resolution and camera-target angle using six targets

Table 7.1 shows the correlations between the angular resolution, spatial resolution, camera-target angle and the aforementioned test variables. To minimize the uncertainty in the r-a angles, the camera resolution, number of photographs, and target spacing should all be maximized; however, it is unclear how the camera height will affect the uncertainty.

Table 7.1: Correlations between test parameters and test variables

	Angular Resolution	Spatial Resolution	Camera-Target Angle
Camera Height	Direct	Indirect	Indirect
Camera Resolution	-	Direct	-
Number of Photos	Direct	-	-
Target Spacing	-	-	Direct

7.5.1 Camera Height

The camera height affects the spatial resolution, angular resolution, and the camera-target angle. Recall also that the longitudinal incidence angle of the camera is indirectly correlated to the camera height so that as the camera height increases, the error due to longitudinal slope errors decreases. To explore the effect of camera height, the camera height was varied from 15 to 35 m above the collector with all other test variables held constant. At a height of 15 m, the collector

almost completely fills the camera's field of view, so that 15 m is the minimum camera height for this test setup. A total of 50 photographs were generated. Four, six, and twelve targets were used with four on the collector corners and the remainder evenly spaced along the collector rims. Table 7.2 lists the camera heights modeled, along with their associated test parameters.

Table 7.2: Observer test parameters for sample camera heights

Camera Height Z_c [m]	Spatial Resolution ΔX_{ap} [mm]	Angular Resolution $\Delta\Phi_c$ [mrad]	Camera-Target Angle θ_{ct}	Longitudinal Incidence Angle Φ_{long}
15	6.3	8.1	20.3°	16.0°
20	8.4	6.1	15.0°	11.9°
25	10.5	4.9	11.9°	9.5°
30	12.6	4.1	9.9°	7.9°
35	14.7	3.5	8.4°	6.7°

Figure 7.20 shows the effect of camera height on the r-a angle measurement uncertainty. As the camera height increases, the uncertainty does not vary significantly between 15 m and 22.5 m; afterwhich, the uncertainty increases as the camera height increases. From this plot, we conclude that for low camera heights, the effects of increasing angular resolution and the reduction in longitudinal incidence angle balance out the effects of decreasing spatial resolution and decreasing camera-target angle; however, for high camera heights, the effect of decreasing spatial resolution and decreasing camera-target angle dominate the uncertainty. In general, the camera height should be minimized to reduce the measurement uncertainty in the r-a angles; however, for each test scenario, there is a range of camera heights for which the uncertainty does not significantly change. This range, as well as the ideal camera height that minimizes the uncertainty, can be found using the uncertainty model for specific test scenarios.

To determine whether the effect of angular resolution or camera-target angle dominates the r-a angle uncertainty as the camera height changes, the camera-target angle was held constant as the camera height was changed from 15 to 35 m. To maintain a constant camera-target angle, the layout of the targets was changed for each camera height. Six targets remained on the collector with four on the corners and two centered on the rims. Six more targets were positioned on

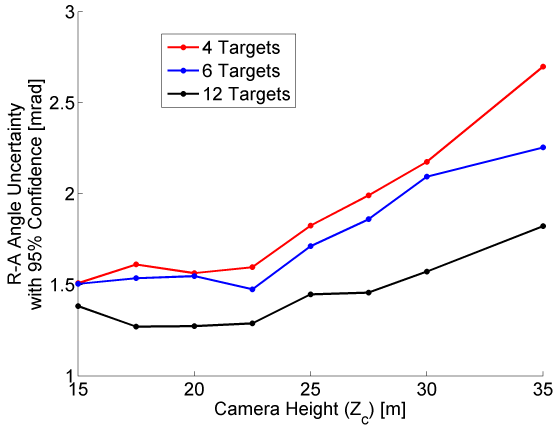

Figure 7.20: Uncertainty in the r-a angles for the GE1910C camera with 50 photographs and the specified number of targets placed on the collector

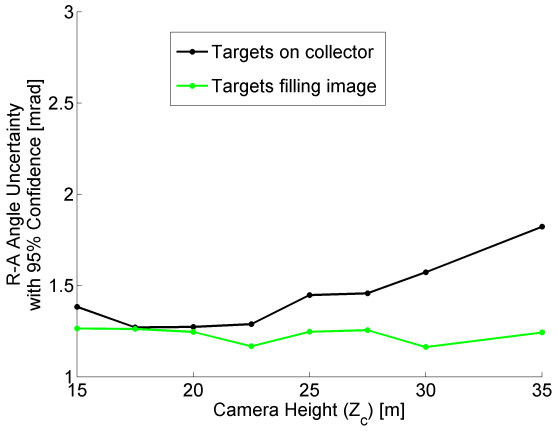

Figure 7.21: Uncertainty in the r-a angles for a constant camera-target angle of 20.3° where the targets are placed to fill the image compared to a changing camera-target angle where the targets are only placed on the collector

the ground around the collector so that the camera-target angle remained at $\theta_{ct} = 20.3°$ for all camera heights. Target coordinate constraints were only written for the targets on the collector. The uncertainty in r-a angles for the constant camera-target angle was compared to the case with twelve targets all located on the collector where the camera-target angle changes with the camera height. The comparison is shown in Fig. 7.21. The uncertainty for the constant camera-target angle is approximately constant between camera heights of 15 m and 35 m. From these results, we can conclude that the dominant factor in the increase in r-a angle uncertainty with increasing camera height for this measurement setup is the decreasing camera-target angle caused by only placing targets on the collector. The effects of spatial resolution, angular resolution, and longitudinal incidence angle due to changing camera height for this test scenario balance each other out. The result is that the camera height can be changed across a wide range of heights without affecting the r-a angle uncertainty as long as the targets are placed to maintain the same camera-target angle at each camera height.

7.5.2 Summary

To minimize the uncertainty in the reflector-absorber angles measurement, a large number of targets should be used with the widest targets filling as much of the image as possible. A wide-angle lens and large-format image sensor should be used to increase the camera's field of view, thus increasing the maximum allowed target spacing. The camera resolution and number of photographs should both be maximized to increase the spatial and angular resolution of the data. The camera can be placed across a range of heights above the collector without significantly affecting the uncertainty as long as the targets are placed to fill as much of the image as possible. However, to decrease the r-a angle uncertainty, it is more practical to place the camera at a lower height and increase the number of photographs than to position the camera at a higher position and increase the camera resolution because the operator typically has more control over the number of photographs than the resolution of the camera. The recommended values for spatial resolution, angular resolution, and camera target angle are $\Delta x_{\mathrm{ap}} = 2.5$ cm, $\Delta\Phi_{\mathrm{c}} = 6$ mrad, and $\theta_{\mathrm{ct}} = 20°$, respectively. The uncertainty in the reflector-absorber angles for the recommended test parameters and 12 targets is ± 1 mrad with a 95% confidence. However, if these test parameters are not met, the measurement uncertainty can be calculated using the uncertainty model for each specific measurement setup.

Chapter 8

Results

8.1 Validation

The Observer measurement of reflector surface slope errors and absorber position location were validated independently. The reflector surface slope errors were compared to measurements from two well-known laboratory optical characterization tools. Absorber position measurements were compared to traditional photogrammetry.

8.1.1 Reflector Surface Slope Measurement

A tremendous effort was put forth to validate the Observer method for measuring reflector slope errors. Typically, reflector surface slope tools are validated by measuring a highly accurate flat reflector panel. This method is not applicable to the Observer technique because it relies on a curved reflector with a focal point at which an absorber can be located to create a reflection. In the absence of a highly accurate parabolic reflector, the Observer technique was compared to other surface characterization tools for parabolic trough reflectors. Currently, the majority of reflector surface slope characterization tools are based in Europe. There are no reliable field surface characterization tools in the United States, so the validation was performed in the laboratory with a single reflector panel. The two main laboratory tools available in the United States for surface characterization of parabolic trough reflectors are VSHOT and SOFAST. Both VSHOT and SOFAST were designed for point-focus reflectors and were adapted to test line-focus reflectors after the fact. VSHOT is a much older tool, and due to the extensive setup and testing time it is becoming obsolete; however,

SOFAST was not accessible until quite recently, so the Observer method was compared both to VSHOT and SOFAST. The VSHOT comparison was performed first, before we obtained access to SOFAST.

VSHOT Comparison

VSHOT is a scanning-laser optical measurement tool that was developed jointly by NREL and Sandia around 1997 and has been used almost exclusively at NREL since [38]. VSHOT measures reflector surface slope based on the known incident angle of a laser beam and the measured return spot location of the reflected ray on a target. A quadratic surface is fit to the measured slope data to find the reflector slope errors relative to a best-fit surface. The best-fit surface is anchored in space based on a distance measurement from the target to the reflector panel. VSHOT requires almost a full day for setup and testing of a single reflector panel. The reflector panel must be located at a distance of about twice the reflector focal length from the target. Unfortunately, this tight spacing required that the reflector panel be moved between the VSHOT measurement and the Observer measurement.

A reflector panel was mounted on a large aluminum frame to be measured with both VSHOT and the Observer. The panel was an inner panel from an LS-2 geometry collector with 1.57-m length, 1.39-m aperture, and a design focal length of $f = 1.49$ m. A green, PVC tube with outer diameter $D_{\mathrm{a}} = 8.73$ cm was used as a mock absorber. The tube was mounted horizontally near the focal line of the reflector, and its position was measured using photogrammetry by placing targets on and around the absorber. A Nikon D90 camera was mounted on a hand-operated lift. The camera was raised vertically across the aperture of the reflector while taking a movie of the absorber reflection. Care was taken to make sure the movement of the camera was extremely slow and steady to minimize the effects of the rolling shutter. To confirm that the rolling shutter was not contributing to measurement error, the reflector was measured by moving the camera in opposite directions. The results agreed without a significant bias error. Figure 8.1 shows the reflector panel setup for the comparison test between VSHOT and the Observer. Four targets near the corners of

the reflector panel were used to find the camera location.

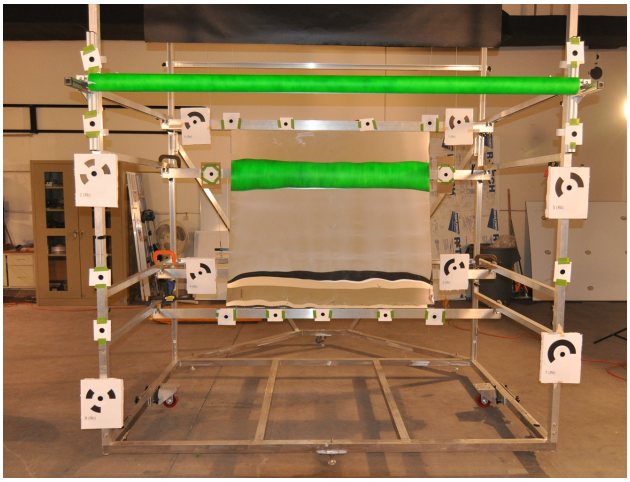

Figure 8.1: Laboratory setup for the Observer comparison with VSHOT

VSHOT measures both the longitudinal and transverse reflector slope errors and then fits a Zernike polynomial to the measured slopes. The order of the Zernike polynomial can be designated by the user. The slope errors are calculated from the difference between the measured slopes and the gradients of the best-fit polynomial. For the comparison with the Observer, a second-order Zernike polynomial was used. The reflector panel was aligned relative to VSHOT to minimize all of the coefficients except the second-order X-coefficient, which contains the focal length in the transverse direction. This process was intended to minimize the effects of longitudinal slope errors on the best-fit polynomial, and thus, on the transverse slope errors relative to that polynomial. A similar surface fit was applied to the Observer results, as described in Section 6.5 and Appendix B.1. The transverse reflector slope errors measured with VSHOT and the Observer are shown in Fig. 8.2. The root-mean-square (RMS) of the difference between the two measurement tools is 1.6 mrad. The uncertainty in the Observer measurement calculated with the uncertainty model for a 95% confidence is 2.9 mrad. For the uncertainty calculation, the uncertainty sources were set as specified in Section 7.3, with the target coordinate constraint uncertainties set to $\sigma = 3$ mm.

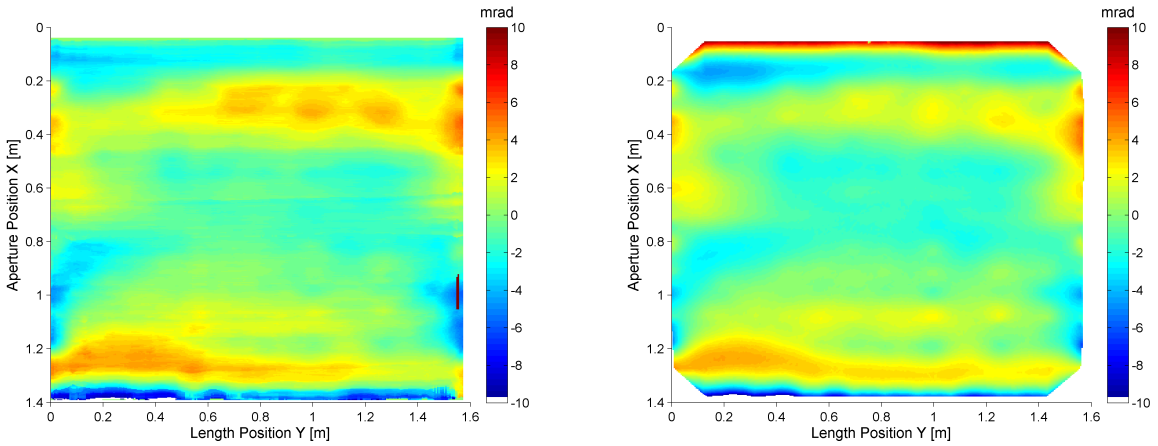

Figure 8.2: Reflector slope errors measured with the Observer (left) and VSHOT (right) of an LS-2 geometry inner reflector panel in the laboratory

SOFAST Comparison

SOFAST is a fringe reflection tool developed at Sandia National Laboratories originally for the surface characterization of parabolic dish reflector facets [1]. SOFAST was adapted to test parabolic trough reflector panels and was licensed to NREL for this purpose. There are currently no publications describing the adaptations made for line-focusing collectors, and the uncertainty is largely unknown. The SOFAST system in use at NREL consists of a 10 ft $\times$ 10 ft projector screen onto which a series of sinusoidal fringe patterns are projected. A single parabolic trough reflector facet is oriented in space so that a camera mounted next to the projector screen can image the reflection of the fringes in the panel. Like VSHOT, SOFAST measures the reflector surface profile independently in both the transverse and longitudinal directions, and a second-order polynomial is fit to the surface. Unlike VSHOT, the best-fit polynomial is independent of the orientation of the reflector panel. The orientation of the polynomial is determined by translating and rotating the measured slopes in space to minimize the slope errors at a designated anchor point on the panel; the polynomial in VSHOT is only translated, not rotated. Instead of depending on the orientation of the panel, the best-fit polynomial is highly dependent on the system inputs including the locations of the reflector panel corners, design focal length, and reference distance from the projector screen

to the anchor point. However, the surface slope errors remain relatively unchanged regardless of the system inputs. For this measurement scenario with a largely unknown single reflector facet, the best-fit polynomial essentially absorbs any errors in the system inputs.

The Observer results were also fit to a second-order polynomial. The best-fit polynomial for the Observer measurement likewise absorbs any errors in the system inputs, specifically the target coordinate constraints and absorber position. The reflector slope errors remain unchanged across a wide range of system inputs. Trusting that the best-fit polynomials absorb any system input errors, the reflector slope errors from SOFAST and the Observer should show good agreement. Small discrepancies between the measurements are to be expected because SOFAST measures both the transverse and longitudinal errors, and its best-fit polynomial reflects both of those; the Observer only measures and fits to the transverse errors.

A single inner panel from an LS-3 geometry collector was used with 1.7-m length, 1.62-m aperture, and $f = 1.71$-m design focal length; however, the method in which the panel was mounted significantly distorted the reflector panel, leaving the focal length largely unknown. The reflector panel was mounted with its transverse axis parallel to the ground and then tilted slightly up toward the SOFAST camera to accommodate the SOFAST measurement. The same mock absorber as in the VSHOT comparison was used here except that this time it was mounted vertically because the reflector panel was rotated 90°. Once again, the absorber position was measured with photogrammetry. For the Observer, a Nikon D300 camera was mounted on a wheeled tripod and scanned horizontally across the aperture of the reflector panel while taking still images. Unfortunately, due to the setup constraints, a 20-cm section along the bottom of the reflector could not be measured with the Observer. Figure 8.3 shows the laboratory setup with the mock absorber and photogrammetry targets. The four targets on the corners of the reflector panel were used to find the camera location.

The reflector panel was not moved between the Observer and SOFAST tests; however, the photogrammetry targets and absorber were removed before performing the SOFAST test. Figure 8.4 shows the reflector surface slope error maps measured by SOFAST and the Observer, respectively.

The RMS of the difference between SOFAST and the Observer is 2.1 mrad. These discrepancies can best be attributed to uncertainties in both tools, as well as the fact the SOFAST best-fit polynomial also reflects measurement of the longitudinal errors. The uncertainty in the Observer measurement for a 95% confidence is 3.7 mrad with the same model parameter uncertainty values as in the VSHOT comparison.

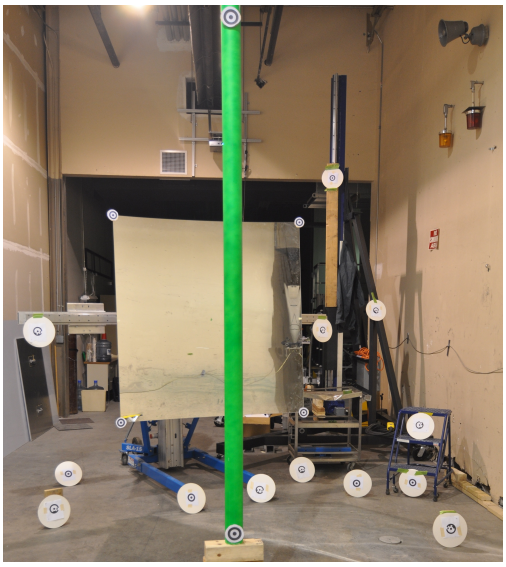

Figure 8.3: Laboratory setup for the Observer comparison with SOFAST

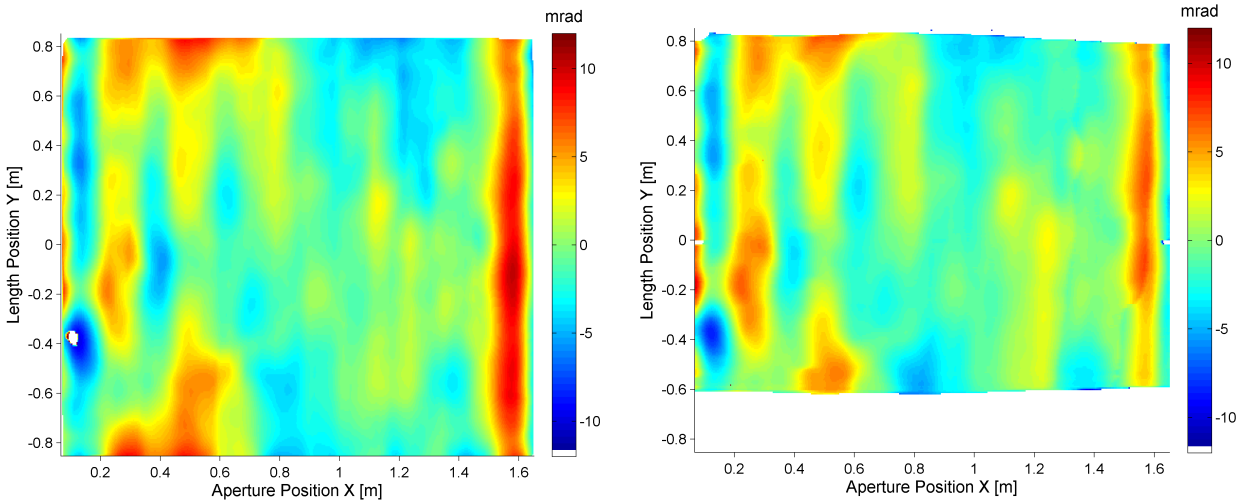

Figure 8.4: The reflector slope error results measured with SOFAST (left) and the Observer (right)

Discussion

The comparison of the Observer measurement with well-established optical characterization tools VSHOT and SOFAST provides credibility to the Observer measurement. The RMS of the difference between VSHOT and the Observer was slightly better at 1.6 mrad than the RMS of the difference between SOFAST and the Observer at 2.1 mrad. One explanation for the larger discrepancy with SOFAST is the larger uncertainty in that Observer measurement due to the test setup. Another explanation for the better comparison with VSHOT is NREL's many years of experience with the tool. Particular care was taken in the mounting of the reflector panel measured with VSHOT to obtain the most accurate measurement. On the other hand, NREL has acquired SOFAST only within the past year and has very limited experience testing with this tool. Because SOFAST was not developed at NREL and we do not have access to the raw code, we are largely ignorant of how SOFAST incorporates user inputs into its measurement.

8.1.2 Absorber Alignment Measurement

To validate the absorber alignment measurement technique, an outdoor absorber test stand was constructed to mimic the geometry of a parabolic trough collector. A 5-m × 8-m rectangle was defined on the ground to represent the aperture plane of an LS-2 type collector. Three sections of 3-m-long steel pipe with an outer diameter of 73 mm were used to represent the 70-mm-diameter absorber. Photogrammetry targets were placed approximately in a regular grid of six targets along the length and four targets across the aperture. The test setup is shown in Fig. 8.5. The distance between two corner targets along the length of the mock collector was measured using a Leica Disto D5 laser distance meter with accuracy ±1.5 mm. A Nikon D300 was used with a 20-mm fixed-focal-length-lens. The camera, mounted on an extendable mast, was used to take photographs of the setup from both sides of the aperture.

To measure the absorber location using the proposed method, two photographs were taken, one from each side of the aperture at a height of about 7 m and a horizontal distance of 7 m from

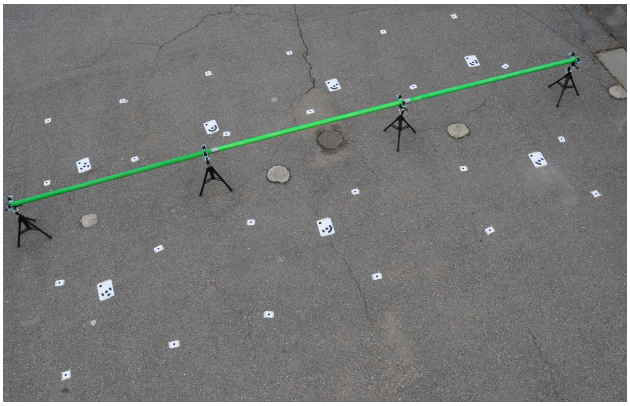

Figure 8.5: Absorber alignment measurement test setup with targets and mock absorber

the absorber. The images were processed using only the 12 targets along the rims of the mock collector. To validate this method, the absorber location was then measured using photogrammetry. Fifteen additional targets were placed on top of the absorber aligned horizontally with the center of the tube. A set of 20 to 40 photographs were taken from around the setup with the absorber targets in place. A commercial photogrammetry packet, PhotoModeler, was used to process the photographs and determine the location of each target on the absorber. The points along the absorber were then corrected by the absorber radius to account for the fact that they were placed on top of the absorber instead of at its centerline. The uncertainty in the absorber target locations found using photogrammetry is $\sigma = 0.35$ mm in X and $\sigma = 0.40$ mm in Z. Linear interpolation was used to determine the location of the absorber between photogrammetry targets. The photogrammetry results were compared to the absorber alignment measurement technique and show excellent agreement.

The absorber location was measured in three different horizontal positions (X_{a}) and three different vertical positions (Z_{a}). Figure 8.6 shows the absorber positions in the horizontal and vertical dimensions for those tests in which the absorber was purposely displaced in that dimension. The photogrammetry points are shown as dots connected by using linear interpolation between the measured points. The solid lines represent the absorber alignment measurement results. For all five test cases along the full length of the absorber, the absorber alignment method compares with the

linear fit to photogrammetry points with a pooled standard deviation of ±1.5 mm in the horizontal direction (X) and ±0.86 mm in the vertical direction (Z).

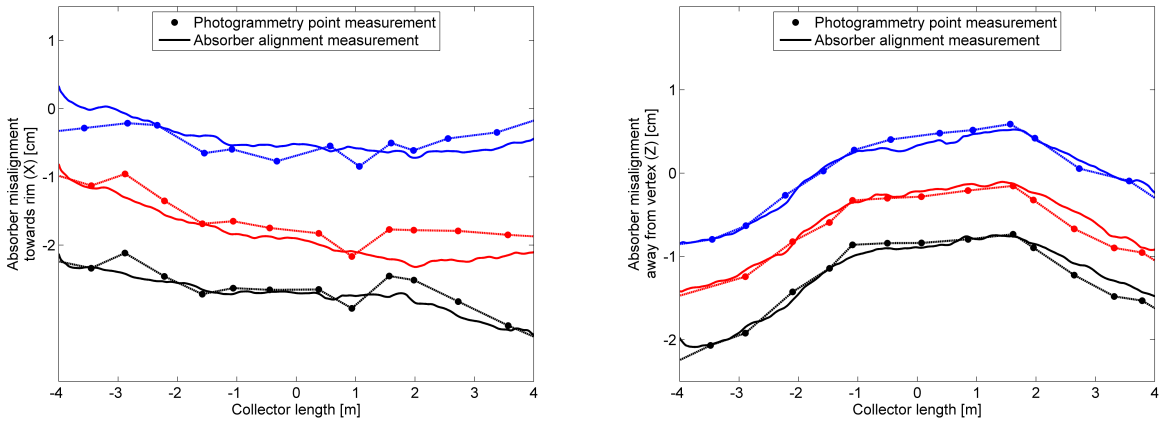

Figure 8.6: Absorber offset from focal line in the horizontal, X, (top) and vertical, Z, (bottom) direction for three different horizontal positions (top) and three different vertical positions (bottom) measured with photogrammetry (dots and dashed line) and the absorber alignment measurement technique (solid line)

8.2 R-A Angle Measurement Repeatability

A single parabolic trough collector was tested in the field to demonstrate the reflector-absorber angle measurement. The collector was oriented vertically (90° above the horizon). A Prosilica GE1910C camera with custom micro-controller and high-speed datalogging software was mounted on an R-C helicopter and flown horizontally across the aperture of the collector. The purpose of this test was to demonstrate the capability to test a collector in the vertical orientation, gain experience testing with an R-C helicopter, and demonstrate measurement repeatability under different testing conditions. The measured r-a angles are confidential and are not published here.

The lightweight octo-copter used for this test did not have a stabilization platform, and the motion of the R-C helicopter was strongly influenced by changing wind conditions. Therefore, the height and flight path of the camera could not be precisely controlled. These tests were performed on a partly cloudy day where the level of direct sunlight varied unpredictably between tests. To

compensate for these variables, a number of targets were placed along the rims of the collector and on the ground around the collector. The goal was to achieve multiple flights over the same collector with at least four targets visible for each pass of the camera over the collector so that measurement repeatability could be demonstrated. A total of five 5-minute flights were possible with the required payload and available batteries. During each flight, the camera was scanned back and forth across the collector multiple times. Five sets of measurement data were obtained for this collector, as described in Table 8.1. The uncertainty in this table is the uncertainty in the measured r-a angles with a 95% confidence as calculated with the uncertainty model using the measured camera positions and target locations for each test run.

Table 8.1: Observer measurement sets taken from a radio-controlled helicopter

Run	Camera Height [m]	Targets	Lighting	Uncertainty [mrad]
1	6.8	4	bright	1.2
2	15.4	14	dark	0.5
3	8.5	6	dark	2.1
4	7.4	4	bright	3.4
5	8.5	5	bright	2.6

The five independent measurements of r-a angles were averaged to find the mean r-a angles at each point on the collector, $\overline{\theta}_{\mathrm{ra}}$. Each measurement set was then compared to the average set. The sample standard deviations for each point on the collector are calculated with

$$s = \sqrt{\frac{1}{4}\sum_{i=1}^{5}\left(\theta_{\mathrm{ra},i} - \overline{\theta}_{\mathrm{ra}}\right)^2}. \tag{8.1}$$

The sample standard deviation is nearly uniform across the collector except near reflector panel discontinuities where the variation was about 2–3 times greater. To examine the distribution of σ, a cumulative probability plot is shown in Fig. 8.7. The sample standard deviation with a 90% confidence removes large discrepencies near reflector panel discontinuities and was found to be 1.7 mrad. The average sample standard deviation across the entire collector for the five measurement sets is 1.5 mrad. Despite large differences in camera height, number of targets used, and lighting conditions, the Observer measurement of reflector-absorber angles shows good repeatibility.

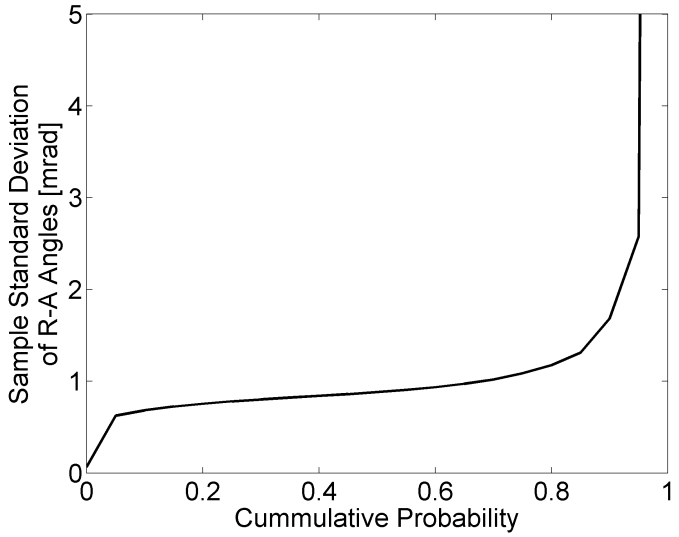

Figure 8.7: Cumulative probability of the sample standard deviations (s) of the r-a angles measured in five different flights

8.3 Gravitational Effects on Absorber Position

The absorber alignment measurement technique can be applied in the field to measure the absorber location of a collector in any orientation. To demonstrate the potential benefit of this tool to the research and development of parabolic trough collectors, the absorber alignment measurement technique was used in the field to measure the absorber location of a collector positioned in different orientations. As the parabolic trough tracks the sun from east to west throughout the day, the orientation of the collector frame and absorber with respect to gravity both change. The collector must maintain a high level of optical alignment in any orientation. Although there is some prior work using finite-element analysis to determine the effects of gravitational loading on reflector slope errors [6], there is no mention of the effects of gravity and collector orientation on absorber alignment.

For a perfectly stiff frame, receiver, and absorber, the absorber offset would not change between different collector orientations; however, for a collector with some flexibility in the receiver supports, we expect the absorber offset to be in the direction of gravity. Figure 8.8 shows three

different collector orientations, along with exaggerated expected absorber misalignments due to gravity (g).

The absorber alignment was measured for a prototype parabolic collector at its extreme positions: 0° (facing east), 90° (facing straight up), and 170° (facing west)[1] . The absorber position perpendicular to the optical axis (X_a) changed by a maximum of about 6 cm between 0° and 170°, shown in Fig. 8.9. Likewise, the absorber position on the right side of the collector changed considerably more than the left side, suggesting a particular problem with the receiver support on the right. The absorber position along the optical axis (Z_a) did not change significantly between different collector orientations. The direction of these absorber misalignments conform to expectations: for orientations of 0° and 170°, the absorber shifts in the direction of gravity. There are minimal changes in the absorber position along the optical axis due to the fixed length of the receiver supports. These results show both the importance and value of measuring the absorber alignment. Because the collector tested was a prototype, the stiffness of the frame and receiver supports can be improved in future generations of the collector to prevent absorber misalignments.

[1] The tracking mechanism prevented the collector from being positioned in a true west orientation of 180°

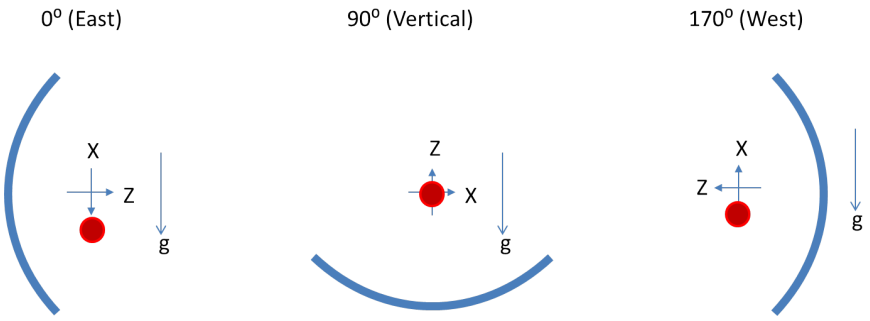

Figure 8.8: Gravitational loading and expected absorber misalignment for different collector orientations

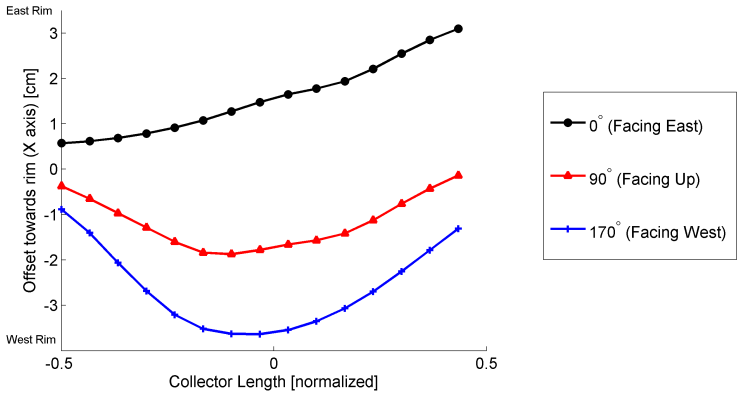

Figure 8.9: Absorber alignment perpendicular to the optical axis (X) for different collector orientations

Chapter 9

Conclusions

The Observer method presented here enables the rapid optical characterization of parabolic trough collectors in the field with the collector positioned in any orientation. This tool fills a subtaintial gap in prior optical alignment measurement capabilities. The Observer method improves on the previous state-of-the-art tool TARMES, which was unable to measure stationary collectors as well as collectors oriented above 0°. Likewise, TARMES required a direct line of sight from the camera to the collector of 100 times the collector focal length, preventing TARMES from measuring the majority of collectors in a solar field. The Observer method solves these three limitations through the use of photogrammetry bundle adjustment to find the camera location. For the Observer method, the camera can be placed at any reasonable distance from the collector (10-40 m), as long as the the minimum spatial resolution, angular resolution, and camera-target angle are statisfied.

A detailed Monte Carlo uncertainty model was developed to determine the uncertainty in the Observer measurements. Using this model, the measurement uncertainty in reflector-absorber angles was shown to depend on three key test parameters: the spatial and angular resolution of the data, and the angle between the camera and the two widest targets (camera-target angle), which should each be maximized to minimize measurement uncertainty. Recommended values of $\Delta x_{\mathrm{ap}} =$ 2.5 cm, $\Delta\Phi_{\mathrm{c}} = 6$ mrad, and $\theta_{\mathrm{ct}} = 20°$ provide guidelines to the user developing a test setup and result in a measurement uncertainty of ± 1 mrad with a 95% confidence. The uncertainty model was used to show that the height of the camera above the collector can be freely varied without

significantly impacting the measurement uncertainty as long as the targets are placed to maintain the recommended camera-target angle. The uncertainty model allows the measurement uncertainty for each specific testing scenario using the Observer method to be determined accurately.

The Observer method was validated by comparing the reflector surface slope errrors and absorber position measurements to well-established and trusted tools. The reflector surface slope errors measured with the Observer were compared to two traditional laboratory reflector slope error measurement tools: VSHOT and SOFAST. The root-mean-square of the difference in reflector slope error measurements was 1.6 mrad for comparison with VSHOT and 2.1 mrad for comparison with SOFAST. The absorber alignment measurement was compared to traditional photogrammetry with a root-mean-square difference of 1.5 mm and 0.86 mm for the X- and Z-components of the absorber position, respectively.

The capabilities of the Observer method were demonstrated in the field on prototype parabolic trough collectors. The reflector-absorber angles were measured with the collector oriented 90° above the horizon by mounting the camera on a radio-controlled helicopter. The same collector was measured five times with different camera heights, targets, and lighting conditions. The average sample standard deviation from five measurements for all points on the collector was 1.5 mrad. The absorber alignment measurement was demonstrated in the field by measuring the absorber position as a function of collector orientation with the collector oriented at 0°, 90°, and 170°. The results show that the absorber position changed by over 6 cm in the X-direction between the extreme collector orientations. This documentation of absorber position misalignment as a function of orientation reinforces the benefit the Observer tool will bring to the concentrating solar power industry. Overall, the Observer method enables a more accurate measurement of the optical alignment of parabolic trough collectors by allowing collectors to be tested in the field after installation and in all operating orientations.

Bibliography

[1] C. E Andraka, S. Sadlon, B. Myer, K. Trapeznikov, and C. Liebner. Rapid reflective facet characterization using fringe reflection techniques. In Proceedings of the ASME 2009 Conference on Energy Sustainability, San Francisco, CA, July 2009.

[2] P. Bendt, A. Rabl, H.W. Gaul, and K.A. Reed. Optical analysis and optimization of line focus solar collectors. Technical Report TR-092, Solar Energy Research Institute, September 1979.

[3] Jean-Yves Bouguet. Camera calibration toolbox for MATLAB. http://www.vision.caltech.edu/bouguetj/calib_doc/, July 2010.

[4] J. David Briers. Optical testing: a review and tutorial for optical engineers. Optics and Lasers in Engineering, 32(2):111–138, 1999.

[5] D. C. Brown. Close-range camera calibration. Photogrammetric Engineering, 37(8):855–866, 1971.

[6] J. M. Christian and C. K. Ho. Finite element modeling and ray tracing of parabolic trough collector for evaluation of optical intercept factor with gravity loading. In Proceedings of the ASME 5th International Conference on Energy Sustainabiliby, Washington, DC, August 2011.

[7] T. A Clarke. An analysis of the properties of targets used in digital close range photogrammetric measurement. ISPRS Journal of Photogrammetry and Remote Sensing, 50(3), 1995.

[8] R. B. Diver and T. A. Moss. Development of a top alignment system for parabolic trough solar collectors. In Proceedings of the 14th SolarPACES International Symposium, Las Vegas, USA, Las Vegas, NV, 2008.

[9] J. Dold. Influence of large targets on the results of photogrammetrci bundle adjustment. International Archives of Photogrammetry and Remote Sensing, XXXI(Part B5), 1996.

[10] Duke Solar Energy. Collection of relevant LS-2 baseline data. Technical report, National Renewable Energy Laboratory, Sanford, NC, 2000.

[11] J. Fernandez-Reche and A. Fernandez-Garcia. Photogrammetric inspection of the low cost CAPSOL parabolic-trough collector prototype. In SolarPACES, Berlin, Germany, September 2009.

[12] L. Foucault. Description des procedes employes pour reconnaitre la configuration des surfaces optiques. C R Acadamie Sci. Paris, 47:958–959, 1858.

[13] J. Hartmann. Objectivuntersuchungen. Zeitschrift für Instrumentenkunde, XXIV, 1904.

[14] A. Heimsath, W. Platzer, T. Bothe, and W. Li. Characterization of optical components for linear Fresnel collectors by fringe reflection method. In Proceedings of the 14th SolarPACES International Symposium, Las Vegas, USA, Las Vegas, NV, 2008.

[15] Y. Y. Hung, L. Lin, H. M. Shang, and B. G. Park. Practical three-dimensional computer vision techniques for full-field surface measurement. Optical Engineering, 39:143, 2000.

[16] IEA. Technology roadmap concentrating solar power. International Energy Agency, Paris, France, 2010.

[17] EOS Systems Inc. PhotoModeler. http://www.photomodeler.com/index.htm, 2011.

[18] S. A. Jones, J. K. Gruetzner, R. M. Houser, R. M. Edgar, and T. J. Wendelin. VSHOT measurement uncertainty and sensitivity sutdy. In Proceedings of the 32th IECEC, Honolulu, HI, 1997.

[19] L. King, David. Beam quality and tracking accuracy evaluation of second generation and Barstow production heliostats. Technical Report SAND82-0181, Sandia National Laboratories, Albuquerque, NM, 1982.

[20] C. Kutscher, F. Burkholder, and J. K. Stynes. Generation of a parabolic trough collector efficiency curve from separate measurements of outdoor optical efficiency and indoor receiver heat loss. Journal of Solar Energy Engineering, 134:011012, February 2012.

[21] C. F Kutscher. Tackling climate change in the US: Potential carbon emissions reductions from energy efficiency and renewable energy by 2030. American Solar Energy Society, 2007.

[22] E. Mikhail, J. Bethel, and J. C. McGlone. Introduction to Modern Photogrammetry. Wiley, 2001.

[23] M. Montecchi, A. Benedetti, and G. Cara. Optical alignment of parabolic trough modules. In Proceedings of the 16th SolarPACES International Symposium, Perpignan, France, 2010.

[24] A. Neumann, A. Witzke, S. A. Jones, and G. Schmitt. Representative terrestrial solar brightness profiles. Journal of Solar Energy Engineering, 124(2):198, 2002.

[25] NREL. System Advisor Model (SAM). https://sam.nrel.gov/, 2012.

[26] K. Pottler, E. Lüpfert, G. H.G Johnston, and M. R Shortis. Photogrammetry: A powerful tool for geometric analysis of solar concentrators and their components. Journal of Solar Energy Engineering, 127:94, 2005.

[27] C. Prahl, B. Stanicki, C. Hilgert, S. Ulmer, and M. Röger. Airborne shape measurement of parabolic trough collector fields. In Proceedings of the 17th SolarPACES International Symposium, Granada, Spain, 2011.

[28] J. A. Quiroga, D. Crespo, and E. Bernabeu. Fourier transform method for automatic processing of moiré deflectograms. Optical Engineering, 38:974, 1999.

[29] T. R. Ritchie, A. I. Burton, A. G. Imenes, and W. Stein. Optical assessment of CSIRO solar array heliostats. Technical report, National Solar Energy Centre CSIRO Energy Technology, Australia, 2008.

[30] R. Ritter and R. Hahn. Contribution to analysis of the reflection grating method. Optics and Lasers in Engineering, 4:13–24, 1983.

[31] M. Röger, C. Prahl, and S. Ulmer. Fast determination of heliostat shape and orientation by edge detection and photogrammetry. Technical report, German Aerospace Center (DLR), 2008.

[32] V. Romero. CIRCE2/DEKGEN2: A software package for facilitated optical analysis of 3D distributed solar energy concentrators. Technical Report SAND91-2238, Sandia National Laboratories, Albuquerque, NM, March 2004.

[33] B. Schiricke, R. Pitz-Paal, E. Lüpfert, K. Pottler, M. Pfänder, K.-J. Riffelmann, and A. Neumann. Experimental verification of optical modeling of parabolic trough collectors by flux measurement. Journal of Solar Energy Engineering, 131:011004, 2009.

[34] M. R Shortis and G. H. G. Johnston. Photogrammetry: An available surface characterization tool for solar concentrators, part l: Measurements of surfaces. Transactions of the ASME, 118:146–150, August 1996.

[35] SolarPACES. NREL: Concentrating solar power projects - parabolic trough projects. http://www.nrel.gov/csp/solarpaces/parabolic_trough.cfm, 2012.

[36] S. Ulmer, B. Heinz, K. Pottler, and E. Lüpfert. Slope error measurements of parabolic troughs using the reflected image of the absorber tube. Journal of Solar Energy Engineering, 131, 2009.

[37] T. Wendelin. SOLTRACE: A new optical modeling tool for concentrating solar optics. In Proceedings of ISEC, pages 253–260, Hawaii, USA, March 2003.

[38] T. Wendelin, K. May, and R. Gee. Video scanning hartmann optical testing of state-of-the-art parabolic trough concentrators. In Proceedings of the ASME 2006 International Solar Energy Conference, Denver, CO, July 2006.

[39] T. J. Wendelin, G. J. Jorgensen, and R. L. Wood. SHOT: a method for characterizing the surface figure and optical performance of point focus solar concentrators. Solar Engineering, pages 555–560, 1991.

[40] K. W. Wong. Basic mathematics of photogrammetry. In C. Slama, C. Theurer, and S. Henriksen, editors, Manual of Photogrammetry. American Society of Photogrammetry and Remote Sensing, 4th edition, 1980.

[41] R. Wood. Distant observer techniques for verification of solar concentrator optical geometry. Technical Report UCRL-53220, Lawrence Livermore National Laboratory, October 1981.

[42] G. Zhu and A. Lewandowski. A new optical evaluation approach for parabolic trough collectors: First-principle optical intercept calculation. Journal of Solar Energy Engineering, 134:041005, November 2012.

Appendix A

Extended Literature Review

Optical testing can be broadly classified into geometric testing, interferometry, and image evaluation. Geometric testing measures surface slope errors or ray aberrations. Interferometry requires coherent light and most commonly examines the interferrogram between a known wavefront and a wavefront produced by the test object. Image evaluation examines the image produced by the optical system directly for qualitative information or tests the resolution of the system. The current application — testing the optical alignment of a parabolic troughs in the field — has been successfully accomplished with geometric testing, hybrid techniques combining geometric testing with pseudo-interferometry, and image evaluation.

A.1 Geometric Testing

Geometric tests can be used to determine surface slope errors or ray aberrations of an optical system. For a simple focusing system such as the parabolic trough, geometric testing can be performed in one of two ways. The first is to project certain rays of light onto the optical system and then measure where they focus. The second method is to allow full illumination of the optical element and observe the image at the focal point [4]. The two traditional geometric optical tests that illustrate these methods are the Hartmann test [13] and the Foucault knife-edge test [12].

The Foucault knife-edge test is ideal for qualitative measurements of point-focus mirrors. A knife edge is placed near the focus and moved through the image of a point source. The shadow observed from behind the focus provides information about the mirror aberrations. For a perfectly

spherical lens, the aperture will darken uniformly; nonuniform illumination is the result of aberrations. The knife-edge test was used for over a century for quality testing of telescopes. The wire test is a variation of the knife-edge test that uses a wire instead of a knife edge. This test is superior for providing quantitative data.

The Hartmann test provides a quantitative measurement of surface slope directly. A screen with a uniform grid of holes is placed in front of the test object. An image of the light reflected through the holes is taken at the focal point of the concentrator. The location of the light spots in the image can be used with the corresponding location of the holes in the screen to determine the slope of the mirror at the hole locations. A modification of the Hartmann test — the Video Scanning Hartmann Optical Test (VSHOT) — was developed by SunLab (a collaboration between NREL and Sandia) for the optical characterization of point-focus solar collectors and subsequently line — focus collectors including parabolic troughs [18]. A detailed description of this technique is provided under the section on Laser Scanning in Appendix A.4.

A.2 Hybrid Techniques

The Ronchi test and moiré techniques use fringes that are not the result of interference. These tests can both be performed with incoherent light. The Ronchi test passes light from a slit through a grating placed near the focal point of the test object. The resulting image consists of a fringe pattern that can be used for both qualitative and quantitative information about the test object [4].

The moiré effect is a fringe pattern that is created when two grids of different spacing or at different angles are superimposed. Although the original moiré technique requires two gratings or fringes, a more recent technique — the fringe reflection method — has been developed to use a single grating. The fringe reflection method has been applied to the optical characterization of several types of CSP collectors [30]. A more detailed review of this method is provided in the section Fringe Reflection in Appendix A.6.

A.3 Applications to CSP

There are a vast number of optical testing methods available. However, very few of them are applicable to CSP collectors due to the large size of the optic and the need for high spatial resolution and quantitative information. There are five main techniques currently applied to measure the optical alignment of parabolic troughs: laser scanning, photogrammetry, fringe reflection, flux measurement, and reflected-absorber image analysis.

A.4 Laser Scanning

Laser scanning is the oldest technique used to characterize solar reflectors. Sandia National Laboratories identified that surface contour errors could be measured independently of surface roughness errors and then their effects combined. Surface contour errors can thus be characterized as part of the intercept factor, and surface roughness errors can be characterized independently as the surface reflectance. The first laser ray-trace system for measuring surface contour errors of parabolic solar reflectors used a He-Ne laser. The laser was aimed at the test article, and the location of the reflected ray was measured by a linear photo-potentiometer located at the design focal length. The laser was mounted on a track allowing it to perform a horizontal scan of the reflector. The reflector was displaced vertically and the procedure repeated to develop a 2D plot of the surface of the test article. The next major laser ray-trace measurement system was developed

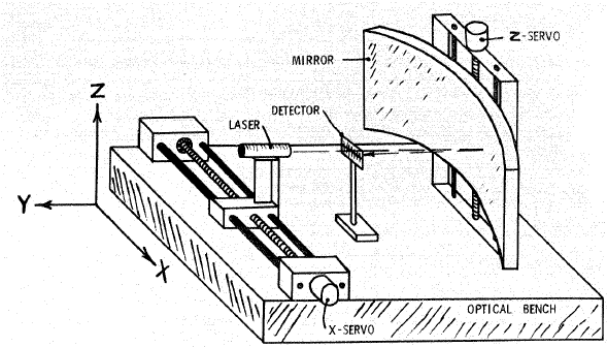

Figure A.1: Original scanning laser measurement system from Sandia National Laboratories [39]

in the early 1990s. The Scanning Hartmann Optical Tester (SHOT) was developed by the Solar Energy Research Institute (SERI) to characterize the optical surface of large-aperture solar dish collectors [39]. The project was aimed toward characterizing parabolic-shaped dish reflectors with diameters up to 15 m. Conventional measurement techniques for optical telescope systems were not applicable because of the larger apertures of solar concentrating dishes (an order of magnitude greater), and methods used for large radar and satellite antennas (although similarly sized optics) were not applicable because the parabolic solar dish concentrator cannot be approximated as a sphere. Other traditional mirror testing methods were not applicable because of the imprecision of solar mirrors. Conventional methods for high-quality optical testing are designed to detect errors two to four orders of magnitude less than those found in solar concentrators. Before selecting the Scanning Hartmann method as the most appropriate measuring technique, other methods were investigated, including the Distant Observer method. This method was ruled about because it would require very large distances for large dishes and has limited slope resolution.

The original Hartmann technique uses a mask with a uniform grid of holes in front of the optic. A point source of light is shined at the mask and the optic behind it. Light passes through the holes in the mask, is reflected by the mirror, and returns through the holes onto a target placed a distance of about twice the focal length of the test object from its vertex. The pattern of light reflected onto the target allows one to characterize the shape of the mirror; however, for parabolic dishes, which cannot be approximated as spherical, this method was modified to use a scanning laser as the light source and no mask. The laser illuminates a single spot on the mirror at a time so that this point on the mirror can be associated with the corresponding reflected laser spot on the target. In this way, a uniform grid of points across the optic can be developed over a period of time, which replicates the grid of points created by the mask at a single point in time.

The angle at which the laser beam hits the test article is known, as well as the distance between the target and the vertex of the test article. By measuring the point on the target that the reflected laser beam hits and assuming a shape for the optic, the slope of the surface at each point can be calculated. During the data processing, the actual shape of the optic is calculated.

A Zernike polynomial is fit to the measured data, and then the difference between the measured slope and the derivative of the Zernike polynomial is calculated at each point to determine the root-mean-square (RMS) slope error. The Zernike polynomial fit is then repeated until a minimum RMS slope error is achieved. This provides the most accurate description of the surface.

The Video Scanning Hartmann Optical Test (VSHOT) was later developed by SunLab, a collaboration between NREL and Sandia National Laboratories [18]. VSHOT is based heavily on its namesake, SHOT, with the addition of a CCD video camera, as well as many other functional improvements. VSHOT was adapted to characterize parabolic trough concentrators as research focus shifted from point-focus concentrators to line-focus concentrators. NREL currently uses the VSHOT system both in the laboratory and in the field to characterize prototype parabolic mirrors developed by industry. VSHOT is considered the state of the art in laser scanning for the characterization of parabolic trough solar reflectors.

A.5 Photogrammetry

Although the term "photogrammetry" was not coined until 1893 by Meydenbauer, photogrammetry is in essence based on the principles of perspective that were first described by Leonardo da Vinci in 1480. The geometric measurement of objects using photography began at the same time as photography. In the mid 1800s, photogrammetry was used for both architectural measurement and topographical mapping. In 1849, Laussedat was the first to attempt aerial photography from a balloon. He was followed by Nadar, Fairman, and finally Cornele B. Adams who patented his "Method for Photogrammetry," which used aerial photographs taken in a balloon from two different locations. The invention of the airplane, computer, and digital camera aided the progression of photogrammetry to its current state [22].

Photogrammetry was first applied to the optical characterization of solar concentrators at the Australian National University [34]. The goal was to measure the surface contour of a 400-m^2 paraboloid dish concentrator. Additionally, a 5-m dish, a 3.5-m equilateral triangular mirror panel, and a 30-cm curved mirror panel were measured. The 400-m^2 dish was prepared with 162 targets

spaced uniformly across the triangular panels comprising the dish. Six camera stations were selected and four photographs taken at each station. The camera had to be positioned with a crane in order to photograph the dish. The camera network was designed for self calibration. The accuracy achieved for the big dish was 1:19,000. Accuracy improvements of 1:47,000 were achieved later when measuring the EuroTrough space-frame structural support at the Platforma Solar de Almería. The structure was measured to determine the effects of thermal expansion throughout the day. Additionally, the mirror facets were measured to determine gravitational loading at different angular positions [26].

Photogrammetry has since been applied to the optical characterization of both heliostats [29], [31] and parabolic troughs [33], [11]. The major benefit of photogrammetry is its scale independence and the ability to test collectors in any orientation; however, the main limitations of photogrammetry are the extensive setup and the fact that slope is not measured directly. The setup requires applying a grid of targets that the camera can automatically detect on the surface to be measured. This is a very tedious task that can take up to a day for a single module, and the resolution depends directly on the number of targets used. The photogrammetric method measures the location of the surface at the target points. A surface is then fit to the point locations, and the slope is calculated as the derivative of that surface. Because slope is the measurement of interest, obtaining the slope from the point locations results in a less accurate measurement.

A.6 Fringe Reflection

The fringe reflection method or reflection grating method was developed to meet a demand for measuring the curvature of free-form specular surfaces, especially in the automotive industry [30]. Fringe reflection is derived from traditional moiré reflection but uses only one of two gratings normally required for moiré techniques. The method was first applied to measure the slopes of reflectors in CSP by the German institutes Fraunhofer ISE and BIAS [14]. Currently, fringe reflection is used to characterize the reflector slope for both linear Fresnel collectors and parabolic dishes [1].

It is easily observed that the reflection of an object provides information about the reflective surface in which it is viewed. For example, when looking at a reflection on a surface of water, the reflection becomes distorted if the liquid's surface is disturbed. Likewise, the door of a car or the side of a building may reflect a distorted image because the reflective surface is not perfectly flat. The fringe reflection technique uses this phenomenon by analyzing the image of a known object in a reflective surface. This technique requires only a camera, the test object, and a monitor on which a pattern can be displayed. The test object — a reflective surface — is placed where the reflected pattern from the monitor will be visible in the camera. A sinusoidal fringe pattern, as shown in Figure A.2, is used as the regular pattern. A photograph is taken of the test object showing the

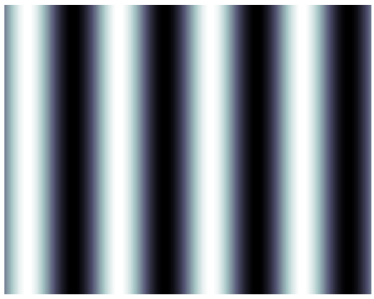

Figure A.2: Example sinusoidal fringe pattern

reflected image of the fringe pattern. If each point on the test object can be associated with a phase in the sinusoidal fringe, the slope of the test object can be determined at each point. There are several techniques used to relate each point on the test object to its corresponding phase in the fringe pattern. One technique is phase shifting, which is done by projecting four different fringe patterns shifted 0°, 90°, 180°, and 270°. The phase ϕ at a point can then be determined by measuring the intensity in each photograph at that point [15]. The phase can also be determined using the Fourier Transform method as described in [28]. Determining the relationship between phase and angle for a perfectly flat test object provides a calibration for the camera-monitor geometry, which allows compensation for tilt in the setup as well as camera lens properties. Once the calibration is determined, it can be applied to all future measurements if the system orientation is not changed.

Appendix B

Image Processing

B.1 Quadratic Surface Fit

A quadratic surface can be fit to the reflector surface slope errors to minimize the measurement error. This method is used in the laboratory when the absorber position is measured and the shape of the reflector is largely unknown. An iterative least-squares method to perform the fit is given here.

The camera locations, $(X_\mathrm{c}, Y_\mathrm{c}, Z_\mathrm{c})$, the directions of the incident rays from the camera $(\vec{r_\mathrm{c}})$, and the location of the absorber $(X_\mathrm{a}, Z_\mathrm{a})$ are found during the measurement process and do not change between iterations. The steps are as follows:

(1) Find the intersection points of the incident rays with the quadratic surface.

(2) Determine the ideal surface slope at those points.

(3) Calculate the absorber and camera angles.

(4) Calculate the measured slopes.

(5) Use a least-squares method to find a new quadratic surface.

A general quadratic equation is given in Eqn. B.1.

$$Z(X,Y) = aX^2 + bXY + cX + dY^2 + gY + h \tag{B.1}$$

Because the Observer method is only able to measure the reflector surface slope errors in the transverse direction, the longitudinal slope is assumed to be equal to the partial derivative of the surface in the longitudinal direction without any slope errors. The coefficients d and g are thus set to the design values of zero. Likewise, the vertex of the reflector can be located at an arbitrary location in space; we select $h = 0$ to set the vertex as the origin of our coordinate system. With these simplifications the quadratic surface becomes

$$Z(X, Y) = aX^2 + bXY + cX. \tag{B.2}$$

In Step 1, the intersection points of the incident rays from the camera with the quadratic surface $(X_\mathrm{t}, Y_\mathrm{t}, Z_\mathrm{t})$ are determined by parameterizing in the direction of the incident ray $(\vec{r_\mathrm{c}})$:

$$\begin{bmatrix} X_t \\ Y_t \\ Z_t \end{bmatrix} = \begin{bmatrix} X_c \\ Y_c \\ Z_c \end{bmatrix} + t\vec{r_\mathrm{c}}. \tag{B.3}$$

The parameter, t, is found by substituting $(X_\mathrm{t}, Y_\mathrm{t}, Z_\mathrm{t})$ in Eqn. B.3 into (X, Y, Z) in Eqn. B.2 and solving for t. For Step 2, the ideal slope is found by taking the partial derivative in the transverse direction of the quadratic surface (Eqn. B.2) at the intersection points $(X_\mathrm{t}, Y_\mathrm{t}, Z_\mathrm{t})$. Step 3 is to find the absorber and camera angles. Figure B.1 depicts the relevant angles. The absorber angles are the angles between the intersection points and the center of the absorber $(\theta_\mathrm{absorber})$, which are calculated with

$$\theta_\mathrm{absorber} = \tan^{-1}\left(\frac{X_\mathrm{r} - X_\mathrm{t}}{Z_\mathrm{r} - Z_\mathrm{t}}\right). \tag{B.4}$$

The camera angles are the angles between the intersection points and the camera (θ_camera) found with

$$\theta_\mathrm{camera} = \tan^{-1}\left(\frac{r_\mathrm{c,x}}{r_\mathrm{c,z}}\right). \tag{B.5}$$

In Step 4, the measured slope is calculated. The measured slope is related to the angle of the measured surface normal (θ_normal) with

$$\left(\frac{\partial Z}{\partial X}\right)_\mathrm{m} = -\tan\left(\theta_\mathrm{normal}\right). \tag{B.6}$$

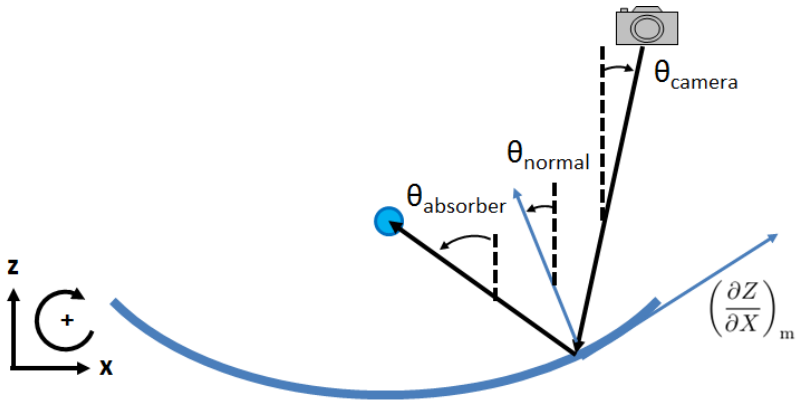

Figure B.1: Schematic of reflector, absorber, and relevant angles

By the law of reflection, the angle of the surface normal is equal to the average of the incident (θ_{camera}) and reflected (θ_{absorber}) angles:

$$\theta_{\text{normal}} = \frac{1}{2}(\theta_{\text{camera}} + \theta_{\text{absorber}}). \tag{B.7}$$

For Step 5, the coefficients of the best-fit quadratic surface are determined by minimizing the absolute difference between the slope of the best-fit surface in the transverse direction ($\partial Z/\partial X$) and the measured slope $(\partial Z/\partial X)_{\text{m}}$. The error, E, is described with

$$E(a,b,c) = \sum_{i=1}^{n}\left[\left(\frac{\partial Z}{\partial X}\right)_i - \tan\left(\theta_{\text{normal}}\right)_i\right]^2 = \sum_{i=1}^{n}\left[(2aX_i + bY_i + c) - \tan\left(\theta_{\text{normal}}\right)_i\right]^2. \tag{B.8}$$

The least-squares problem is formulated by minimizing the error that occurs when its gradient is equal to zero:

$$\nabla E = 2\sum_{i=1}^{n}\left[(2aX_i + bY_i + c) - \tan\left(\theta_{\text{normal}}\right)_i\right][2X_i, Y_i, 1] = 0. \tag{B.9}$$

Expanding the vector multiplication above results in the following matrix equation:

$$\begin{bmatrix} \sum_{i=1}^{n} 4X_i^2 & \sum_{i=1}^{n} 2X_iY_i & \sum_{i=1}^{n} 2X_i \\ \sum_{i=1}^{n} 2X_iY_i & \sum_{i=1}^{n} Y_i^2 & \sum_{i=1}^{n} Y_i \\ \sum_{i=1}^{n} 2X_i & \sum_{i=1}^{n} Y_i & \sum_{i=1}^{n} 1 \end{bmatrix} \begin{bmatrix} a \\ b \\ c \end{bmatrix} = \begin{bmatrix} \sum_{i=1}^{n} X_i \tan\left(\theta_{\text{normal}}\right)_i \\ \sum_{i=1}^{n} Y_i \tan\left(\theta_{\text{normal}}\right)_i \\ \sum_{i=1}^{n} \tan\left(\theta_{\text{normal}}\right)_i \end{bmatrix}. \tag{B.10}$$

Rewritting Eqn. B.10 as

$$Ak = Y, \tag{B.11}$$

where k is the vector containing the three surface coefficients, a, b, and c, then the solution is found by solving the linear least-squares problem with

$$k = (A^{\mathrm{T}}A)^{-1}(A^{\mathrm{T}}Y). \tag{B.12}$$

Using the new quadratic surface, steps 1-5 are repeated until the solution converges to a final quadratic surface. Once the solution has converged, the slope errors relative to the best-fit quadratic surface are found with

$$\theta_{\mathrm{e}} = \tan^{-1}\left(\frac{\partial Z}{\partial X}\right) - \tan^{-1}\left(\frac{\partial Z}{\partial X}\right)_{\mathrm{m}}. \tag{B.13}$$

B.1.1 Marching-Squares Algorithm

A built-in MATLAB function that uses a marching-squares algorithm is used to find contour lines. The marching-squares algorithm begins by converting the gray-scale image to a binary images using the contour level as the threshold. Figure B.2 demonstrates an example of this algorithm. The blue and red dots represent the logical values corresponding to an intensity level above the

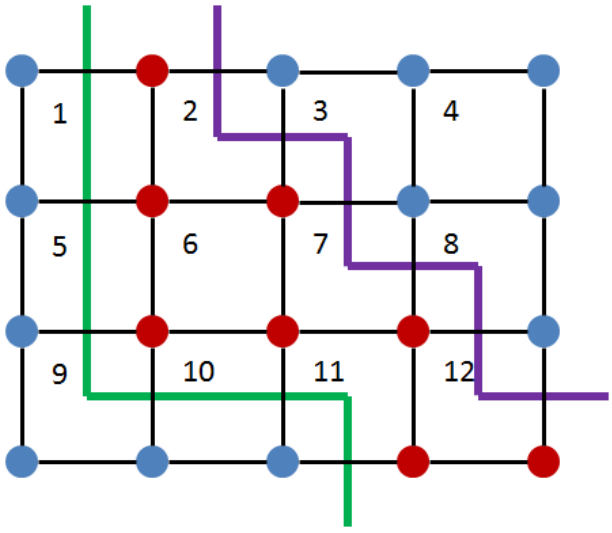

Figure B.2: Example of marching-squares algorithm used to define contours

threshold and an intensity level below the threshold, respectively. A regular grid is created across the image (numbered 1-16 in Fig. B.2). Each grid cell is then searched looking for one in which the four corner values enclosing that square are not all equal; this square represents the beginning of a contour line. The algorithm then marches around that square looking for two different logical values on the same side of the square. A side with different end values shows where the contour exits the cell. A more precise location on this exit edge is found by linearly interpolating between the original gray-scale intensity values on the ends to find the location of the contour level value. The square adjacent to the exit side is then chosen as the next square, and the algorithm marches around this new square to determine where the contour exits. The contour is thus traced through the image until it either reaches the border of the image or reconnects with itself. Any remaining grid cells are then searched to find additional contour lines. In the example shown in Fig. B.2, the contour-finding algorithm began in square 1 and traced the green contour line until it hit the border of the image in square 11. The search resumed in square 2 and traced the purple contour line through to square 12.

B.1.2 Ellipse Fit

The linear least-squares ellipse fit uses the general form of a quadratic equation given as

$$ax^2 + 2bxy + cy^2 + 2dx + 2fy + g = 0. \tag{B.14}$$

To formulate the traditional least squares problem, we divide Eqn. B.14 by a and subtract x^2 from both sides to yield

$$2\frac{b}{a}xy + \frac{c}{a}y^2 + 2\frac{d}{a}x + 2\frac{f}{a}y + \frac{g}{a} = -x^2, \tag{B.15}$$

where the prime denotes the original coefficient divided by a. The problem is now posed as

$$X\beta = \Upsilon \tag{B.16}$$

$$X = [xy \;\; y^2 \;\; x \;\; y \;\; 1] \tag{B.17}$$

$$\beta = \begin{bmatrix} b/a \\ c/a \\ d/a \\ e/a \\ f/a \end{bmatrix} \tag{B.18}$$

$$\Upsilon = -x^2 \tag{B.19}$$

Appendix C

Camera-Mounting Platforms

Camera-mounting platforms, in addition to the remote-controlled helicopter and extendable mast, that were tested include: a full-size helicopter, remote-controlled airplanes (Fig. C.1), tethered aerostat (Fig. C.2), and telescope (Fig. C.3). The full-size helicopter was extremely costly and subject to large vibrations; a large helicopter is also limited in how close it can approach the collectors. The remote-controlled airplane lacked the maneuverability and fine control of the remote-controlled helicopter. The tethered aerostat was tested as a stationary camera platform to be used with a rotating collector; however, it could not be placed accurately enough in a single location because its position was strongly subject to the wind. Likewise, the aerostat moved significantly and uncontrollably in typical weather conditions. A telescope was also tested as a stationary camera platform to be used with a rotating collector, where the angle of the camera with respect to the collector was measured using the collector's tracking mechanism. The telescope proved useful for qualitative measurements using Wood's Distant Observer concept [41]; however, no attempt was made to develop a quantitative measurement system, and there are few circumstances in which an unobstructed line of sight on the ground between a telescope and collector is possible.

Figure C.1: Remote-controlled airplane development platform

Figure C.2: Tethered aerostat development platform

Figure C.3: Telescope development platform